Site C0018[1]

Expedition 333 Scientists[2]

Chapter contents

Background and objectives

During Integrated Ocean Drilling Program (IODP) Expedition 333, the slope basin seaward of the megasplay that is characterized in 3-D seismic data by stacked mass transport deposits (MTDs) (Strasser et al., 2011) (Fig. F1) was drilled and sampled at Site C0018. The primary goals of drilling at Site C0018 were

1. To establish a well-dated Quaternary mass-movement event stratigraphy and
2. To sample the distal part of an exceptionally thick MTD and analyze its rheological behavior to constrain sliding dynamics and tsunamigenic potential.

These goals aim at providing answers to the following questions:

1. What is the frequency of submarine landslides?
2. What is the source material of MTDs?
3. What is the importance of accretionary wedge remobilization versus surficial processes?
4. What controls the type, size, and magnitude of turbidites and MTDs and how do they change through time?
5. How do large MTDs relate to the timing of splay fault activity as inferred from Nankai Trough Seismogenic Zone Experiment (NanTroSEIZE) Stage 1 drilling (Strasser et al., 2009)?
6. What are the dynamics of large submarine landslides and can we infer their tsunamigenic potential?

By addressing these questions, we aimed to isolate tectonic processes influencing magnitude and occurrence of submarine landslides along active subduction zone margins and to understand their potential for triggering catastrophic events in terms of both hazards (tsunamigenic landslides) and sediment mass transfer within the context of margin evolution.

Site C0018 (proposed Site NTS-1A) (water depth = 3084.35 m) is located on a margin-perpendicular transect 4.5 km southwest of the NanTroSEIZE Stage 1 drilling transect (Fig. F2). It is located 5 km south-southwest of IODP Site C0008, which was drilled into a small slope basin seaward of the megasplay fault (Kinoshita, Tobin, Ashi, Kimura, Lallemant, Screaton, Curewitz, Masago, Moe, and the Expedition 314/315/316 Scientists, 2009). Site C0008 results showed the utility of using the ages of MTDs to reconstruct slope failure activity and to relate it to megasplay fault movements (Strasser et al., 2009). Apart from the deepest section, Site C0008 lacks clear evidence for MTDs because of a significant hia-

[1] Expedition 333 Scientists, 2012. Site C0018. *In* Henry, P., Kanamatsu, T., Moe, K., and the Expedition 333 Scientists, *Proc. IODP,* 333: Tokyo (Integrated Ocean Drilling Program Management International, Inc.). doi:10.2204/iodp.proc.333.103.2012
[2] Expedition 333 Scientists' addresses.

doi:10.2204/iodp.proc.333.103.2012

tus, suggesting erosion related to a prominent slope collapse structure seaward of the megasplay fault (Strasser et al., 2011; Conin et al., 2011). Site C0018 is located within a lower slope basin that (1) better represents the depocenter for downslope mass transport, (2) is clearly characterized by stacked MTDs as seismically imaged by acoustically transparent to chaotic bodies with ponded geometries (Fig. F1), and (3) includes a large, as thick as 182 m, MTD (Strasser et al., 2011). Expedition 333 drilled at a location where the MTD bodies wedge out and basal erosion is minimal. Continuous coring with hydraulic piston coring system (HPCS) and extended shoe coring system (ESCS)/extended punch coring system (EPCS) to ~314.15 meters below seafloor (mbsf) allowed sampling of the MTDs across this stratigraphic succession.

Operations

After recovering transponders by remotely operated vehicle, the D/V *Chikyu* left IODP Hole C0002G at 0300 h on 10 December 2010. After 8 nmi of transit at an average speed of 4 kt, the *Chikyu* arrived at the first transponder location for Site C0018 at 0500 h. Deployment of four transponders and calibration finished at 2045 h, and we began preparation for HPCS/EPCS/ESCS coring. The 11 inch HPCS/EPCS/ESCS bottom-hole assembly (BHA) was run into Hole C0018A at 1445 h on 11 December. Coring began at 0115 h on 12 December and continued to the 36th core, and we decided to finish at 314.15 mbsf at 2103 h on 16 December (Table T1). Operational problems were few and minor during the course of 4 days of coring. Those included damage to a seal in the inner barrel, failures on shooting, and a broken lower part of the sinker bar assembly. After recovering the inner barrel and sinker bar assembly, we spotted kill mud, displaced the hole with seawater, and pulled out of the hole. The bit was back on the rig floor at 0500 h on 17 December.

Core recovery was excellent for piston coring with the HPCS to 153.85 m drilling depth below seafloor (DSF) (Core 333-C0018A-17H), but core liner collapse or expansion in the core barrel caused problems for several cores (Cores 333-C0018A-9H and 16H were damaged). After experiencing repeated incomplete penetration and reaching the estimated MTD bottom, the coring system was shifted to the EPCS at 190.65 m DSF (Core 333-C0018A-24T). EPCS recovery was variable, ranging from 90.7% to 0% with an average recovery of 47.2%, as attempts to adjust the penetration of the EPCS cutting shoe ahead of the drill bit were met with mixed success. We switched to the ESCS after the seventh core. ESCS core recovery was surprisingly better than expected, with good recovery ranging from 70.8% to 114.9% and an average recovery of 87.35%.

Both the EPCS and the ESCS were used below the MTD (EPCS from 190.65 m DSF and ESCS from 257.15 m DSF), and core quality assessment from X-ray computed tomography (CT) scans showed no major difference between EPCS and ESCS cores. Both systems formed fractured biscuits 2–4 cm thick. However, ESCS cores appear to contain more slurry. Once split, degradation between EPCS and ESCS cores is obvious as the thickness of shear zones between biscuits and core liner increases. Some cores, including HPCS cores, were also strongly affected by gas expansion, resulting in voids and bubbly slurry intervals.

Lithology

Hole C0018A was chosen to sample a series of MTDs and underlying turbidites identified on 3-D seismic data (e.g., Expedition 316 Scientists, 2009b; Moore et al., 2007; Strasser et al., 2011). Hole C0018A follows the drilling of slope deposits, forming part of Unit I, during IODP Expedition 316 (Expedition 316 Scientists, 2009a, 2009b). A total of 313.66 m of strata was drilled in Hole C0018A, with very good recovery rates (Fig. F3). Two lithologic subunits were interpreted during the examination of cores: Subunits IA (youngest) and IB (Fig. F3). The units drilled correlate with seismic Units 1a and 1b defined by Kimura et al. (2011) and by Strasser et al. (2011).

As with other IODP sites (e.g., Expedition 316 Scientists, 2009b), depositional units in this report are distinguished based on variations in grain size, mineralogy, composition, and presence (and thickness) of sand and ash layers (Figs. F4, F5). Unit boundaries and intervals with evidence for MTDs were selected based on lithology, X-ray CT images, observations of structural style (see "Structural geology"), and seismic data interpretation (Kimura et al., 2011; Strasser et al., 2011).

Lithologic subunits mainly comprise silty clay with variable quantities of volcanic ash. Six intervals with evidence for MTDs are observed within the cored succession, with the largest, a 61.03 m interval, located below 127.55 mbsf (Fig. F3; Table T2). The silty clay consists of clay minerals with quartz, feldspar, and abundant calcareous nannofossils, diatoms, and sponge spicules. Heavy minerals (mainly pyrite), apatite, chlorite, and biotite are present in some intervals (see Site C0018 smear slides in "Core descriptions"). In turn, micas and opaque minerals are relatively rare. From bulk powder X-ray diffraction (XRD), clay mineral content of the silty clay (averag-

ing 47 wt% for the entire cored succession) shows some variations in depth, approaching 51 wt% on average between 21 and 58 mbsf (Fig. F5; Table T3). The relative abundances of feldspar and quartz increase steadily with depth, for an average of 20 wt% and 23 wt%, respectively. Near the bottom of Hole C0018A, feldspar reaches 23 wt% in abundance against 29 wt% abundance in quartz. Below Core 333-C0018A-13H (108.65 mbsf) the relative abundances of diatoms and spicules decrease. Below Core 333-C0018A-24T (190.65 mbsf) is a marked decrease in the relative abundance of nannofossils, diatoms, and spicules and a relative increase in the number of siliciclastic grains in smear slide samples. This change is confirmed by XRD data, which show almost complete depletion of calcite below 180 mbsf and a sharp increase in the relative abundance of quartz (Fig. F5; Table T3).

Subunit IA (slope-basin facies)

Interval: Sections 333-C0018A-1H-1, 0 cm, through 23H-CC, 21 cm
Depth: 0.00–190.65 mbsf
Age: Holocene–Pleistocene

Subunit IA comprises greenish gray to grayish silty clay with mostly thin (<5 cm) intercalations of volcanic ash. The subunit shows internal facies variations and can be divided into three intervals: Facies IAi, IAii, and IAiii, which are described in more detail below. Bioturbation is observed particularly in the upper part of the unit where *Zoophycos* and *Chondrites* are abundant. These ichnofossils are better observed in CT scans of cores, where they appear pervasive in some sections. Shell debris is seen in parts of the unit, particularly in Facies IAi. XRD data indicate an average content of 15 wt% calcite, 20 wt% quartz, and 47 wt% clay minerals for Subunit IA. However, variations in the relative percentage of the latter minerals are recorded at specific intervals (Fig. F5; Table T3).

Six intervals with evidence for MTDs are observed within Subunit 1A and numbered from top to bottom for convenience (Fig. F3; Table T2). The upper boundary/contact is well defined for MTDs 1, 2, and 6 and is marked by a turbidite for two of them (MTDs 2 and 6) (Fig. F6). MTD 1 extends over 2.9 m of chaotic and convolute bedding in Core 333-C0018A-1H. MTD 2 comprises in its lower part several intervals of coherent bedding bounded by probable shear zones (see detailed X-ray CT description notes in Table T4). The lowermost shear zone defines the base of the MTD 2 interval (Fig. F7). MTD 3 comprises an interval with visual evidence for remobilization near its top. Examination of the CT scan and structural data (see detailed X-ray CT description notes in Table T4) led us to consider this interval as part of a thicker MTD zone. MTD 4 is a relatively thin interval (50 cm) associated with a fluidized ash layer (Fig. F8). MTD 5 extends over cores that were also disturbed by the coring process. A zone of remobilization is identified based on visual evidence and CT scan in Core 333-C0018A-9H, although this core was damaged during extraction from the core barrel. CT scan images provide evidence for a shear zone with a sharp lower boundary that defines the base of MTD 5 (see detailed X-ray CT description notes in Table T4). It is yet unclear whether this MTD interval corresponds to a single event deposit. MTD 6 is a ~61 m interval between 127.55 and 188.57 mbsf and corresponds to the main MTD body identified in the seismic data (Strasser et al., 2011). As already noted, a turbidite deposit is found immediately above its upper boundary. Chaotic and convolute bedding (Fig. F9) and mixing of ash with hemipelagite deposits are observed in the cores, but other intervals remain coherently bedded. Several shear zones are identified from CT scans of the lower part of MTD 6 (Table T4), but none could be positively identified as the basal surface. The base of MTD 6 was therefore defined at the top of the Pink volcanic ash bed (see below), which forms a distinct thick, fine-grained, sand-sized volcanic ash layer separating disturbed landslide material from undisturbed material with original horizontal bedding below. Because the core containing this coarse sand-sized ash layer experienced severe disturbance because of gas expansion upon core retrieval, deformation and structures indicating shearing at the base of the landslide cannot be conclusively identified within this layer.

The deposition of Subunit IA occurred on a continental slope dominated by hemipelagic settling, submarine landslides, and minor contributions of volcanic ash. The onset of the hemipelagic-dominated paleoenvironment occurs at ~190 mbsf. The Subunit IA/IB boundary is defined at the base of a >1 m thick, likely reworked, coarse, sand-sized volcanic ash at 190.65 mbsf (Section 333-C0018A-23H-CC). Based on characteristic microscopic features observed in smear slides (i.e., bubble wall type glass shards and abundant hornblendes as heavy minerals [Fig. F8]), this sand bed can be tentatively correlated with the Pink volcanic ash bed with the age of ~1.05 Ma (Hayashida et al., 1996) (see Site C0018 smear slides in "Core descriptions"). Turbidity current contributions to deposition from a mixed volcaniclastic and siliciclastic source substantially increase below this latter boundary (Fig. F3; see "Subunit IB (sand-rich slope basin)").

Facies IAi

Interval: Sections 333-C0018A-1H-1, 0.0 cm, through 3H-8, 110.2 cm
Depth: 0.00–24.04 mbsf

The dominant lithology in Facies IAi is greenish gray silty clay with minor contributions of volcanic ash. Ash layers are <2 cm thick, fine grained, light to dark gray, and at least partly laminated, with sharp lower and diffuse upper contacts. These ash layers consist mainly of fresh glass with minor pumice, quartz, feldspar, mica, and calcareous nannofossils. Clay mineral content ranges from 40 to 47 wt% and averages 44 wt%, quartz content ranges from 18 to 26 wt% and averages 21 wt%, and feldspar ranges from 15 to 22 wt% and averages 17 wt%. Calcite content ranges from 11 to 26 wt% and averages 18 wt% (Fig. F5; Table T3).

An ~3 m thick interval with evidence for MTDs is present in Core 333-C0018A-1H in the form of convolute tilted strata and intervals of remobilized mud clasts (debrite) overlying tilted strata.

Facies IAii

Interval: Sections 333-C0018A-3H-8, 110.3 cm, through 7H-3, 54 cm
Depth: 24.04–57.51 mbsf

The dominant lithology of Facies IAii is greenish to dark gray silty clay, silt, and sparse fine-grained sand (Fig. F3). Most silty and sandy layers have a dominant volcaniclastic composition, but metamorphic lithic fragments with secondary quartz and feldspar are also present in variable amounts. Heavy minerals are abundant. Mica is abundant in some levels (see Site C0018 smear slides in "Core descriptions"). Individual sand and ash beds are generally <5 cm thick, showing a predominant fining-upward trend into silt and locally silty clay with indistinct boundaries between the different lithologies. However, the sand and coarse volcanic ash beds have sharp bases. Silty clay beds are typically <1 m thick with minor sandy silt and clayey silt intervals also present.

Clay mineral content ranges from 34 to 74 wt% and averages 51 wt%, quartz content ranges from 5 to 24 wt% and averages 15 wt%, and feldspar ranges from 10 to 38 wt% and averages 21 wt%. Calcite in this facies varies from 1 to 31 wt% in relative abundance (Fig. F5; Table T3). The large variations in XRD values observed in this section can be partially attributed to the lithologies and textures sampled, varying from coarse volcanic ash to silty clay (Fig. F5). The relatively higher sand- and silt-size ash content of this facies suggests the deposition of volcaniclastic sediment by relatively low energy plumes of volcanic material (Division E of Bouma [1962]). In addition, a substantial portion of the finer grained volcaniclastic material in Facies IAii comprises ash fall deposits.

Deposition in Facies IAii occurred on a continental slope basin dominated by hemipelagic settling with some contribution of volcanic ash and low-energy volcaniclastic turbidity currents. The Facies IAii/IAiii boundary at 57.5 mbsf (Section 333-C0018A-7H-3, 53 cm) is marked by the lowermost appearance of a volcanic ash deposit. Below this ash deposit, volcaniclastic contribution is mostly recorded as scattered laminae of silty ash in the underlying Facies IAiii.

One interval with evidence for MTDs occurs between 39.45 and 46.73 mbsf (Table T2). It is shown as convoluted silty clay strata with mud clasts. The lower part of the subunit (below Section 333-C0018A-5H-8, 44 cm) comprises a homogeneous silty clay that, on X-ray CT scan data, shows convolute and tilted strata with internal shear zones (see also Table T4) (Fig. F7).

Facies IAiii

Interval: Sections 333-C00018A-7H-3, 54.1 cm, through 23H-CC, 21 cm
Depth: 57.52–190.65 mbsf

The bulk of Facies IAiii comprises greenish gray silty clay intercalated with four intervals with evidence for MTDs. In contrast with Facies IAii, volcanic ash is somewhat less abundant in this succession. However, darker silty and clayey laminae are visible in the background hemipelagic silty clay. Turbidites are rare and appear associated with volcanic deposits (e.g., Section 333-C0018A-13H-9). Sand beds are virtually absent in Facies IAiii with the exception of Sections 333-C0018A-14H-7 and 14H-8 (125.40–126.45 mbsf), in which successive intervals of volcanic ash and sand are observed. The last of these intervals (125.65–126.45 mbsf) mobilized deposits that appear correlative to the Azuki volcanic ash bed (0.85 Ma; Hayashida et al., 1996), as indicated by the observation of abundant bubble wall type glass shards and obsidian grains in smear slides (Fig. F8). Clay mineral content ranges from 31 to 53 wt% and averages 46 wt%, quartz content ranges from 10 to 26 wt% and averages 21 wt%, and feldspar ranges from 11 to 35 wt% and averages 18 wt%. Calcite content ranges from 0 to 39 wt% and averages 15 wt% (Fig. F5).

Deposition in Facies IAiii occurred in a setting dominated by hemipelagic settling with some contribution by air fall volcanic ash and fine-grained volcaniclastic turbidity currents. In comparison to Facies IAii, volcaniclastic contribution is sparse but increases downward. The Facies IAiii/Subunit IB boundary is marked by the appearance of redepos-

ited volcanic ash bed at 190.65 mbsf (Section 333-C0018A-23H-CC, 21 cm), which is tentatively correlated with the Pink volcanic ash bed with the age of ~1.05 Ma (Hayashida et al., 1996) based on the abundant presence of bubble wall type glass shards and abundant hornblendes as heavy minerals (Fig. F8).

Several intervals with evidence for MTDs occur in Facies IAiii, namely at 58.01–65.75 mbsf (Section 333-C0018A-7H-5), 66.44–67.93 mbsf (Section 8H-4), 75.91–94.37 mbsf (Sections 9H-3 through 11H-5), and 127.55–188.57 mbsf (Sections 15H-2 through 23H-1) (Table T2). These intervals consist of convoluted intervals of banded silty clay strata with scarce mud clasts as observed on visual core descriptions. Tilted, convolute, and sheared intervals are visible in X-ray CT scans (Table T4). The larger thicker MTD interval comprises a mixture of mud-rich debrites, remnant hemipelagic strata, and convoluted banded deposits denoting extensive deformation in their interior (Fig. F8). The base is marked by a region disturbed by drilling, probably in relation to the presence of gas and water in a (sandy and silty) volcaniclastic deposit attributed to the Pink volcanic ash bed (Fig. F3). On XRD data, the maximum contents of clay minerals and quartz are observed in the thickest MTD interval below 127.55 mbsf. In contrast, a relative reduction in the relative abundance of calcite is observed in the same interval when compared with the strata above (Fig. F5).

Subunit IB (sand-rich slope basin)

Interval: Sections 333-C00018A-21H-CC, 21.0 cm, through 36X-CC, 64 cm

Depth: 190.65–313.66 mbsf

Age: Pleistocene

Subunit IB consists of interbedded fine-grained to medium sand, silty sand, silty clay, and clay. Subhorizontally dipping, 4–20 cm thick sand layers typically show a sharp and erosional base and normal grading. Bed spacing is 20–30 cm in average, but muddy intervals up to 4 m thick comprising no intercalated sand layer occasionally occur. The sand content of this subunit is markedly higher than overlying Subunit IA (Figs. F3, F4). Silty and fine-grained silty clay and dark olive-gray sand are dominated by metamorphic and volcanic lithic grains (quartz content averaging 29 wt% by XRD) and feldspar (averaging 23 wt% by XRD). The proportion of lithic fragments decreases in very fine sand and silt layers. Carbonate content is mostly below detection by XRD, with a local maximum of 6 wt% at 307.95 mbsf. The large variations in XRD mineral abundances throughout this section (Fig. F5) derive from the varied lithologies and textures sampled (sand to silty clay; Fig. F10). Some sand beds show normal grading with indistinct upper boundaries that grade into silty clay. The silty clay is greenish gray and is only slightly bioturbated or mottled in places. The bases of sandy beds are sharp and erosional (Fig. F10).

Ash and dispersed volcanic glass are widespread in this unit, and accumulations occur as light gray bands in otherwise greenish gray strata. The unit represents a sand-rich slope wedge system, fed by both siliciclastic and volcanogenic sources. Sand-silty clay alternations represent high-frequency cycles of turbidite flows sourced from proximal areas on the slope.

X-ray fluorescence analyses

X-ray fluorescence analyses were performed on 59 samples from Hole C0018A to estimate the bulk chemical composition of the sediments and to characterize compositional trends with depth and/or lithologic characteristics (Fig. F11; Table T5).

Major element contents show several variations with depth that are compatible with the lithologic subunits as defined earlier. The silty clays of Subunit IA are characterized by low SiO_2 content (60.2 wt% on average), compared to the underlying sand-rich Subunit IB (67.5 wt% on average) (Fig. F11). This difference may be explained by a higher proportion of siliciclastic grains in Subunit IB. In contrast, Subunit IA contains higher and less scattered Al_2O_3, Fe_2O_3, and MgO contents (Fig. F11), which can be related to a higher abundance of clay minerals. The significant decrease in CaO content observed in Subunit IB (2.0 wt% on average versus 8.8 wt% in Subunit IA) (Fig. F11) is consistent with the very low calcite content observed by XRD below ~190 mbsf.

The large variations observed for almost all the major elements at given depths between ~50 and ~100 mbsf within Subunit IA (Fig. F11) essentially account for the sampling of specific lithologies such as volcaniclastic sand beds and volcanic ash layers.

The lower part of Subunit IA, from ~100 to 190 mbsf, shows a remarkably homogeneous composition in regard to Al_2O_3, Fe_2O_3, K_2O, P_2O_5, MgO, and TiO_2 contents (Fig. F11; Table T5). The bulk composition of the thickest MTD occurring from 127.55 to 188.57 mbsf does not differ from the composition of the homogeneous overlying strata. By contrast, Subunit IB is characterized by largely scattered concentrations in almost all major elements that may be related to the heterogeneous nature of this sedimentary unit consisting of interbedded sand, silt, and clay.

Structural geology

Site C0018 is located within the slope basin. Here, drilling was performed to 313.655 mbsf to penetrate and recover MTDs and surrounding cores. Core structural data are given in C0018.XLS in STRUCTUR in **"Supplementary material."** Where possible, we corrected planar structures to true geographic coordinates using shipboard paleomagnetic data (see **"Structural geology"** in the "Methods" chapter [Expedition 333 Scientists, 2012]). The distribution of planar structures is shown in Figure **F12.** At this site, six intervals with evidence for MTDs were carefully identified based on lithologic and structural visual core descriptions and observation of X-ray CT images (see detailed X-ray CT description notes in Table **T4**).

Structural features of this site mainly record sedimentation and mass-movement processes and gravitational tectonics within a slope basin. The main structural features at this site are

- Southeast-dipping beds, normal faults, shear zones, and a slump fold above MTD 6 (thickest MTD) of lithologic Subunit IA (0–127.545 mbsf);
- Scattered beds, shear zones, and flow structures within MTD 6 (127.545–188.573 mbsf); and
- Subhorizontal beds and fissility within lithologic Subunit IB (below MTD 6) (188.573–313.655 mbsf).

Structural elements above MTD 6 (within lithologic Subunit IA)

Gently to moderately dipping beds, normal faults, and a slump fold are observed above MTD 6 in lithologic Subunit IA (Fig. **F12**). After paleomagnetic correction, bedding surfaces gently dip southeastward except for several scattered points (Fig. **F13**). This trend is consistent with local seafloor topography and southeast-dipping beds displayed in seismic reflection profiles (Fig. **F1**). Steeply dipping beds (dip angle >40°) are scarce and distributed in limited depths: 2.78, 3.20, 44.76, 45.92, 64.27, 65.80, and 92.22 mbsf. These depths range within or nearby the lithologically identified MTDs 1–5 (gray zones in Fig. **F12**), suggesting that beds were tilted in response to the deposition of MTDs.

Minor faults develop below Section 333-C0018A-6H-5 (49.00 mbsf). Faults are recognized as dark or greenish thin planes with thickness <1 mm. Their offsets in split core surfaces range up to 28 mm. Most of the faults show normal offsets of beds and burrows (Fig. **F14A**), except for one example with reverse offset (Fig. **F14B**). Faults are also expressed as bright planes with high CT numbers on X-ray CT images (Fig. **F14**), suggesting that fault materials are denser than the surrounding host sediments. This might reflect shear-induced consolidation (porosity reduction) or mineral precipitation within the fault plane. Dip angles of faults are moderate to high (generally 50°–80°). After paleomagnetic correction, orientations of faults show scattered distribution along the vertical axis (Fig. **F15**), possibly reflecting vertical maximum principal stress within the sediments. These observations suggest that high-angle faults above MTD 6 were mainly formed by gravitational collapse in response to the sedimentation and burial processes of the slope basin.

A cylindrical fold occurs in Section 333-C0018A-5H-6 (41.62 mbsf) within MTD 2 (Fig. **F16**). Lack of systematic change in orientation of the bedding plane within lithologic Subunit IA suggests that the fold was formed as a synsedimentary slump fold. Two ash beds are involved in this fold, and orientations of folded ash layers are carefully measured in X-ray CT images. Poles to the folded layers lie on a great circle, which is perpendicular to the fold axis. After paleomagnetic reorientation, the fold axis strikes east–west and dips nearly horizontal (Fig. **F17**), whereas the axial plane also dips subhorizontal. The orientation of the fold axis implies that the fold was formed in response to gravity flow of north–south direction that locally occurred in the slope.

Structural elements within MTD 6 (127.545–188.573 mbsf)

Scattered beds, shear zones, flow structures, minor faults, and web structures are observed within the thickest MTD (i.e., MTD 6, 127.545–188.573 mbsf). Reflecting remobilization of sediments, paleomagnetic poles of this depth range are scattered evenly in each core (see **"Paleomagnetism"**). As a result, paleomagnetic correction of structural elements could not have been performed within MTD 6. Moreover, HPCS coring-induced disturbance (flow-in) especially occurs in the lower part of MTD 6 (Cores 333-C0018A-18H, 19H, 20H, 21H, and 22H).

Despite the difficulty of structural analyses caused by coring-induced disturbance and the lack of reoriented data, structural features of this interval explore the internal deformation style of the MTD. Dip angles of bedding range from subhorizontal to nearly vertical (Fig. **F12**). In contrast, subhorizontal beds, which are commonly distributed both above and below MTD 6, are not observed. Scattered dip angles suggest incoherent folding within MTD 6 formed during movement of a large submarine landslide.

Shear zones and healed, dark-colored planar fabrics dividing lithologies are recognized in Core 333-C0018A-17H (145.18–152.51 mbsf) (Fig. **F18**). At Sec-

tion 333-C0018A-17H-6 (150.39–150.53 mbsf), two shear zones truncate dark grayish silty clays including fragments of volcanic ash. Greenish and brownish light-colored clay occurs between the two shear zones. On the split core surface and X-ray CT image, planar fabric is recognized in this light-colored part (Fig. F18). Shear zones also occur in Section 333-C0018A-22H-8.

Flow structures occur in Sections 333-C0018A-22H-4 through ~22H-9 (178.45–184.01 mbsf) (Fig. F19). At Section 333-C0018A-22H-6, greenish and brownish light-colored clay-rich sediments, including fragments of volcanic ash and burrows, consist of wavy-shaped flow structures (Fig. F19).

Both shear zones and flow structures exhibit typical occurrences of unconsolidated soft-sediment deformation, which is carried by independent particulate flow.

Faults are not common within MTD 6; however, faults with slickenlines and steps locally occur in Core 333-C0018A-16H (141.09–143.09 mbsf) (Fig. F20). In contrast to the faults above MTD 6, planes of these faults are not healed by relatively dense materials. Slickenlines and steps indicate that those faults have normal dip-slip offsets. Web structures, anastomosing dark-colored seams (each with thickness <2 mm), occur in Sections 333-C0018A-17H-7 to 17H-8 (Fig. F21). Web structures truncate beds and burrows. These nonhealed faults and web structures appear to occur posterior to MTD formation.

The bottom of MTD 6 is bounded by a structureless, thick sand layer.

Structural elements below MTD 6 (lithologic Subunit IB)

Subunit IB below MTD 6 is characterized by gently dipping beds of turbidites (<30°) (Fig. F22). Deformation is generally weak, and no fault is recognized within this unit. Fissility, cleavagelike planar fabric within the muddy part, weakly develops below Core 333-C0018A-31X (257.15 mbsf) (Fig. F23).

Coring-induced disturbances are commonly recognized, especially in cores sampled by ESCS (Core 333-C0018A-31X and below); however, some contain a boundary between sand and mud, providing evidence that they possess original stratigraphic relations.

Biostratigraphy

Preliminary biostratigraphy determination for Hole C0018A was based on examination of calcareous nannofossils. All core catcher samples and additional samples from sections between core catcher samples were examined. The results of nannofossil investigation are presented in Table T6. Calcareous nannofossils investigated are generally well to moderately preserved through all sections except for Samples 333-C0018A-18H-CC and 20H-CC (Table T6). The biostratigraphic results (six recognized nannofossil events) show that the entire recovered section in Hole C0018A has an age range within the Pleistocene (Fig. F24; Table T7). Two lithologic subunits have been described (see "Lithology"):

- Subunit IA: ash-bearing hemipelagic silty clay interbedded with MTDs between 0 and 190.65 mbsf, and
- Subunit IB: a sandy turbidite sequence between 190.65 and 313.66 mbsf.

Subunit IA ranges from the recent to ~1 Ma, and Subunit IB ranges from ~1 to ~1.46–1.67 Ma. Two nannofossil events in Subunit IA suggest a slightly lower sedimentation rate in the interval between 0 and 25 mbsf than the other intervals. In spite of interbedding of disturbed MTDs within Subunit IA, nannofossil analysis provides no evidence for any significant hiatus or age reversal (Table T7). Thus, it can be interpreted that no considerable erosion and overturning of sequences within Subunit IA have occurred.

Paleomagnetism

Magnetic susceptibility and remanent magnetization measurements were performed on 313 discrete samples from Site C0018. Samples for shipboard measurements were taken routinely at a frequency of two specimens per standard section (~140 cm), whereas we flexibly omitted one or two from shorter sections. The samples were subjected to alternating-field (AF) demagnetization to isolate the characteristic remanent magnetization (ChRM). The samples were typically demagnetized at 5, 10, 20, 30, and 40 mT.

Pervasive drilling-induced magnetization is commonly encountered, as noted during previous Deep Sea Drilling Project/Ocean Drilling Program/IODP legs (e.g., Gee et al., 1989; Zhao et al., 1994). This magnetization is characterized by a direction strongly biased downward. As shown in Figure F25, upon AF demagnetization to 30 mT, a significant decrease in intensity and an inclination shift toward negative or positive shallower directions. Figure F26A and F26B shows that AF demagnetization removes drilling-induced magnetizations and isolates ChRM directions successfully.

Throughout this site, sediments have low intensity of natural remanent magnetization (NRM) overall. Average NRM intensity (1.25×10^{-2} A/m) and 30 mT

and 40 mT demagnetized intensities (2.39×10^{-3} and 1.76×10^{-3} A/m) at Site C0018 are comparable with those at IODP Site C0004 and roughly one order smaller than those at Site C0008 (cf. Site C0004 $NRM_{Ave} = 1.84 \times 10^{-2}$ A/m, Site C0004 40 $mT_{Ave} = 1.15 \times 10^{-3}$ A/m, Site C0008 $NRM_{Ave} = 1.30 \times 10^{-1}$ A/m, and Site C0008 40 $mT_{Ave} = 5.58 \times 10^{-2}$ A/m). Data at 40 mT demagnetization often show incoherent behavior (Fig. F26C), likely resulting from low intensity after demagnetization that is beyond the lower sensitivity limit of the used spinner magnetometer (3×10^{-1} to 5×10^{-6} mAm^2). We therefore employed the 30 mT demagnetization step for interpretation to minimize the effects of both drilling-induced remagnetization and sensor response constraint.

A histogram of the inclinations isolated from discrete samples excluding MTD 6 horizons is shown in Figure F27. The inclinations are concentrated in a range of +45° to +60° and –35° to –50°, which correspond to an expected inclination from the geocentric axial dipole model at the latitude of this site.

Different coring systems present a different characteristic distribution in paleomagnetic declination. Declination in cores recovered using HPCS show a clustered distribution within each core, whereas those using EPCS and ESCS demonstrate scattered distribution (Fig. F25). Cores recovered using EPCS and ESCS were heavily disturbed, occurring as pieces (biscuits) interspaced with drilling slurry (see "Structural geology"). The possibility of rotating cores, as well as pieces, may be the cause of the scattered data distribution.

For intervals of particular interest for structural geology at Site C0018, we used ChRM isolated from progressive demagnetization of the discrete samples to restore azimuthal orientation. For HPCS cores, average declination can be used for most cores because no systematic twisting of core is observed (Fig. F28). For EPCS and ESCS cores, only structures from the same coherent piece as the ChRM data can be reoriented.

Natural remanent magnetization and magnetic susceptibility

Paleomagnetic data obtained in Hole C0018A present some variations in demagnetization behavior with depth. NRM intensities of the discrete samples from Hole C0018A span more than two orders of magnitude (Fig. F25). NRM intensity from the top of the hole to Sample 333-C0018A-2H-3, 90 cm (8.913 mbsf), is relatively high (averaging 7.99×10^{-2} A/m), whereas intensity decreases with depth by >1/10 to Core 333-C0018A-8H. In the lower part of Subunit IA, from Cores 333-C0018A-9H to 13H, NRM intensity tends to be stable at slightly higher values than the upper part, 4.63×10^{-2} and 1.68×10^{-2} A/m on average, respectively. In Cores 333-C0018A-13H and 14H, a significant drop in intensity associated with a transitional period of paleomagnetic polarity reversal is clearly pronounced. NRM intensity of 1.50×10^{-2} A/m at Sample 333-C0018A-13H-13, 20.5 cm (116.543 mbsf), fades rapidly to 1.58×10^{-3} A/m at Sample 333-C0018A-14H-7, 93 cm (125.017 mbsf), and recovers to 7.58×10^{-3} A/m at 53.5 cm below (Sample 333-C0018A-14H-8, 5 cm). Variations in NRM intensity are enhanced after demagnetization, which implies the transient weakening during the geomagnetic pole shift. The magnetic susceptibility is nearly synchronous with the paleomagnetic intensity, suggesting that these changes are controlled by the nature and/or concentration of ferromagnetic minerals.

Magnetostratigraphy

As shown in Table T8 and Figure F29, a number of magnetic reversals are discerned on the basis of changes in sign of inclination. The horizon of the MTD 6 (see "Lithology" for details) is disregarded here because it shows dispersed declination and inclination even with HPCS coring, which implies that the initial orientation has not been maintained.

Normal polarity from the top of the hole to Core 333-C0018A-14H corresponds to the Brunhes Chron regarding its continuity from the seafloor. Reversal in Core 333-C0018A-14H transits across this core and coincides with a weakening of the intensity as mentioned above. Because MTD 6 starts at Section 333-C0018A-15H-2, 91 cm (127.545 mbsf), polarity is disturbed below this section. A tephra in Section 333-C0018A-14H-8 has been assigned a chronologic age of 0.85 Ma (Azuki volcanic ash bed; see "Lithology" and Table T8); this reversal event, therefore, corresponds to the Brunhes/Matuyama boundary (0.78 Ma). Immediately below the bottom of MTD 6 (Core 333-C0018A-23H), a short interval of normal polarity is recognized (Sections 333-C0018A-24T-1, 1 cm, to 24T-4, 72 cm [190.66–194.465 mbsf]); as the Pink volcanic ash bed is recognized (age = 1.05 Ma; see "Lithology") just above this interval, this interval would correspond to the Jaramillo Subchron (0.99–1.07 Ma). Another normal polarity chron interval is found between Sections 333-C0018A-27T-2, 20 cm (219.66 mbsf), and 28T-2, 20 cm (230.26 mbsf), and may correspond with the Cobb Mountain Subchron (1.21–1.24 Ma). A few other normal polarities below Core 333-C0018A-29T are not interpreted because of insufficient data. Although it is only one data point, Sample 333-C0018A-8H-2, 14 cm (64.008 mbsf), shows negative polarity amid the Brunhes

Chron. Assuming a constant sedimentation rate, this reversal fits the Emperor excursion at 0.42 Ma; however, we leave it pending until further postcruise research reveals additional details.

An age-depth profile for the sediments at Site C0018 was constructed based on the above determined magnetostratigraphy (Fig. F24) and the sedimentation rate was calculated, accordingly. Data sets used are the Brunhes/Matuyama boundary (0.78 Ma, 122.47 mbsf), the bottom of the Jaramillo (1.07 Ma, 193.20 mbsf), and the bottom of the Cobb Mountain (1.24 Ma, 229.58 mbsf) (Table T8). Sedimentation rates above and below MTD 6 are 15.7 and 21.4 cm/k.y., respectively. These values are relatively high compared to the sedimentation rate in the Pleistocene part of Site C0004 (2.04 cm/k.y.). A very high apparent sedimentation rate of 37.08 cm/k.y. was recognized in Hole C0008A, where possible mass transport is suggested (Expedition 316 Scientists, 2009b). The depositional environment at Site C0018 is in accordance with such a high sedimentation rate.

Physical properties

The goal of physical properties measurements in Hole C0018A was to provide high-resolution data on the bulk physical properties and their downhole variations. Because Site C0018 focused on sampling MTDs inferred from seismic reflection data, the physical properties data are discussed in light of the observed MTD 6 (see "Lithology"). All physical properties measurements were made after cores had been imaged by X-ray CT and had equilibrated to room temperature (~20°C). Whole-round multisensor core logger (MSCL-W) data were collected to define natural gamma radiation, gamma ray attenuation (GRA) density, noncontact resistivity, magnetic susceptibility, and *P*-wave velocity. MSCL *P*-wave velocity data were extremely noisy and are not discussed further. Thermal conductivity was measured using the full-space needle probe method on the whole core. Penetrometer, vane shear, and electrical resistivity measurements were made shortly after the core was split, and moisture and density (MAD) analyses were performed on discrete samples collected from either the working halves of split cores or cluster samples taken adjacent to whole-round samples. Acoustic velocity and electrical resistivity on discrete samples were not measured at Site C0018 because the sediments were too soft to allow cutting appropriate samples.

MSCL-W

GRA density

GRA density was measured using the MSCL-W, based on the detection of a gamma ray beam that is produced by a cesium source. GRA density values are affected by the presence of voids and gaps between the core and core liner and thus show considerable scatter. The GRA density values will underestimate true densities where the sediment does not completely fill the liner, such as below 190.5 m core depth below seafloor (CSF), where HPCS coring ended. In general, GRA density gradually increases with depth (Fig. F30). However, GRA density decreases slightly from 58 to 70 m CSF where MAD-derived porosity increases. GRA density slightly increases within MTD 6 (127.26–188.62 m CSF) and decreases below MTD 6.

Magnetic susceptibility

Magnetic susceptibility is the degree to which a material can be magnetized by an external magnetic field. Therefore, magnetic susceptibility provides information on sediment composition. Magnetic susceptibility decreases from 20 m CSF and then shows little variation between 50 and 180 m CSF, regardless of the presence of MTDs (Fig. F30). Below the base of MTD 6, magnetic susceptibility abruptly increases.

Natural gamma radiation

Natural gamma radiation gradually increases with depth. However, a step decrease occurs between 68 and 80 m CSF, which coincides with the interval of decreasing GRA density, electrical resistivity, and porosity. Natural gamma radiation shows a slight increase at 125 m CSF and remains elevated to 190 m CSF, approximately coincident with MTD 6.

Electrical resistivity

Resistivity increases from the top of Hole C0018A to 20 m CSF, likely because of decreasing porosity.

Moisture and density measurements

MAD measurements on discrete samples from Site C0018 provide a detailed characterization of grain density, bulk density, and porosity. Samples consisting predominantly of sand-sized particles were visually noted and are plotted with distinct symbols. All MAD data are provided in Table T9 and are summarized below.

From the surface to ~200 m CSF, bulk density generally increases and porosity decreases downhole, as

expected for progressive burial (Fig. F31). A modest reversal in this trend is noted between 60 and 70 m CSF. In this interval, bulk density decreases, in both discrete and MSCL-W data, and porosity increases. Below 200 m CSF, bulk density and porosity remain relatively constant, averaging 1.90 g/cm^3 and 0.47, respectively.

Grain density averages 2.67 g/cm^3 at Site C0018. Some of the scatter in grain density data likely reflects errors in the pycnometer measurements. The scatter in grain density decreases slightly downhole as efforts were made to increase the sample volume. Bulk density and porosity show the largest scatter within the MTD zone and within the turbidites beneath the MTD zone. Reduced scatter in grain density within this zone relative to shallower measurements suggests that the bulk density and porosity scatter reflects natural variations. The scatter within the turbidites beneath the MTD likely reflects grain size variations, whereas the reason for the increased scatter within the MTD is not clear.

Strength measurements

The undrained shear strength of soft sediments in the working half of the core was measured using an analog vane shear device (Wykeham Farrance, model WF23544) and a pocket penetrometer (Geotest E284B). Strength ranges from 10.7 to 294 kPa, with an anomalously high value of 447.2 kPa when measured with the penetrometer, whereas the vane shear provides shear strength that ranges from 3 to 215.5 kPa (Fig. F32). Although there is scatter, shear strength measurements show a general trend that can be divided into successive intervals. From 0 to 30 m CSF, shear strength increases rapidly from minimal values to 50–70 kPa. The high fluid content in the uppermost meters of sediment and its progressive decrease in the first cores are likely to be responsible for this evolution. From 30 to 50 m CSF, shear strength increases to 60–90 kPa and then remains stable around these values until 120 m CSF, except between 80 and 90 m CSF where shear strength peaks at 190 kPa. Between 125 and 185 m CSF, shear strength values are higher and highly scattered with the maximum values for this site reached at the bottom of this layer. Below 190 m CSF, the values decrease and remain low and scattered. The high shear strength values between 125 and 185 m CSF may be related to MTD 6.

Electrical resistivity

Resistivity measurements were made at room temperature (25°C) with a 4-pin, 2 kHz Wenner array. Resistivity values for samples from Hole C0018A are given in Table T10. The measured values agree with the baseline values measured by the MSCL-W (Fig. F33). Measurements with the Wenner array are expected to be less affected by cracks and voids than the MSCL-W, as care was taken to select undisturbed locations. Thus, the Wenner array will provide a more accurate measure of formation resistivity than the MSCL-W. Resistivity generally increases with depth as a result of loss of pore volume (Fig. F33). A slight decrease in resistivity below 68 m CSF coincides with an increase in MAD-derived porosity and with the base of MTDs 3 and 4. A slight decrease in resistivity and increase in porosity is also observed at ~95 m CSF, coincident with the base of MTD 5. In MTD 6, resistivity increases with depth to 178 m CSF and decreases below that to the base of the MTD. The elevated resistivity observed over most of the MTD interval is consistent with observations from IODP Expedition 308 that sediments in MTDs tend to be overconsolidated (Sawyer et al., 2009). Below MTD 6, within the interval dominated by turbidites (see "Lithology"), the trend of resistivity with depth is more variable than above MTD 6.

Thermal conductivity and heat flow

The thermal conductivity results obtained for Hole C0018A are shown as a function of depth (Fig. F34). The trend of thermal conductivity with depth in Hole C0018A appears very well correlated with other physical properties, including electrical resistivity and bulk density. Therefore, thermal conductivity values can be useful not only for heat flow determination of the hole but also for an additional physical parameter, which characterizes the sedimentary formations penetrated by the hole.

The thermal gradient was estimated by linear fit of temperatures obtained by the advanced piston corer temperature tool (APCT-3), and those results are summarized in Figure F35. Two temperature measurements were taken from >150 m CSF, but they are problematic in data quality, probably due to too large frictional heat or disturbance at the coring shoe. As a result, we omitted those two points when assessing the heat flow at this site; only the four measurements from above 150 m CSF (open squares) were used. After this data screening, the mean thermal gradient value is determined as 63°C/km and the mean seafloor temperature, or the intercept temperature on the plot, is given as 1.48°C from the linear regression, whereas the measured mudline temperature at the time of APCT-3 measurements was 1.60°–2.22°C. A slightly lower intercept temperature relative to the measured mudline temperatures may reflect some natural characteristics of the thermal gradient at the topmost sediments on the seafloor

because of sediment/seawater interface physical processes or inaccuracy in the estimated mudline depth during the measurements.

Heat flow is defined as the product of temperature gradient (*dT/dz*) at a certain depth of the earth and corresponding mean thermal conductivity (k_{mean}) of the formation interval where temperature gradient is measured. Thus, heat flow in Hole C0018A is estimated by a fit of the Bullard equation (method of temperature versus integrated resistance plot). The mean heat flow value at Site C0018 is 62 mW/m^2, which is slightly higher than the previous heat flow estimates of 42–58 mW/m^2 determined for IODP NanTroSEIZE Holes C0001E, C0004D, C0008A, and C0008C in this area (Expedition 316 Scientists, 2009b). Based on the determined heat flow value as well as the thermal conductivity values that we have measured onboard, a temperature profile to the bottom of Hole C0018A is synthesized and shown in Figure **F36.** The temperature at the bottom of the hole is estimated as 19.4°C.

Inorganic geochemistry

The main geochemical objective at this site, located seaward of the megasplay, was to document the variations in interstitial water chemical composition. Such data may be used to elucidate origins, volume and nature of flow, and fluid-rock interactions that may affect the state and geotechnical properties of the formation and how they are affected by the presence of MTDs. A total of 33 interstitial water samples were squeezed from selected whole-round sections for chemical analyses. Sample depths ranged from 0 to 309 mbsf. One sample per core was collected when possible. Samples were collected at a higher spatial resolution in the uppermost 10 m in order to define the sulfate-methane transition (SMT).

Fluid recovery

Whole-round lengths ranged from 20 to 31.5 cm, with larger samples collected from cores recovered deeper within the hole where the sediments are more consolidated.

The interstitial water volumes normalized by interstitial water section length, which were recovered from whole-round sections by squeezing at a maximum pressure of 2500 pounds per square inch (17.2 MPa), are presented as a function of depth in Figure **F37A.** There is a considerable change in interstitial water recovery at ~130.5 mbsf. Interstitial water volumes per centimeter of core range from 1.95 to 2.15 mL/cm between 0 and 130.5 mbsf (Cores 333-C0018A-1H to 15H). The higher recovered volumes correspond to the less compacted lithologies. Below Core 333-C0018A-15H, the average interstitial water volume per section length fell to 1.3 ± 0.4 mL/cm; thus, the whole-round section length was increased to obtain a sufficient volume of interstitial water.

Because of the consolidated nature of the formation in the deeper portion of this site and the coring techniques used, some of the deeper cores were quite disturbed. Although we attempted to remove as much of the outer layers of the samples as possible, complete removal was not always feasible in fractured samples, and thus the interstitial waters can exhibit contamination by drilling fluid (Fig. **F37C**). Little to no drilling disturbance was noted in cores taken by HPCS, which included the SMT. The disturbed cores taken via EPCS and ESCS fell below the SMT, where in situ SO_4 concentration is expected to be 0 mM. Samples that were contaminated by drilling fluid exhibit slightly elevated SO_4 values. We used the sulfate concentration to identify and quantify contamination as indicated in **"Inorganic geochemistry"** in the "Methods" chapter (Expedition 333 Scientists, 2012). Drilling fluid contamination below the SMT reaches ~5%, thus the samples that were obtained using the EPCS and ESCS were sulfate corrected for drilling contamination following the methods of IODP Expedition 322 (Saito, Underwood, Kubo, and the Expedition 322 Scientists, 2010). Given the low levels of drilling-induced contamination in HPCS coring, these samples were not sulfate corrected. The uncorrected interstitial water data collected at Site C0018 are listed in Table **T11.** In addition, the composite uncorrected HPCS data and sulfate-corrected EPCS and ESCS data are listed in Table **T12** and illustrated in Figures **F38** and **F39.**

Salinity, chlorinity, and sodium

Interstitial water salinity rapidly decreases in the upper 30 m of Hole C0018A (Fig. **F38**). A general increase is observed from 30 to ~100 mbsf, with the trend becoming discontinuous below ~100 mbsf. The decrease in salinity in the upper ~30 m of the sediment section may reflect active sulfate reduction and the subsequent precipitation of authigenic carbonates consuming interstitial water SO_4, Ca, alkalinity, and Mg within this interval (Figs. **F38, F39**). Chlorinity increases rapidly in the upper ~30 m of Hole C0018A and then gradually increases with depth. Dissolved sodium increases in the upper ~30 m of the sediment section of Hole C0018A then broadly increases with depth to 480 mM at 308 mbsf.

Biogeochemical processes

Sulfate and alkalinity

Sulfate concentration decreases rapidly in the upper 15 m of Hole C0018A and then remains steady at less than ~0.8 mM from 15 to ~190 mbsf. SO_4 levels increase slightly from ~190 to 310 mbsf, where EPCS and ESCS coring systems were used (Fig. **F37B**). The rapid decrease in SO_4 in the upper 15 m of Hole C0018A may reflect microbial sulfate reduction. Higher SO_4 below ~190 mbsf may result from seawater intrusion due to disturbance by the coring system or the contamination with drilling fluid.

Interstitial water alkalinity increases sharply in the upper 15 mbsf of Hole C0018A, coinciding with sulfate depletion, and then remains steady at 26 mM from 15 to 29.5 mbsf. Alkalinity increases gradually from 26 mM at 29.5 mbsf to 31 mM at 84 mbsf and then gradually decreases to 22 mM from 84 to ~190 mbsf. It increases slightly at 220 mbsf and then decreases gradually to 23 mM at 308 mbsf. The elevated alkalinity in the upper 15 m of Hole C0018A reflects rapid alkalinity production in the region of intense sulfate reduction, likely occurring through methane oxidation (see **"Organic geochemistry"**).

Ammonium, phosphate, and bromide

Dissolved ammonium increases monotonically in Hole C0018A from 0.8 to ~220 mbsf. The dissolved ammonium then slightly decreases from 220 to 290 mbsf. The steady ammonium increase is interpreted as being the result of production by microbially mediated decomposition of organic matter. Ammonium remains elevated below the SMT due to ongoing organic matter degradation fueled by CO_2 reduction and higher burial rates during remobilization of sediment resulting in MTDs. The decline with depth likely reflects decreasing metabolic rates, and thus declining ammonium production, as well as NH_4 sorption on clay minerals.

Phosphate increases sharply to 128.5 µM in the upper part of Hole C0018A, peaking at 30 mbsf, and then rapidly decreases to 97 µM at 58 mbsf before starting to increase again, peaking at 114.2 µM at 84 mbsf. Below this peak, PO_4 displays an overall decreasing trend with a broad interval of negative excursion between 120 and 180 mbsf, coinciding with the occurrence of MTD 6 (see **"Lithology"**). The initial rapid increase in phosphate reflects active organic matter decomposition, which occurs below the zone of most active sulfate reduction. The decreasing and low phosphate below the depth of maximum concentration is likely controlled by the solubility of apatite, which is a major sink for phosphate.

Bromide concentration in Hole C0018A displays a monotonic increase with depth from 0.9 mM at the surface to 1.1 mM at 308 mbsf. In general, bromide is released during organic matter diagenesis and the observed trend suggests a bromide source deeper than the base of the borehole. However, the curvature of the Br/Cl profile, though chlorinity follows a constant gradient, suggests that part of the bromide is released in situ.

Major cations (Ca, Mg, and K)

Calcium in Hole C0018A decreases from 9.4 mM at the surface to 1.6 mM at 21 mbsf, below which the profile reverses and Ca gradually increases to 6.8 mM at 308 mbsf. A positive excursion coinciding with a large ash horizon at ~50 mbsf is observed. The initial decreasing trend reflects Ca consumption during authigenic carbonate formation in the zone of the most intense sulfate reduction. The increase in Ca with depth may reflect progressive ash alteration and carbonate diagenesis downhole and/or diffusion from a deeper source.

Magnesium decreases throughout Hole C0018A from 51 mM at the surface to 29 mM at 308 mbsf. The decrease is more rapid in the upper 40 m of the hole. This zone of rapid Mg depletion approximately coincides with the SO_4 reduction zone, indicating some precipitation of Mg with authigenic carbonates within this depth interval as well as uptake in clay minerals. The general decrease in Mg may indicate that uptake of magnesium in hydrous silicate minerals (mainly clays) that were formed during volcanic ash alteration.

Potassium decreases throughout Hole C0018A from 13 mM at the surface to 8.4 mM at 308 mbsf. In the upper 58 m, the values are greater than the concentration of K in seawater. This is likely a sampling artifact resulting from pressure changes during core recovery and ion exchange with NH_4 on clay surfaces. The overall decline in K likely reflects the uptake of dissolved potassium in clays and, possibly, in authigenic zeolites formed during the alteration of volcanic ash and feldspars.

Minor elements (B, Li, Si, Sr, Ba, Mn, and Fe)

Boron in Hole C0018A increases from 490 µM at the surface to 530 µM at 15 mbsf (Fig. **F38**). From 15 to ~220 mbsf, B decreases gradually to 175 µM. From 225 mbsf, B slightly decreases to 170 µM at 308 mbsf. Boron concentration decreases with depth is commonly observed in marine sediment and generally attributed to boron uptake in clays at low temperature.

Lithium rapidly decreases from 42 µM at the surface to 21 µM at 21 mbsf. Below 21 mbsf, Li gradually increases to 49 µM at 308 mbsf with a positive excursion at 122 mbsf, which may correspond to the volcaniclastic material observed at ~125 mbsf (see "Lithology" results).

Dissolved silica is higher than modern values at all depths, though no Si trend is apparent.

Strontium is discontinuous, ranging from 73 to 83 µM in the upper ~30 m of Hole C0018A, and then increases from 71 µM at 40 mbsf to 85 µM at 160 mbsf with two negative excursions at 122 and 144 mbsf, which may correspond to volcanic material and a chaotic bedding interval, respectively. Between ~170 and ~190 mbsf, Sr is generally lower, ranging from 75 to 81 µM. This may correspond to a region of slightly higher density observed at this interval (see "Physical properties"). Below 223 mbsf, Sr increases with depth to 95 µM at 308 mbsf.

Barium is not detected above 10 mbsf and exhibits a rapid increase across the SMT from 5.2 µM at 11.5 mbsf to 184 µM at 21 mbsf. Ba decreases with depth from 100 µM at 30 mbsf to 21 µM at 244 mbsf and then increases slightly with depth to 28.5 µM at 308 mbsf.

Dissolved manganese rapidly decreases in Hole C0018A from 27.5 µM at the surface to 0.2 µM at 15 mbsf. Below 15 mbsf, Mn is relatively constant around >2 µM. Some increased intervals can be recognized at ~70 and ~190 mbsf. The rapid increase of dissolved Mn in the upper 15 m at this site may reflect MnO_2 reduction by microbially mediated organic matter decomposition.

Dissolved iron exhibits considerable variability throughout Hole C0018A.

Trace elements (Rb, Cs, V, Cu, Zn, Mo, Pb, and U)

Rubidium at Hole C0018A shows a rapid decrease from 2000 nM at the surface to 1350 nM at 20 mbsf, followed by a gradual decrease to 1200 nM at ~300 mbsf (Fig. F40).

Cesium rapidly decreases from 5.4 nM at the surface to 3.2 nM at 20 mbsf then increases to 6.3 nM at ~110 mbsf. This is followed by a decrease to 4.5 nM at ~200 mbsf. Below this depth concentrations are generally higher and more variable.

Vanadium scatters in the upper 21 m of Hole C0018A. V then increases from 95 nM at 29 mbsf to 125 nM at 58 mbsf, below which it rapidly declines to 65 nM at 68 mbsf. Below 68 mbsf, vanadium increases to 110 nM at 122 mbsf, followed by a rapid decline to 54 nM at 130 mbsf. Below 130 mbsf, V remains relatively constant at ~50 nM.

Copper is relatively depleted (<100 nM) from 15 to 100 mbsf in Hole C0018A compared with the surface (averages 1000 ± 300 nM from 0 to 15 mbsf) with the exception of a positive excursion to 2830 nM at 39 mbsf, which corresponds to a zone of mixed sediment as described in "Lithology." Below 100 mbsf, Cu exhibits a wide range.

Zinc rapidly decreases in the upper ~20 mbsf of Hole C0018A from ~1500 to 130 nM, followed by a broad increase to ~2500 nM at ~300 mbsf.

Molybdenum exhibits considerable variability throughout Hole C0018A, ranging from ~50 nM to ~350 nM. An interval of low concentration (generally <50 nM from 4 to 23 mbsf) is observed.

Lead is generally low in Hole C0018A. The average background concentration is 1.07 ± 0.74 nM.

Uranium is generally low throughout with small peaks observed at ~50, ~100, and ~175 mbsf.

Organic geochemistry

Hydrocarbon gas

Concentrations of methane and ethane, as well as the ratios of methane to ethane (C1/C2) are shown in Table T13 and Figure F41. Methane is predominant in all Hole C0018A cores except in Core 333-C0018A-1H, where no hydrocarbon gas was detected. Methane concentration ranges between 0 and 19,338.7 parts per million by volume (ppmv), with an average of 6,949.5 ppmv. Ethane was sporadically detected in Hole C0018A and only present in low concentrations, with a maximum value of 1.6 ppmv. No heavier hydrocarbon gases were found. The C1/C2 ratios for all cores are >4000, suggesting methane is mostly biogenic and organic matter is immature in Hole C0018A.

Relatively high methane concentration occurs at two depth intervals. The first interval occurs approximately between 17 and 50 mbsf, corresponding to the SMT zone (see "Inorganic geochemistry") and indicating increases in methanogenesis. The second interval is between 201.5 and 239.5 mbsf, where methane concentration rises to the maximum value.

Sediment carbon, nitrogen, and sulfur composition

Calcium carbonate ($CaCO_3$) content varies in a wide range from 0.22 to 25.36 wt% and averages 8.52% throughout Hole C0018A (Table T14; Fig. F42). Most high values (i.e., >15 wt%) are found in the upper

~86 mbsf, where the values average 13.22 wt% and are highly variable between 0.22 and 25.36 wt%. $CaCO_3$ concentration between ~86 and ~191 mbsf displays a lower average of 9.55 wt% and a smaller variation range of 1.77–17.85 wt%. Below 191 mbsf, the amounts of $CaCO_3$ are less variable and generally low, averaging 3.13 ± 1.75 wt%. The change in $CaCO_3$ concentration is correspondent with lithologic Subunits IA and IB (see **"Lithology"**).

Total organic carbon (TOC), total nitrogen (TN), and total sulfur (TS) contents are low in the majority of cores (Table **T14;** Fig. **F42**). TOC and TN concentrations show a positive correlation (r^2 = 0.74). Similar to the $CaCO_3$ content, TOC and TN values show large variations in the upper 71 mbsf. TOC content ranges from 0.03 to 0.96 wt% with an average of 0.50 wt%, whereas TN values are from 0.01 to 0.12 wt% with an average of 0.07 wt%. Higher values are concentrated in the upper 20 mbsf, which is perhaps due to less diagenetic alterations in the shallow sediments. TOC and TN contents are less variable between ~87 and ~191 mbsf, averaging 0.49 ± 0.09 wt% and 0.07 ± 0.01wt%, respectively. Values become more sporadic below 191 mbsf, averaging 0.47 ± 0.11 wt% for TOC and 0.06 ± 0.02 wt% for TN. The TOC to TN atomic ratios (TOC/TN_{at}) fall in the range of 3.5–15, suggesting the organic matter is predominately marine derived but also contains terrigenous material in some horizons. TS concentration varies from 0.04 to 1.19 wt% and averages 0.28 wt%. The samples show elevated TS content between ~90 and 130 mbsf, which can be associated with the occurrence of pyrite at ~120 mbsf (see **"Lithology"**).

Rock-Eval pyrolysis

Thirty samples were measured by Rock-Eval pyrolysis to characterize the type and maturity of organic matter (Table **T15;** Fig. **F43**). Rock-Eval T_{max} values are <430°C in all but one sample, indicating that the organic matter in Hole C0018A is thermally immature. The amounts of free hydrocarbon (S1) range between 0 and 0.12 mg hydrocarbon/g sediment (mg HC/g sediment). Thermal cracking of nonvolatile organic matter released hydrocarbon (S2) is between 0.01 and 0.80 mg HC/g sediment. Production index (PI) ranges between 0 and 0.14, further indicating the immaturity of the organic matter.

Hydrogen index (HI) values <100 mg HC/g TOC are typical of terrigenous organic matter, whereas HI values of 300–800 are generally attributed to a marine source (Tissot and Welte, 1984). The HI values in Hole C0018A are rather low, varying between 9 and 93 mg HC/g TOC. The contradiction between low HI values and contemporarily low TOC/TN_{at} ratios may be related to the low TOC content in our samples, which can artificially lower HI values due to the adsorption of hydrocarbons onto clay minerals (Espitalié et al., 1985). In addition, intensive degradation can preferentially remove hydrogen-rich organic matter and further lower HI values (Espitalié et al., 1977).

References

Bouma, A.H., 1962. *Sedimentology of Some Flysch Deposits: A Graphic Approach to Facies Interpretation:* Amsterdam (Elsevier).

Conin, M., Henry, P., Bourlange, S., Raimbourg, H., and Reuschlé, T., 2011. Interpretation of porosity and LWD resistivity from the Nankai accretionary wedge in light of clay physicochemical properties: evidence for erosion and local overpressuring. *Geochem., Geophys., Geosyst.,* 12:Q0AD07. **doi:10.1029/2010GC003381**

Espitalié, J., Laporte, J.L., Madec, M., Marquis, F., Leplat, P., Paulet, J., and Boutefeu, A., 1977. Méthode rapide de caractérisation des roches mètres, de leur potentiel pétrolier et de leur degré d'évolution. *Rev. Inst. Fr. Pet.,* 32(1):23–42. **doi:10.2516/ogst:1977002**

Espitalié, J., Senga Makadi, K., and Trichet, J., 1985. Role of the mineral matrix during kerogen pyrolysis. *In* Schenck, P.A. (Ed.), *Advances in Organic Geochemistry 1983:* Oxford (Pergamon Press).

Expedition 316 Scientists, 2009a. Expedition 316 Site C0004. *In* Kinoshita, M., Tobin, H., Ashi, J., Kimura, G., Lallemant, S., Screaton, E.J., Curewitz, D., Masago, H., Moe, K.T., and the Expedition 314/315/316 Scientists, *Proc. IODP,* 314/315/316: Washington, DC (Integrated Ocean Drilling Program Management International, Inc.). **doi:10.2204/iodp.proc.314315316.133.2009**

Expedition 316 Scientists, 2009b. Expedition 316 Site C0008. *In* Kinoshita, M., Tobin, H., Ashi, J., Kimura, G., Lallemant, S., Screaton, E.J., Curewitz, D., Masago, H., Moe, K.T., and the Expedition 314/315/316 Scientists, *Proc. IODP,* 314/315/316: Washington, DC (Integrated Ocean Drilling Program Management International, Inc.). **doi:10.2204/iodp.proc.314315316.136.2009**

Expedition 333 Scientists, 2012. Methods. *In* Henry, P., Kanamatsu, T., Moe, K., and the Expedition 333 Scientists, *Proc. IODP,* 333: Tokyo (Integrated Ocean Drilling Program Management International, Inc.). **doi:10.2204/iodp.proc.333.102.2012**

Gee, J., Staudigel, H., and Tauxe, L., 1989. Contribution of induced magnetization to magnetization of seamounts. *Nature (London, U. K.),* 342(6246):170–173. **doi:10.1038/342170a0**

Hayashida, A., Kamata, H., and Danhara, T., 1996. Correlation of widespread tephra deposits based on paleomagnetic directions: link between a volcanic field and sedimentary sequences in Japan. *Quat. Int.,* 34–36:89–98. **doi:10.1016/1040-6182(95)00072-0**

Heki, K., 2007. Secular, transient, and seasonal crustal movements in Japan from a dense GPS array: implica-

tion for plate dynamics in convergent boundaries. *In* Dixon, T.H., and Moore, J.C. (Eds.), *The Seismogenic Zone of Subduction Thrust Faults:* New York (Columbia Univ. Press), 512–539.

Kimura, G., Moore, G.F., Strasser, M., Screaton, E., Curewitz, D., Streiff, C., and Tobin, H., 2011. Spatial and temporal evolution of the megasplay fault in the Nankai Trough. *Geochem., Geophys., Geosyst.,* 12:Q0A008. **doi:10.1029/2010GC003335**

Kinoshita, M., Tobin, H., Ashi, J., Kimura, G., Lallemant, S., Screaton, E.J., Curewitz, D., Masago, H., Moe, K.T., and the Expedition 314/315/316 Scientists, 2009. *Proc. IODP,* 314/315/316: Washington, DC (Integrated Ocean Drilling Program Management International, Inc.). **doi:10.2204/iodp.proc.314315316.2009**

Moore, G.F., Bangs, N.L., Taira, A., Kuramoto, S., Pangborn, E., and Tobin, H.J., 2007. Three-dimensional splay fault geometry and implications for tsunami generation. *Science,* 318(5853):1128–1131. **doi:10.1126/science.1147195**

Raffi, I., Backman, J., Fornaciari, E., Pälike, H., Rio, D., Lourens, L., and Hilgen, F., 2006. A review of calcareous nannofossil astrobiochronology encompassing the past 25 million years. *Quat. Sci. Rev.,* 25(23–24):3113–3137. **doi:10.1016/j.quascirev.2006.07.007**

Saito, S., Underwood, M.B., Kubo, Y., and the Expedition 322 Scientists, 2010. *Proc. IODP,* 322: Tokyo (Integrated Ocean Drilling Program management International, Inc.). **doi:10.2204/iodp.proc.322.2010**

Sawyer, D.E., Flemings, P.B., Dugan, B., and Germaine, J.T., 2009. Retrogressive failures recorded in mass transport deposits in the Ursa Basin, northern Gulf of Mexico. *J. Geophys. Res., [Solid Earth],* 114(B10):B10102. **doi:10.1029/2008JB006159**

Seno, T., Stein, S., and Gripp, A.E., 1993. A model for the motion of the Philippine Sea plate consistent with NUVEL-1 and geological data. *J. Geophys. Res., [Solid Earth],* 98(B10):17941–17948. **doi:10.1029/93JB00782**

Strasser, M., Moore, G.F., Kimura, G., Kitamura, Y., Kopf, A.J., Lallemant, S., Park, J.-O., Screaton, E.J., Su, X., Underwood, M.B., and Zhao, X., 2009. Origin and evolution of a splay fault in the Nankai accretionary wedge. *Nat. Geosci.,* 2(9):648–652. **doi:10.1038/ngeo609**

Strasser, M., Moore, G.F., Kimura, G., Kopf, A.J., Underwood, M.B., Guo, J., and Screaton, E.J., 2011. Slumping and mass-transport deposition in the Nankai forearc: evidence from IODP drilling and 3-D reflection seismic data. *Geochem., Geophys., Geosyst.,* 12:Q0AD13. **doi:10.1029/2010GC003431**

Tissot, B.P., and Welte, D.H., 1984. *Petroleum Formation and Occurrence* (2nd ed.): Heidelberg (Springer-Verlag).

Zhao, X., Roperch, P., and Stokking, L.B., 1994. Magnetostratigraphy of the north Aoba Basin. *In* Greene, H.G., Collot, J.-Y., Stokking, L.B., et al., *Proc. ODP, Sci. Results,* 134: College Station, TX (Ocean Drilling Program), 457–474. **doi:10.2973/odp.proc.sr.134.025.1994**

Publication: 18 May 2012
MS 333-103

Figure F1. Detailed bathymetry and structure around Site C0018 at the footwall of the splay fault (Strasser et al., 2011). Block diagram and multichannel seismic cross-lines (XLs). IL = in-line. VE = vertical exaggeration.

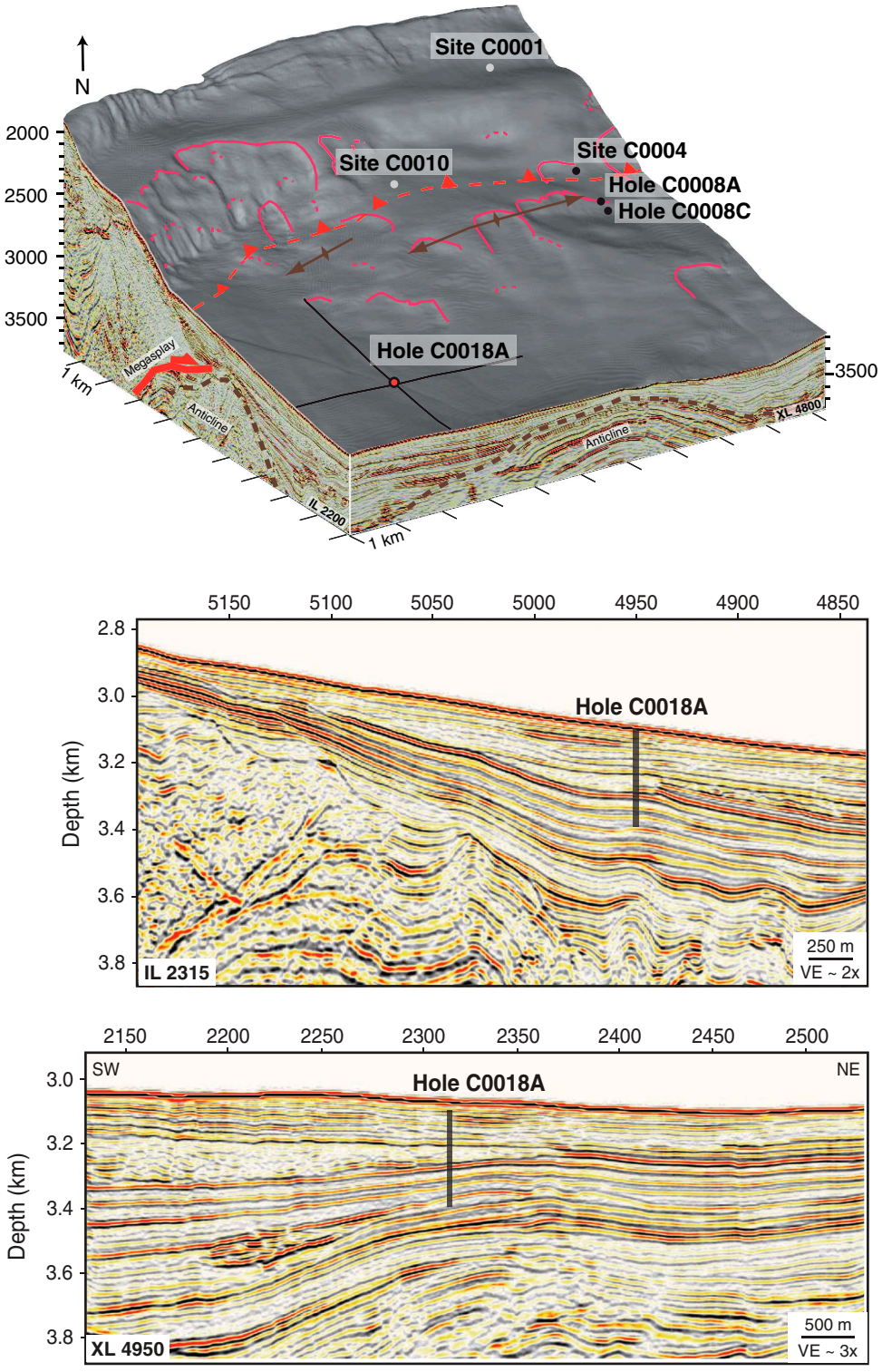

Figure F2. Bathymetric map, with 2-D multichannel seismic profile locations, NanTroSEIZE Stage 1 and 2 drill sites (white circles), and Expedition 333 drill sites (red circles). White barbed line = position of deformation front of accretionary prism, yellow arrow = estimated far-field vectors between Philippine Sea plate and Japan (Seno et al. 1993; Heki, 2007).

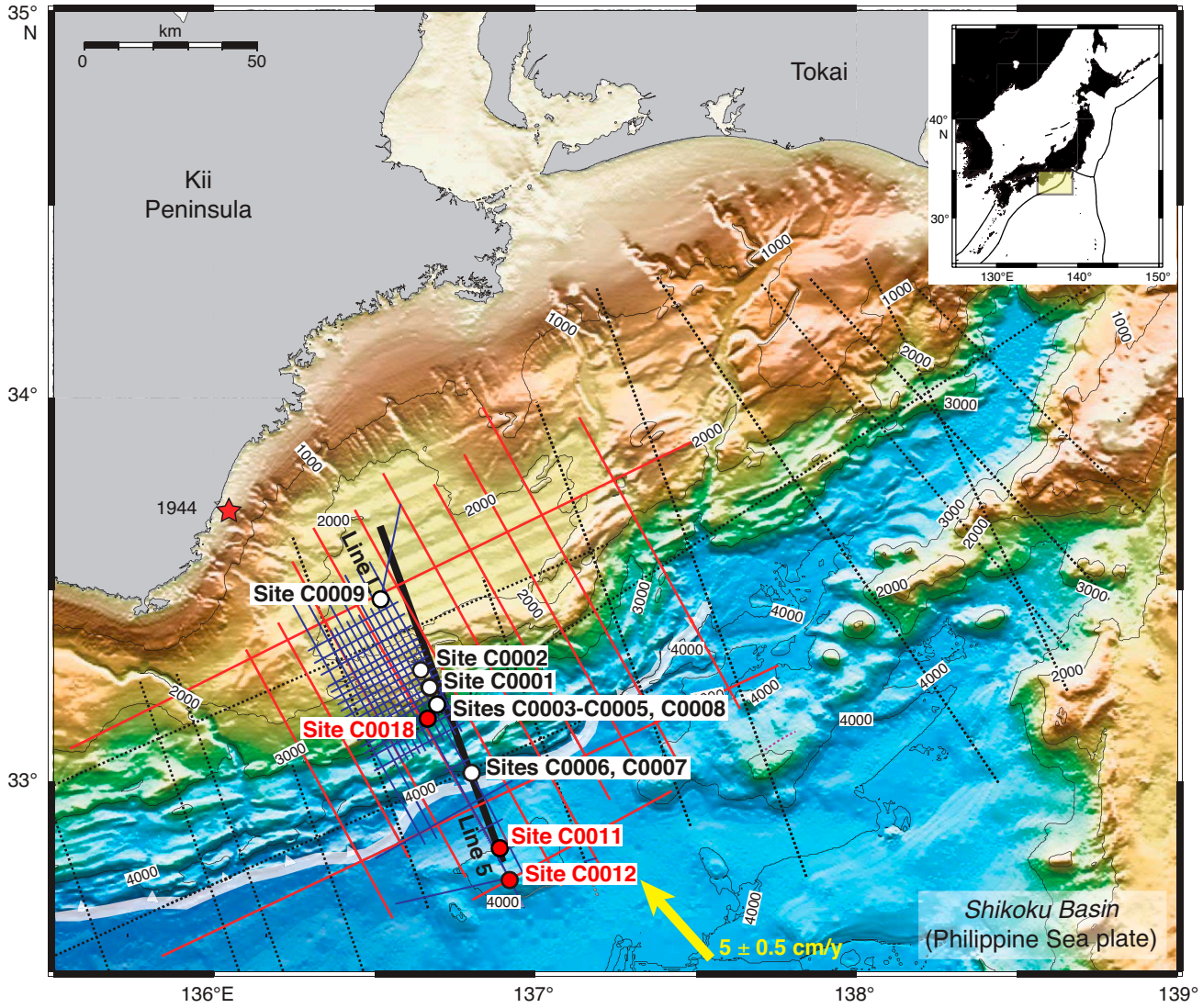

Figure F3. Schematic sedimentary log of Hole C00018A, showing main units and facies interpreted, recovery rates, and relative depths of drilled intervals with mass transport deposits (MTDs).

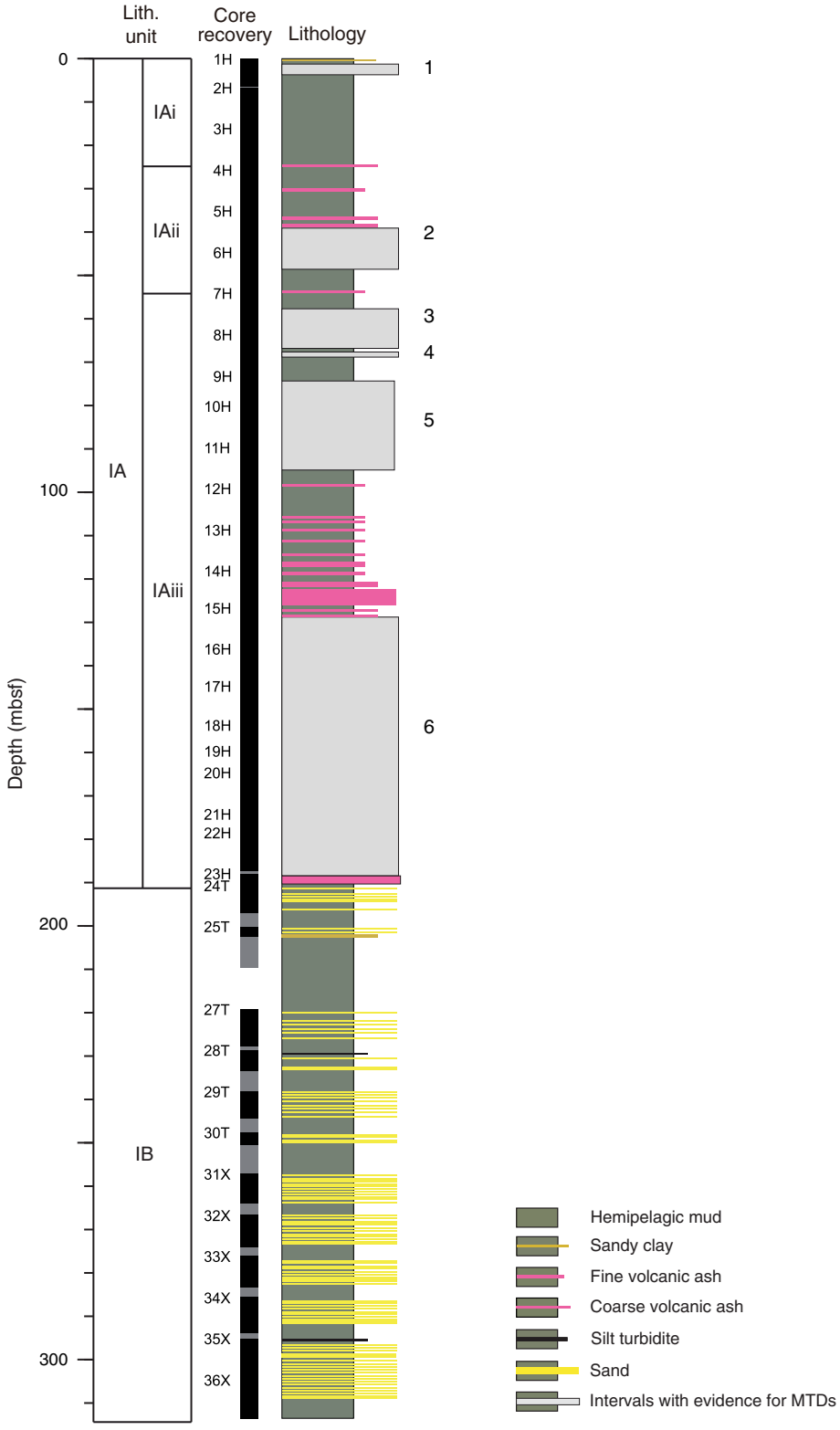

Figure F4. Relative occurrence and thickness of ash and sand, Hole C0018A. MTD = mass transport deposit.

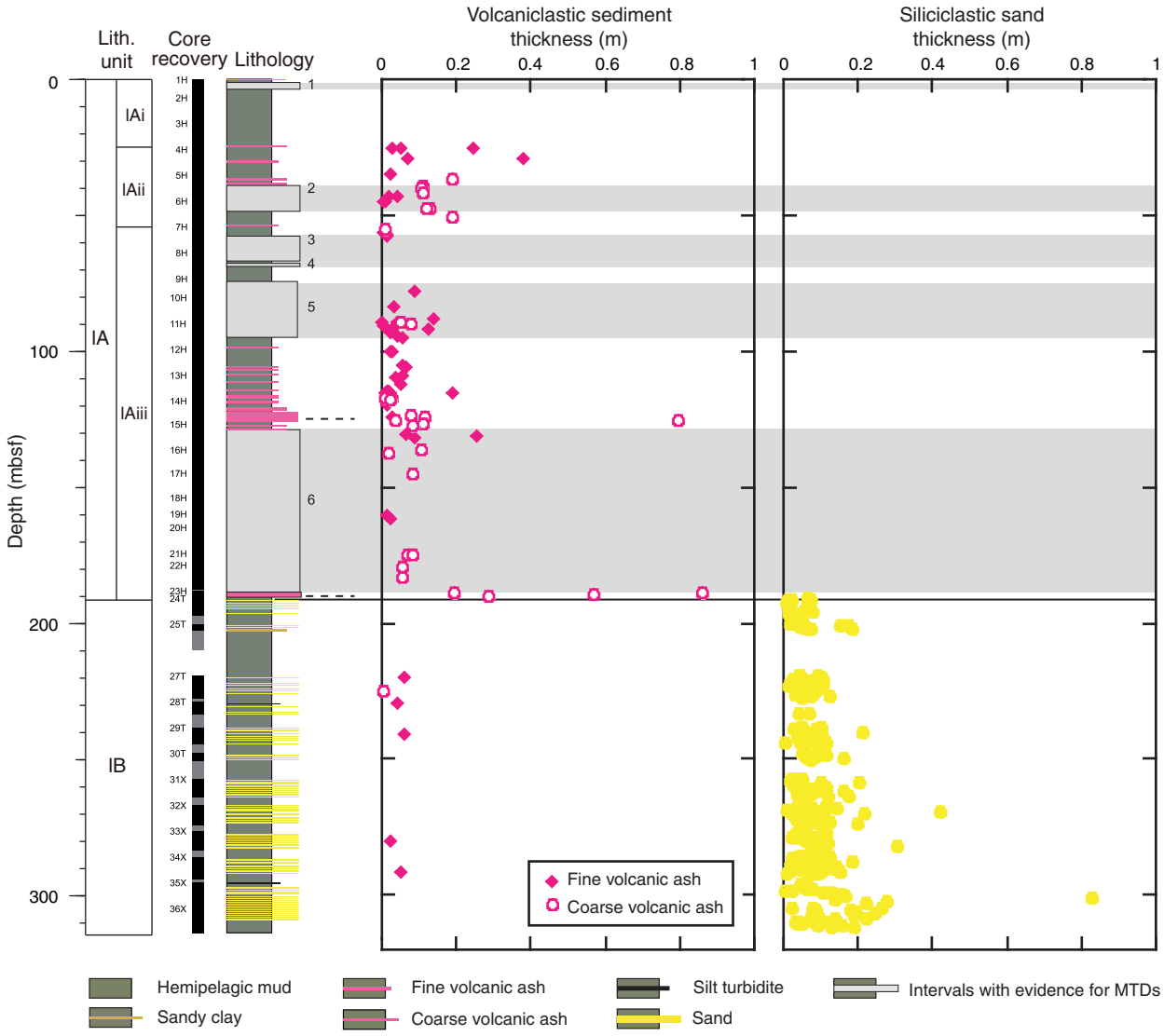

Figure F5. Summary of XRD data, Hole C0018A. Note the sharp change in composition across the Subunit IA/IB boundary. MTD = mass transport deposit.

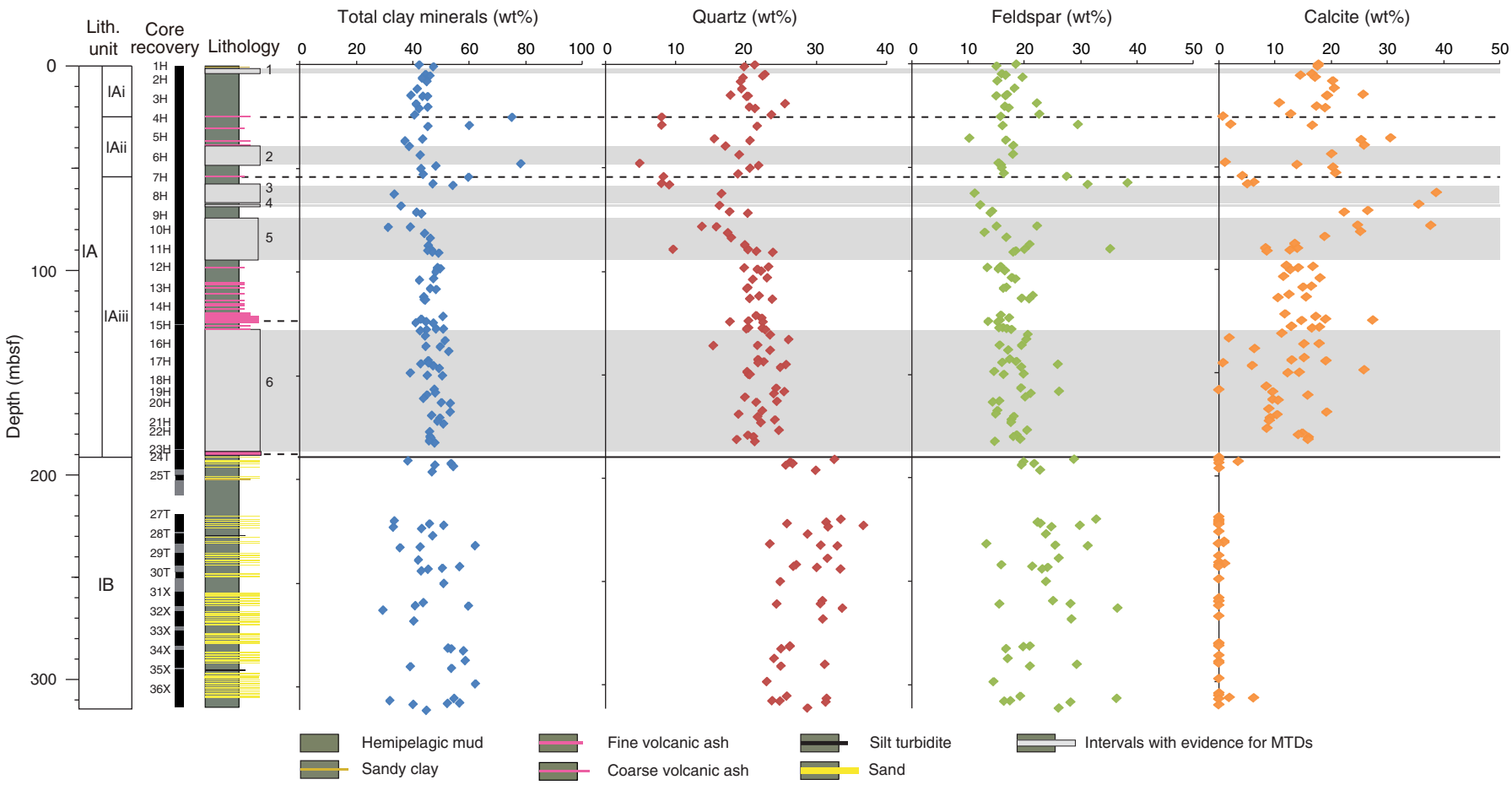

Figure F6. Top of MTD 2 in Section 333-C0018A-5H-5 showing chaotic facies and overlying turbidite. **A.** Core photo. **B.** Computed tomography (CT) scan. **C.** CT scan 3-D rendering.

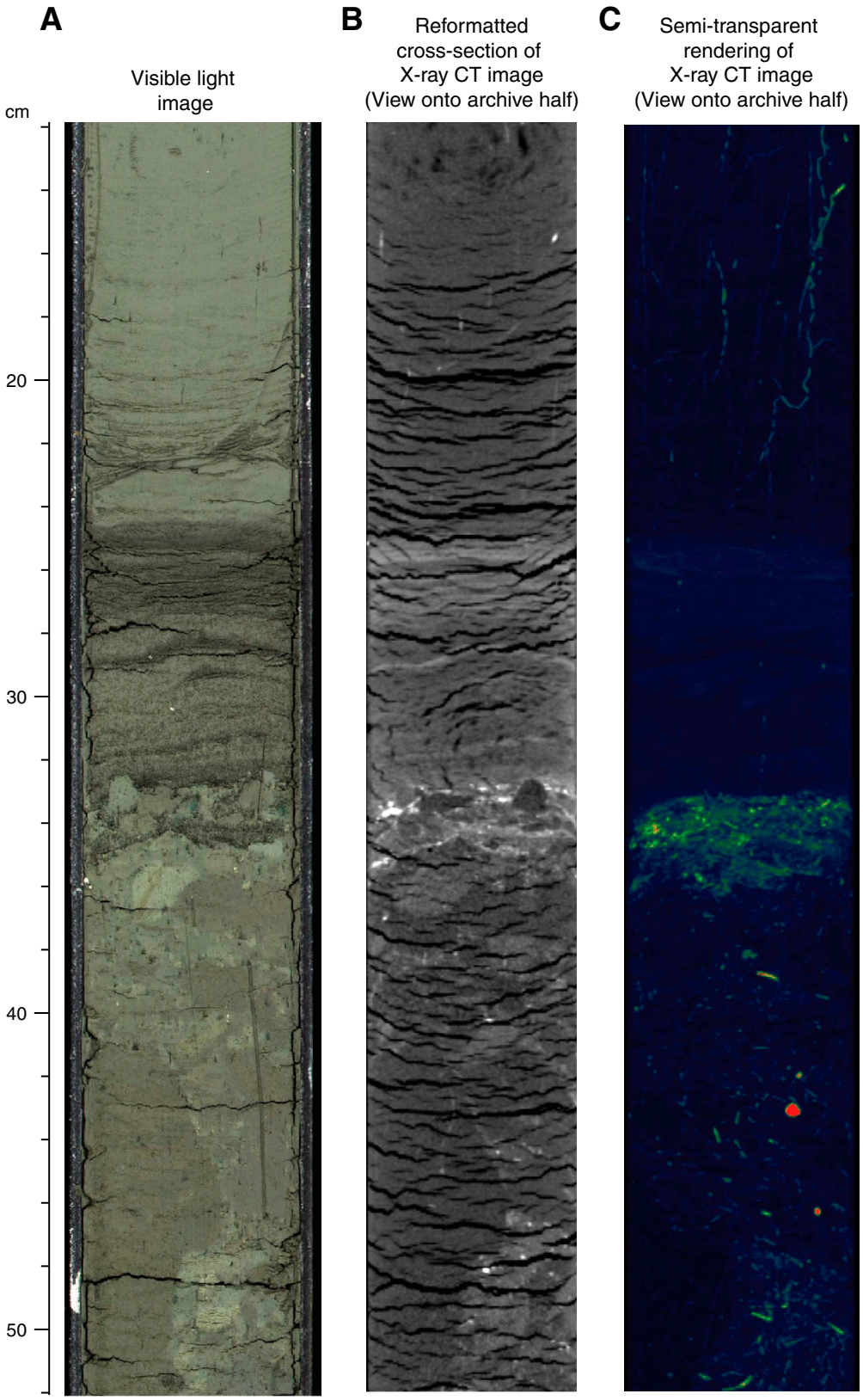

Figure F7. Shear zone at base of MTD 2 in Section 333-C0018A-6H-2. **A.** Core photo. **B.** Computed tomography (CT) scan. **C.** CT scan 3-D rendering showing high CT pyrite lines.

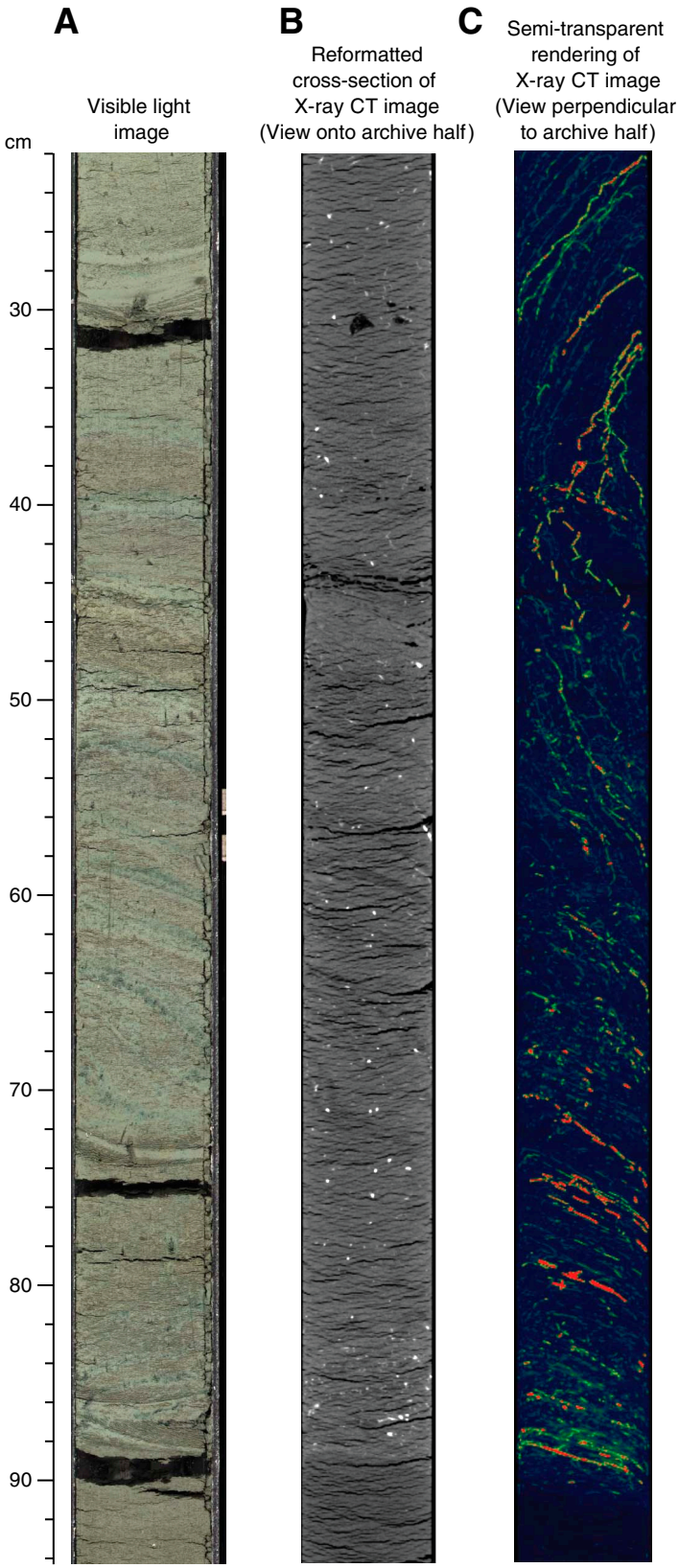

Figure F8. A. Core photo of a fluidized ash layer, corresponding to MTD 4, Subunit IA. **B.** Core photo of sand-sized volcaniclastic layer, likely correlated to the onland Azuki volcanic ash bed. **C.** Detail of this sand layer (Section 333-C0018A-14H-8, 46 cm). This sand is composed of pumice, volcanic lithic fragments, metamorphic lithic fragments, quartz, feldspar, and foraminifers. **D.** Smear slide photo (Section 333-C0018A-14H-8, 77 cm) showing that this ash is mainly composed of volcanic glass shards with minor amounts of hornblende, orthopyroxene, and clinopyroxene. At the center of the photo, an obsidian fragment is visible, which is characteristic of the Azuki volcanic ash bed. **E.** Smear slide photo of volcanic ash tentatively correlated to the Pink volcanic ash bed (Section 333-C0018A-23H-3, 49 cm), based on characteristic microscopic features showing bubble wall volcanic glass shards and minor amount of hornblende.

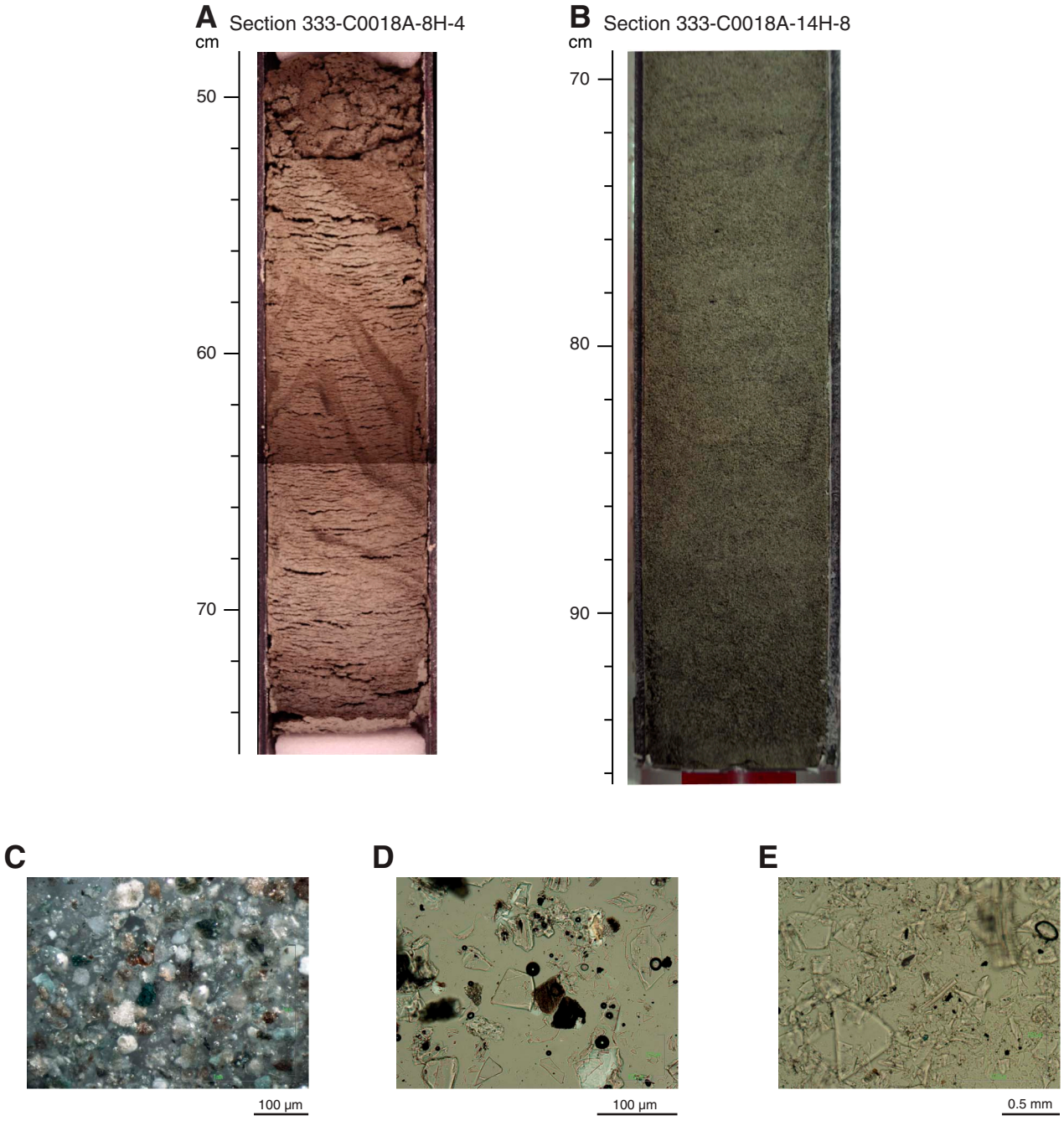

Figure F9. Photos showing the style of internal deformation within MTD 6.

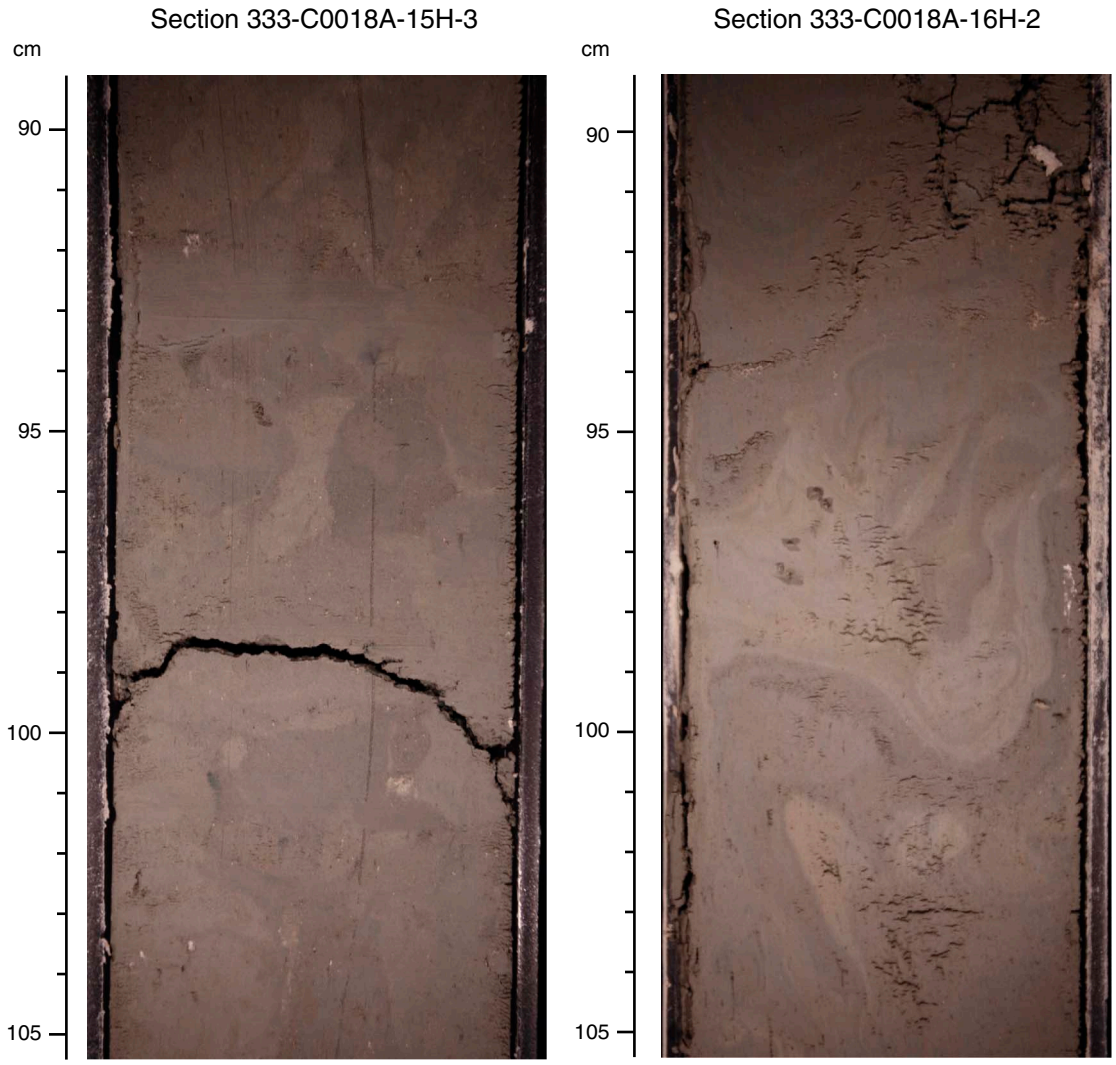

Figure F10. A. Core photo from a cyclic succession of turbidites showing fining-upward trends. **B.** Smear slide denoting sand and lithic grains in the turbidite succession. **C.** Detail showing erosion at the base of turbidite deposits occurring in Subunit IB.

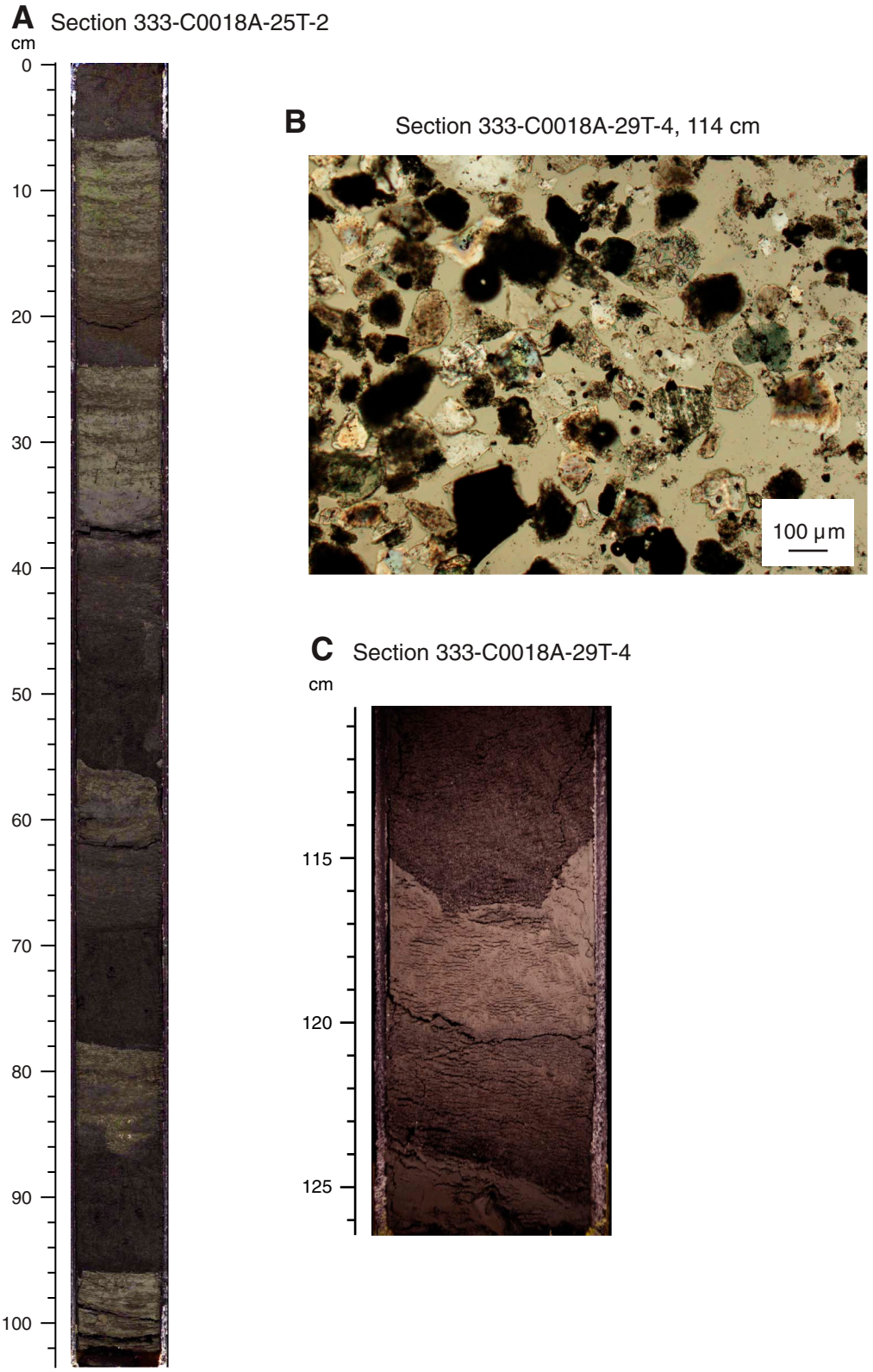

Figure F11. Discrete X-ray fluorescence major element (SiO_2, Al_2O_3, CaO, Fe_2O_3, MgO and TiO_2) composition as a function of depth, Hole C0018A. MTD = mass transport deposit.

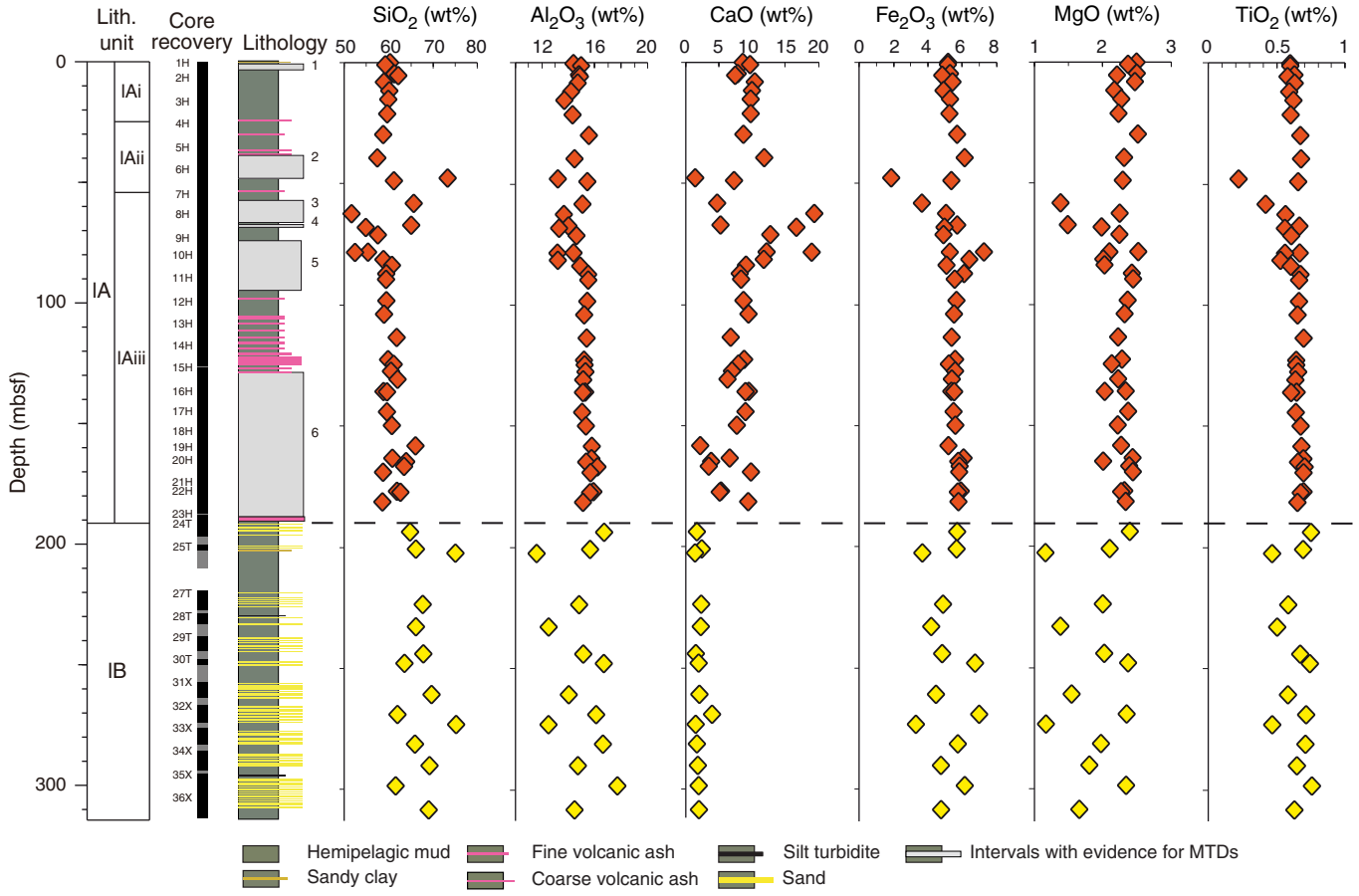

Figure F12. Distribution of bedding dip angles and deformation structures with depth, Hole C0018A. Gray intervals = location of mass transport deposits (MTDs).

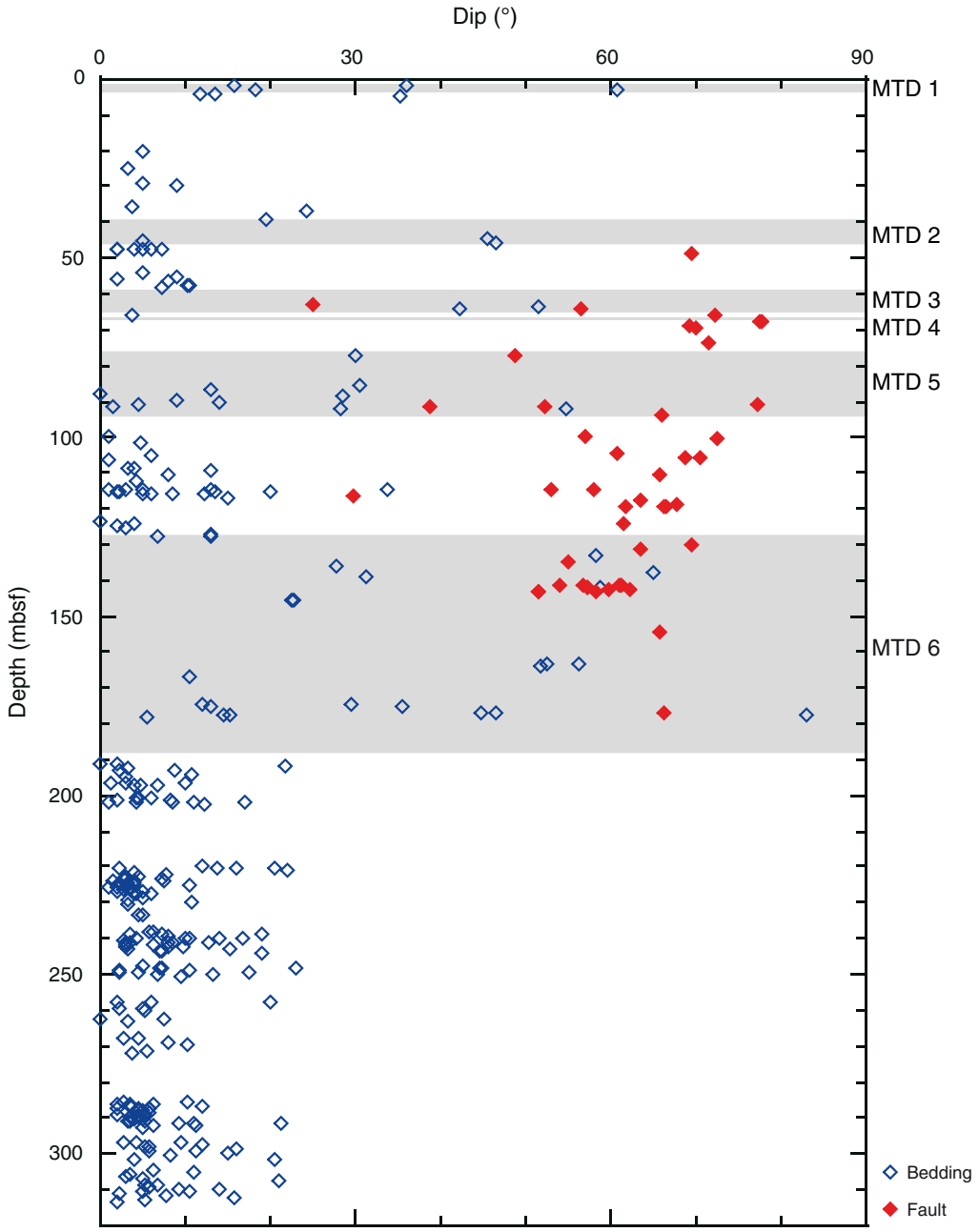

Figure F13. Lower hemisphere equal area projection of poles to bedding, above MTD 6 of Subunit IA in Hole C0018A.

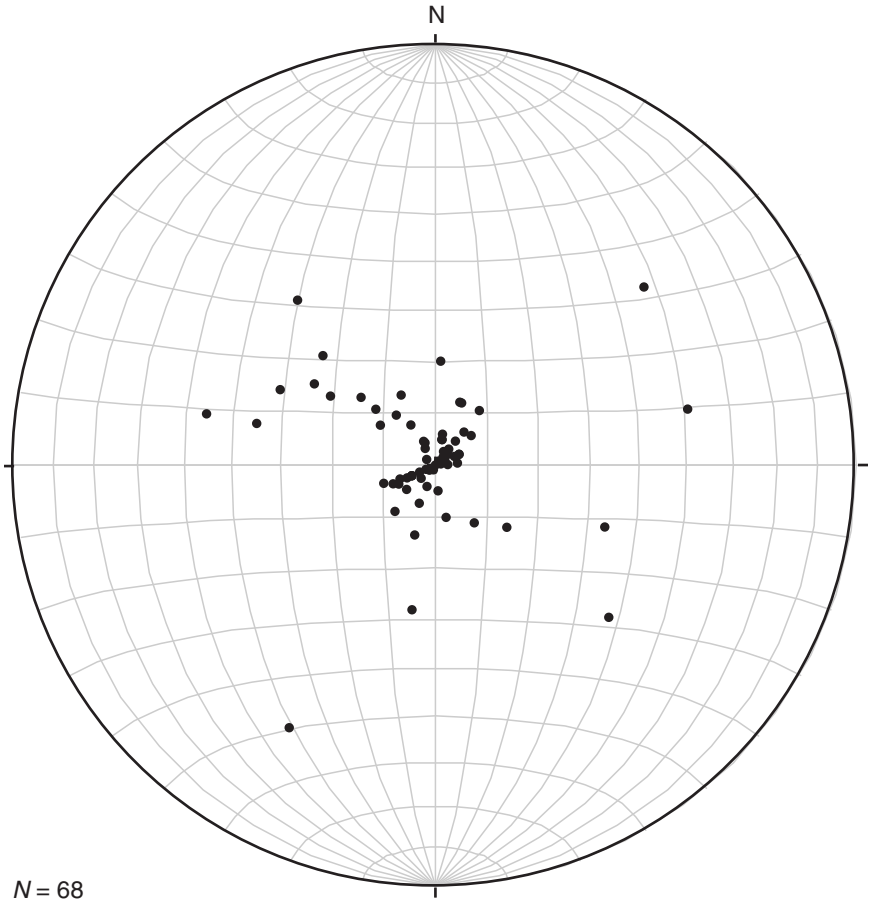

Figure F14. A. Normal fault within Subunit IA (interval 333-C0018A-8H-8, 8–21 cm). Note that the fault offsets a burrow. Offset = 8 mm. MSCL-I = photo image logger, CT = computed tomography. (Continued on next page.)

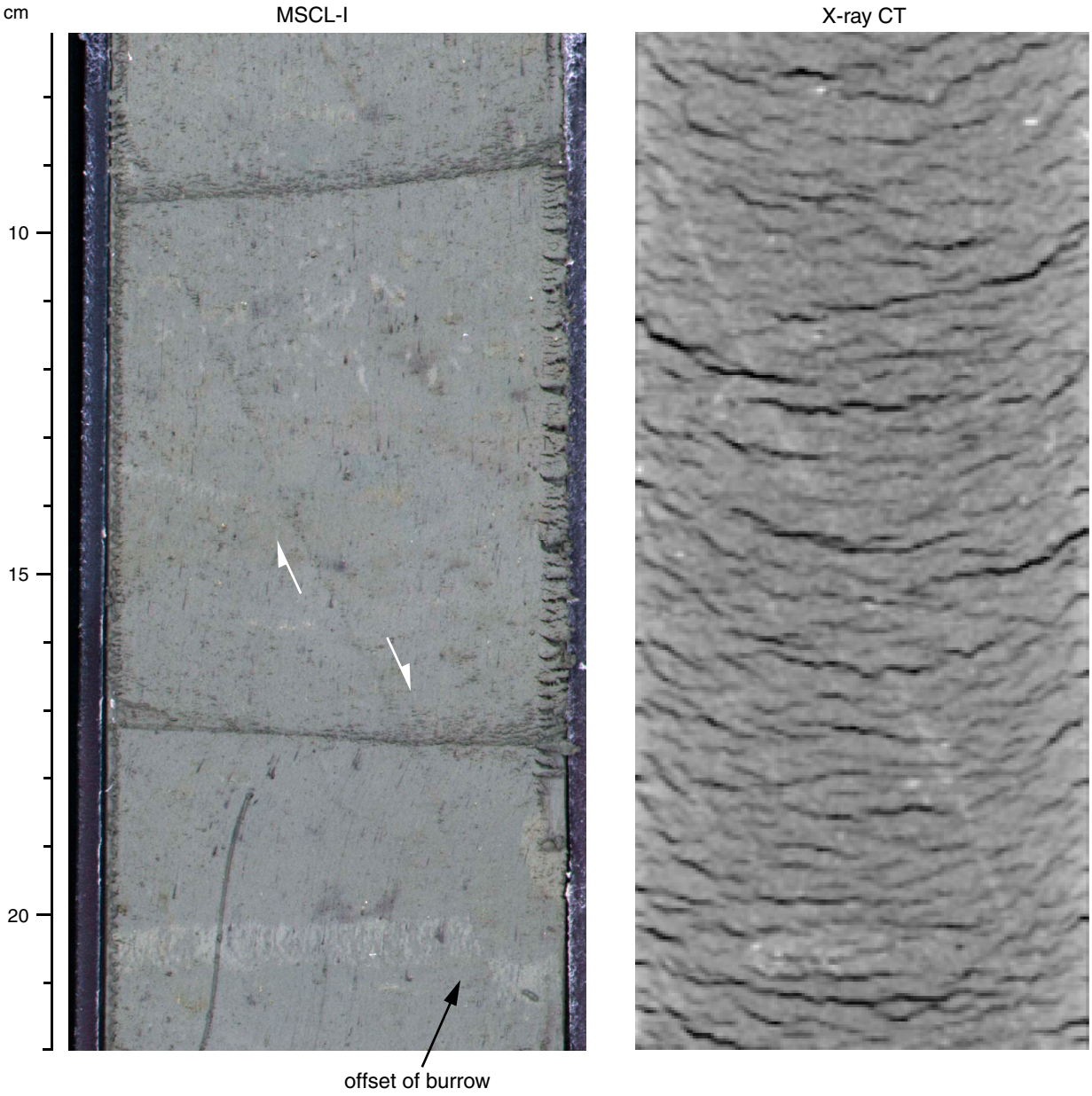

Figure F14 (continued). B. Reverse fault within Subunit IA (interval 333-C0018A-13H-9, 6–14 cm). Offset = 20 mm.

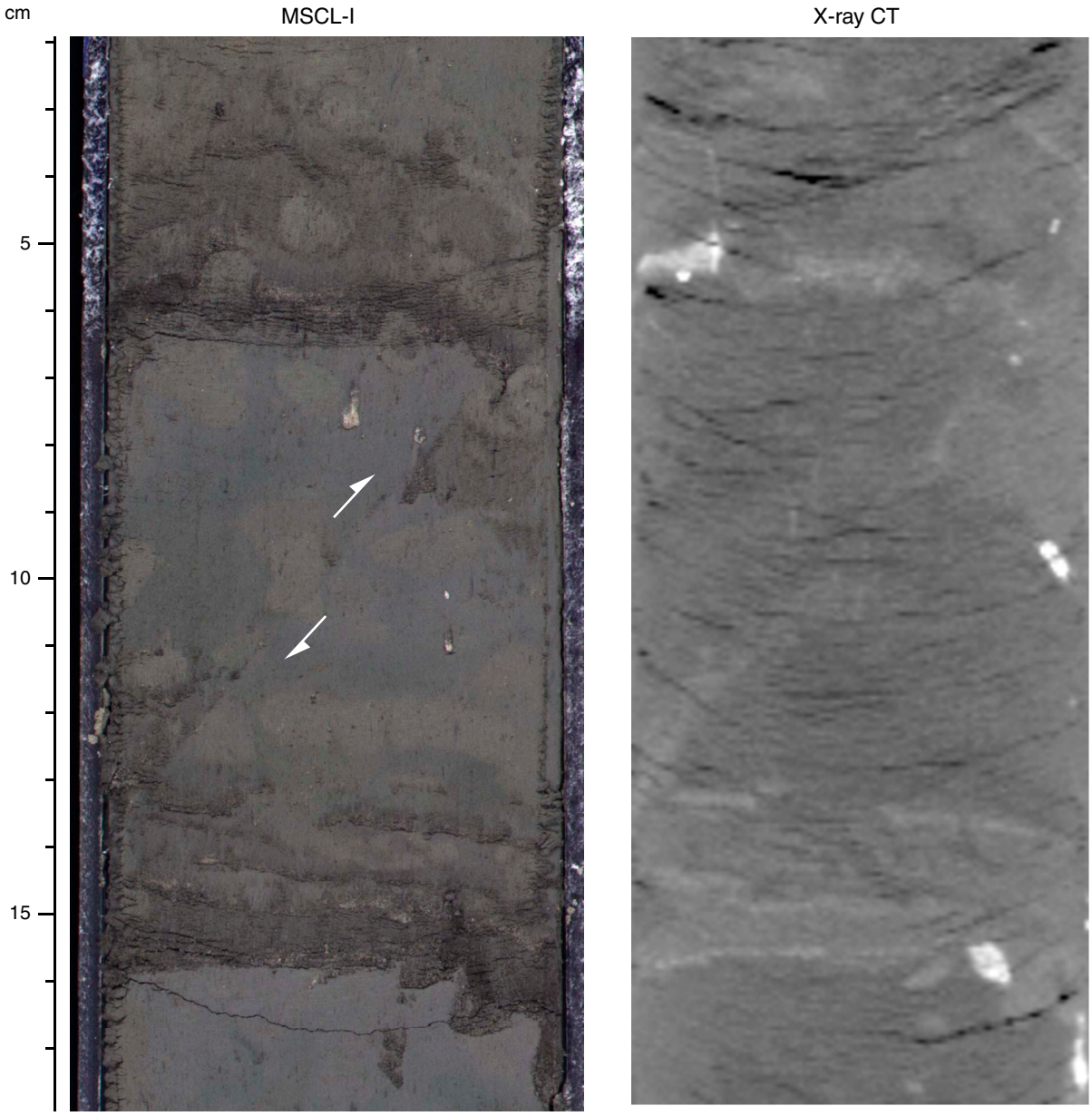

Figure F15. Lower hemisphere equal area projection of poles to fault, Hole C0018A Subunit IA.

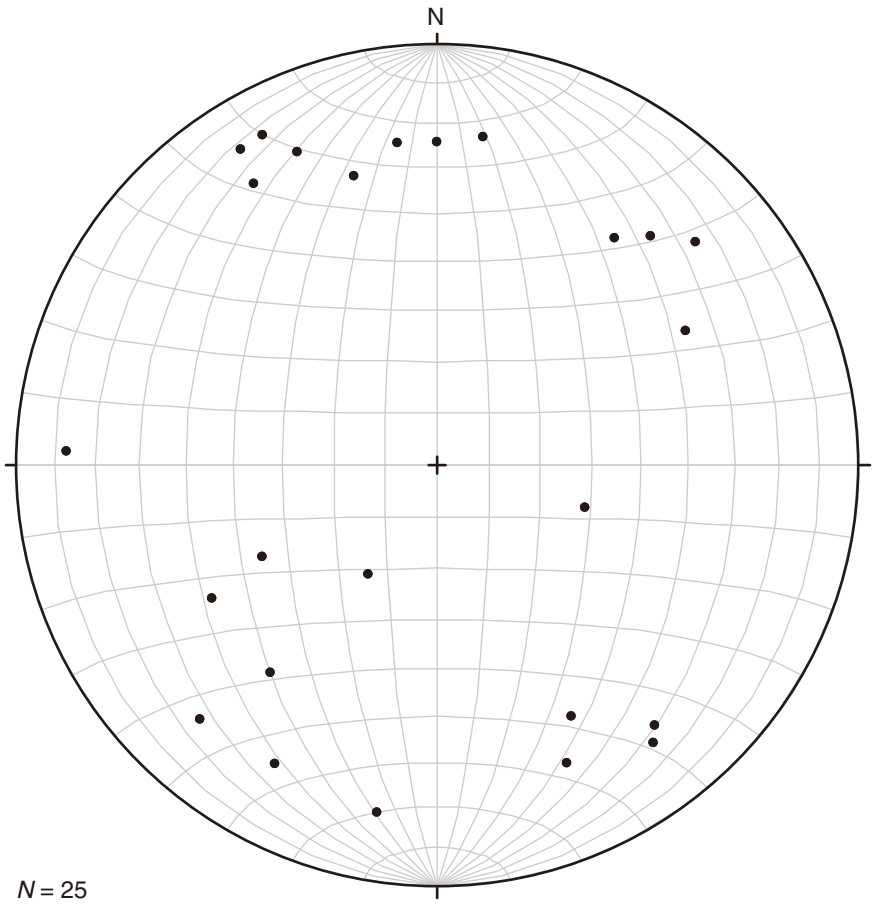

Figure F16. Appearance of a slump fold (interval 333-C0018A-5H-6, 76–84 cm). MSCL-I = photo image logger, CT = computed tomography.

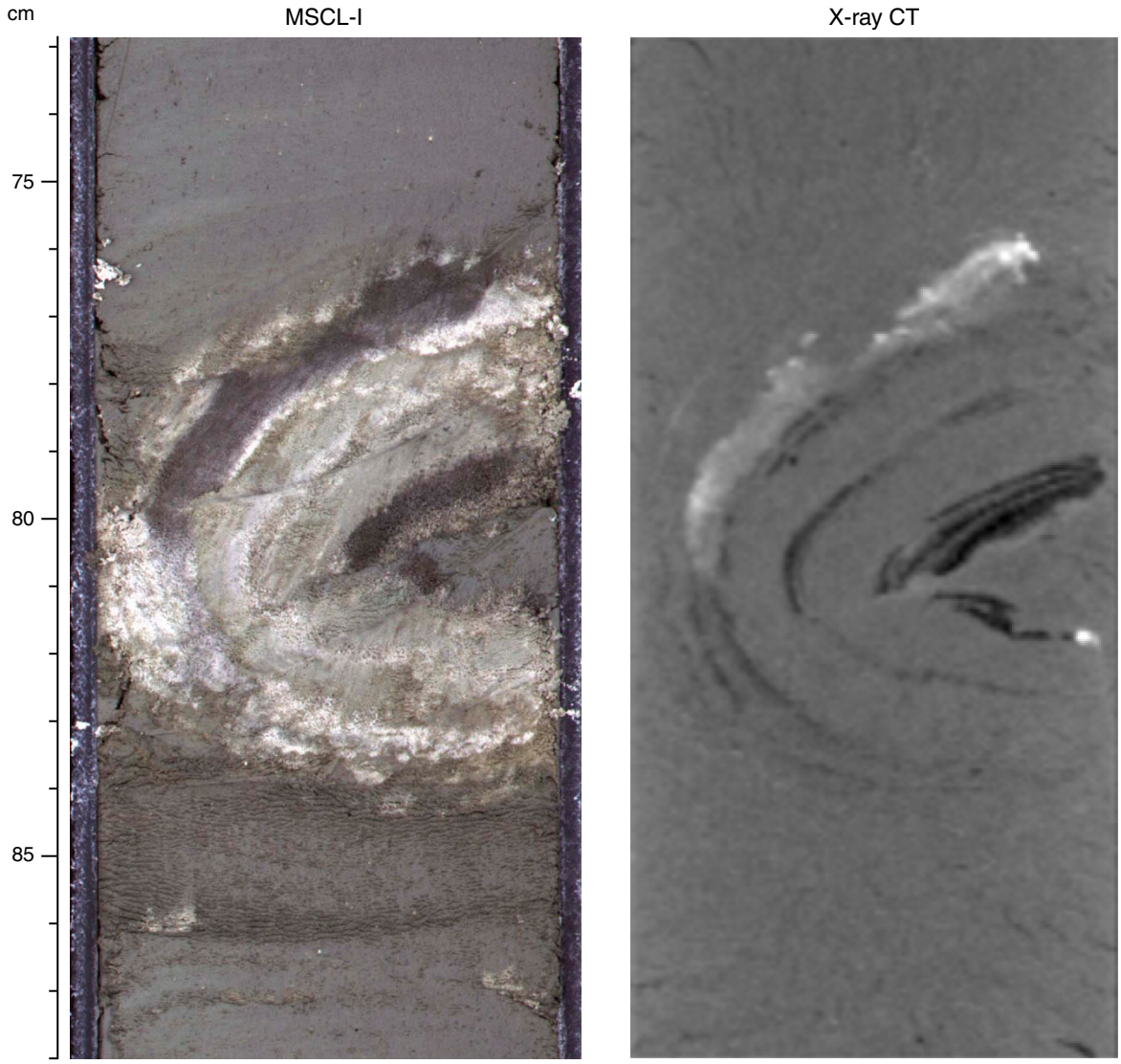

Figure F17. Lower hemisphere equal area projection of poles to folded bedding plane (circles) and fold axis (green triangle) of the slump fold (Fig. F16), Hole C0018A.

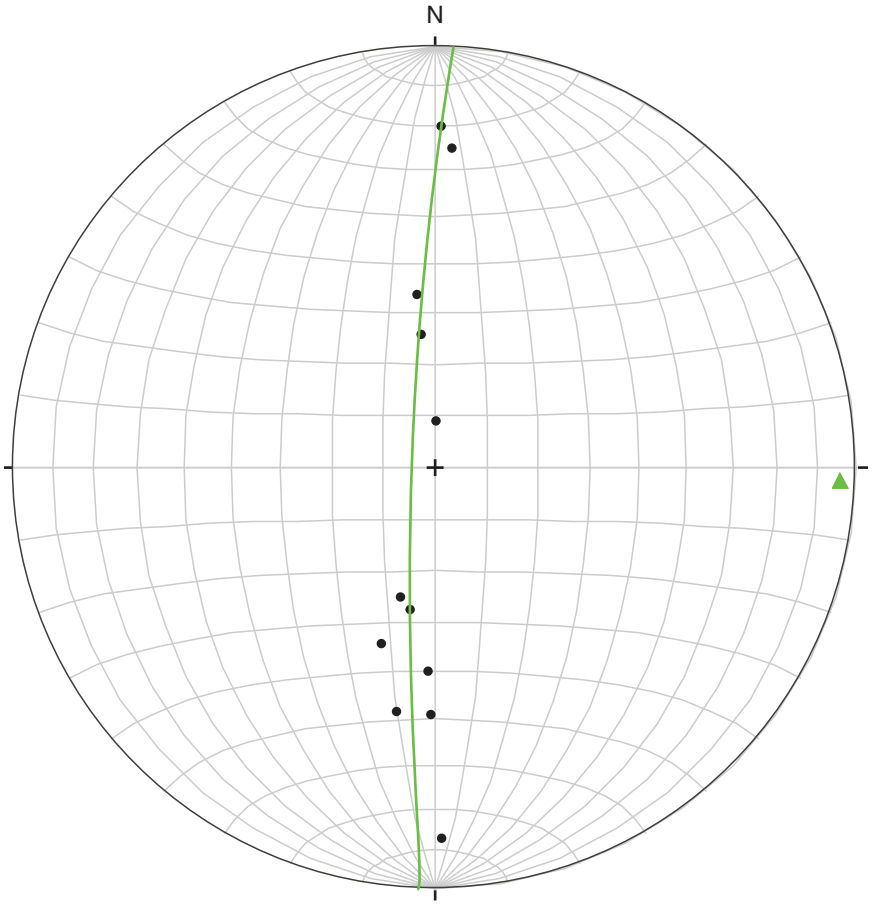

Figure F18. Appearance of shear zone (interval 333-C0018A-17H-6, 53–74 cm). Red triangles = location of shear zones. MSCL-I = photo image logger, CT = computed tomography.

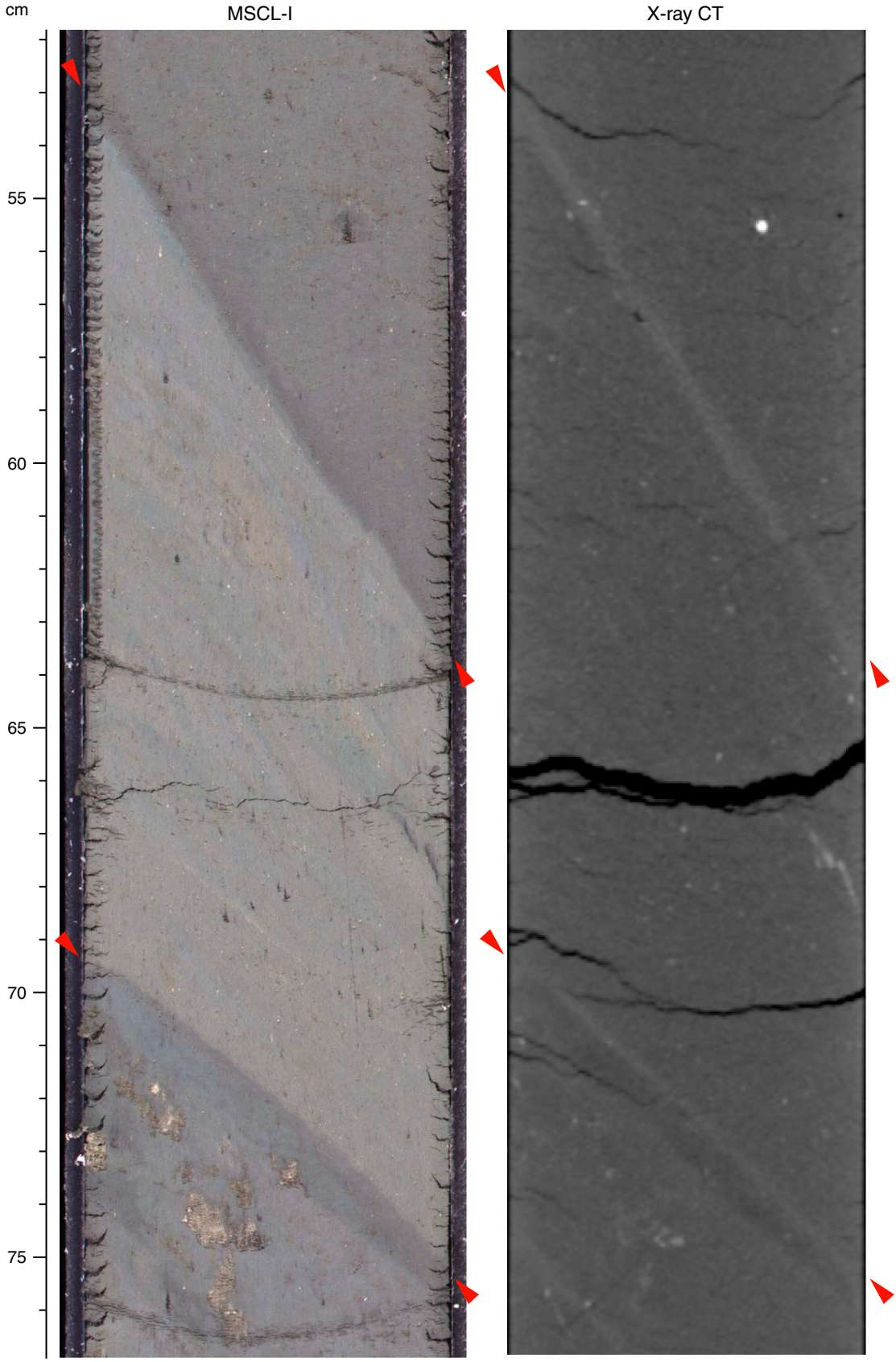

Figure F19. Appearance of flow structure (interval 333-C0018A-22H-6, 10–30 cm). MSCL-I = photo image logger, CT = computed tomography.

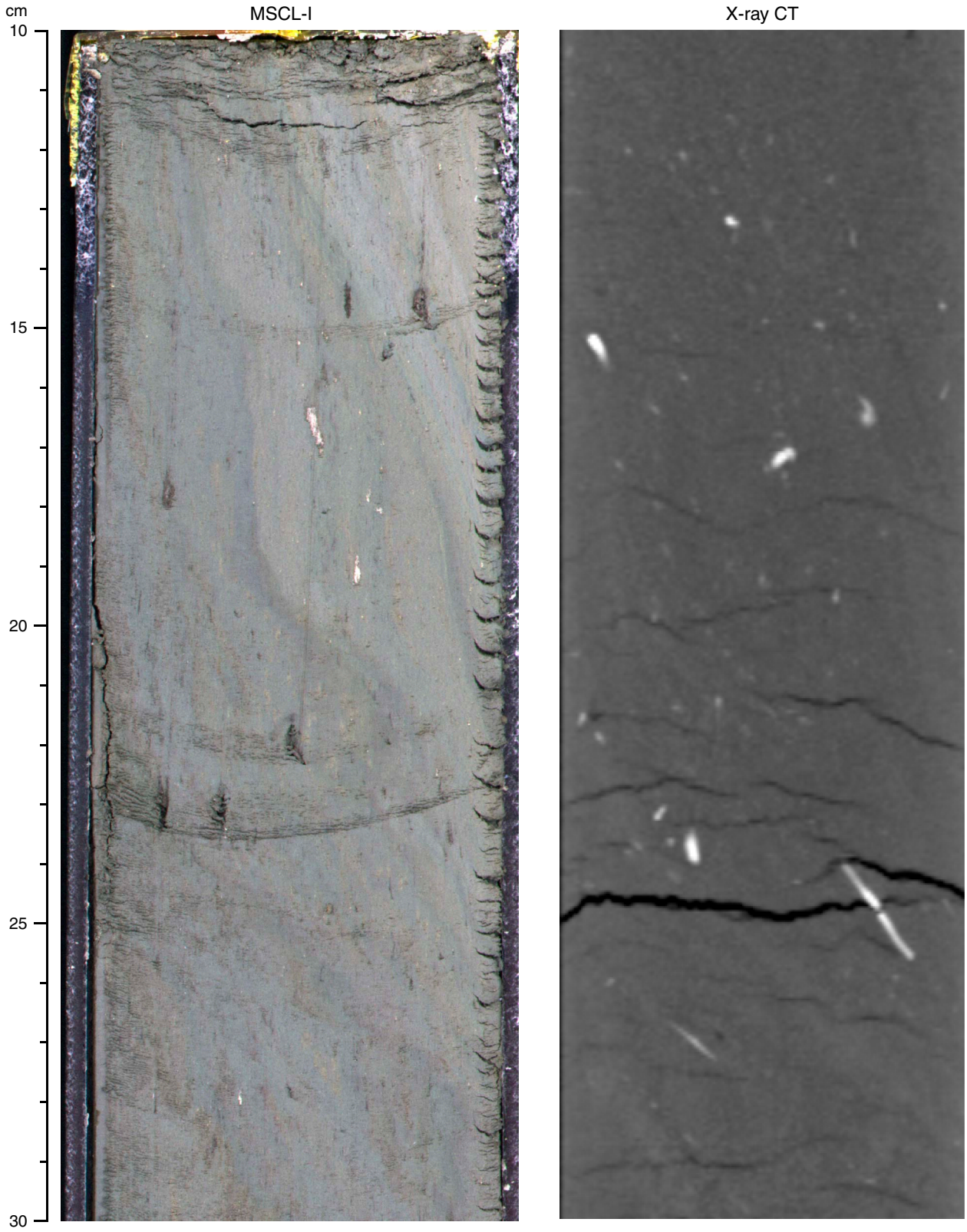

Figure F20. Fault with slickenlines and steps (interval 333-C0018A-16H-11, 36–42 cm). Red triangles = location of fault, white line = orientation of slickenline.

Figure F21. Appearance of web structures (interval 333-C0018A-17H-8, 30–40 cm).

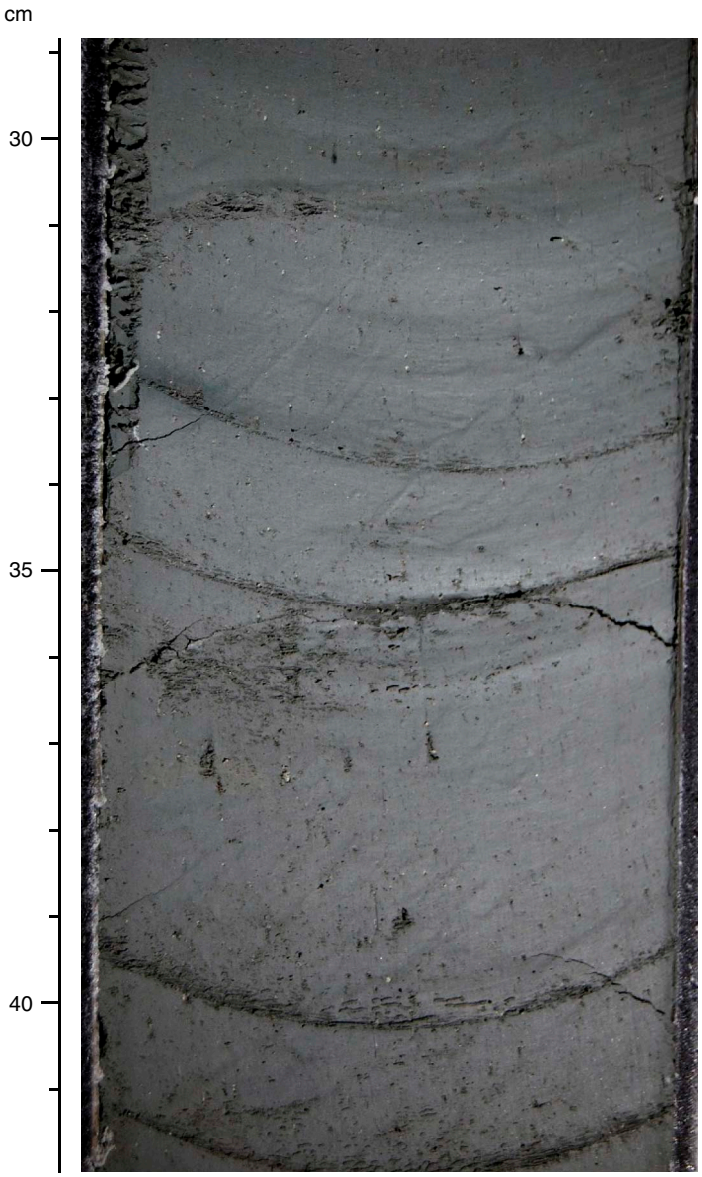

Figure F22. Lower hemisphere equal area projection of poles to bedding and fissility, Hole C0018A Subunit IB.

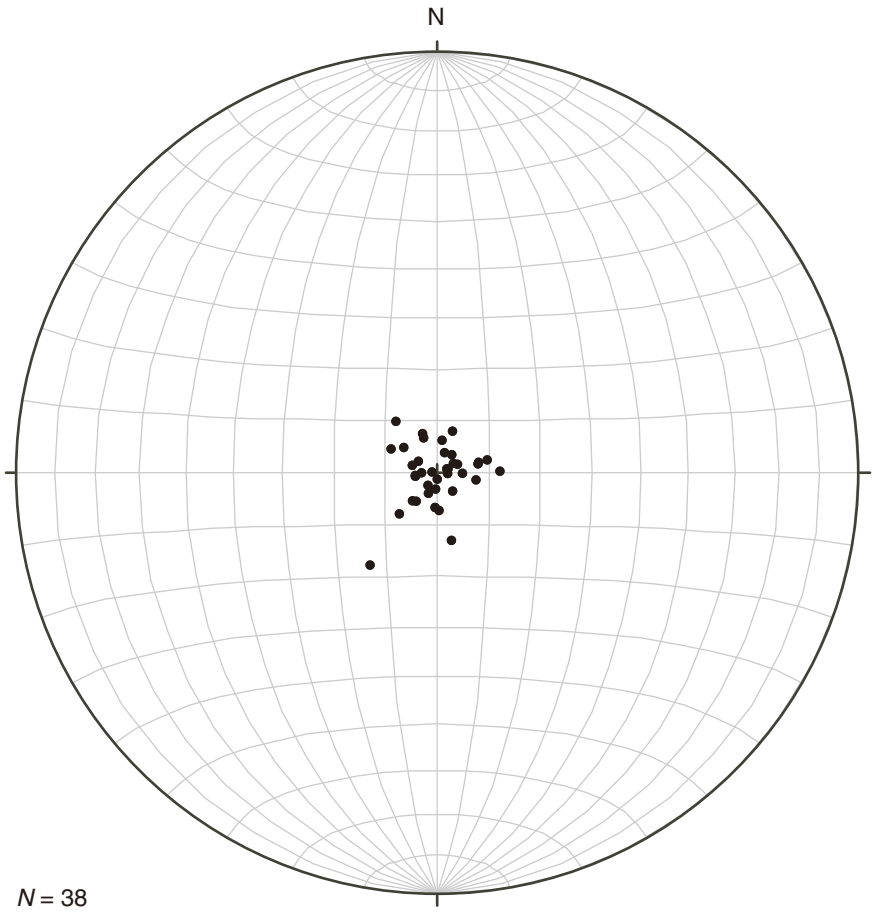

Figure F23. Appearance of fissility in siltstone (interval 333-C0018A-31X-6, 53–55 cm). White dotted line = orientation of fissility.

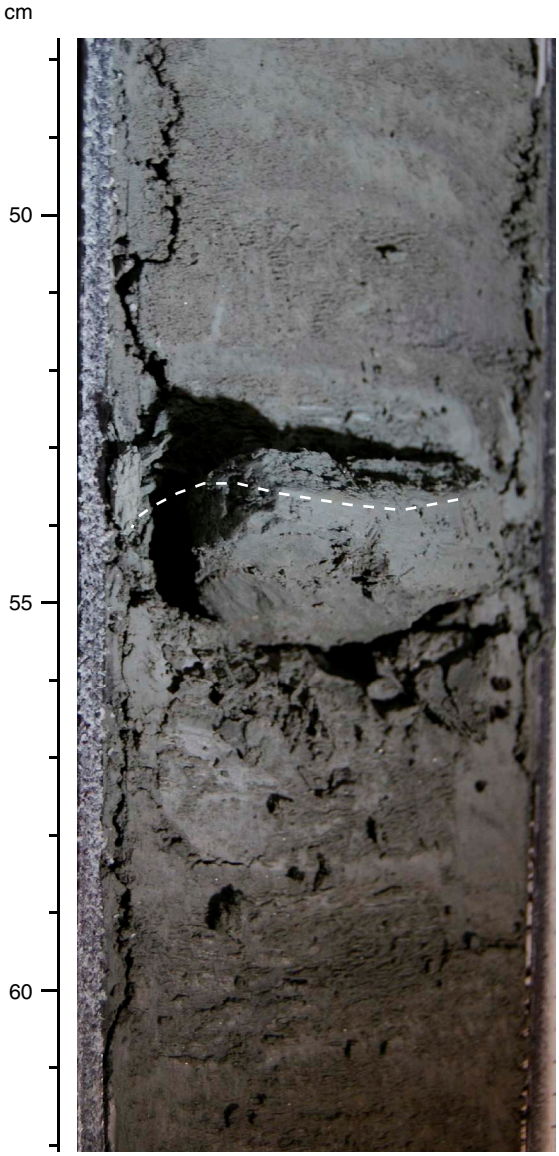

Figure F24. Age-depth plot for Hole C0018A showing nannofossil datums, paleomagnetic events, volcanic marker events, and estimated bulk sedimentation rates (in cm/k.y.) between individual nannofossil datums.

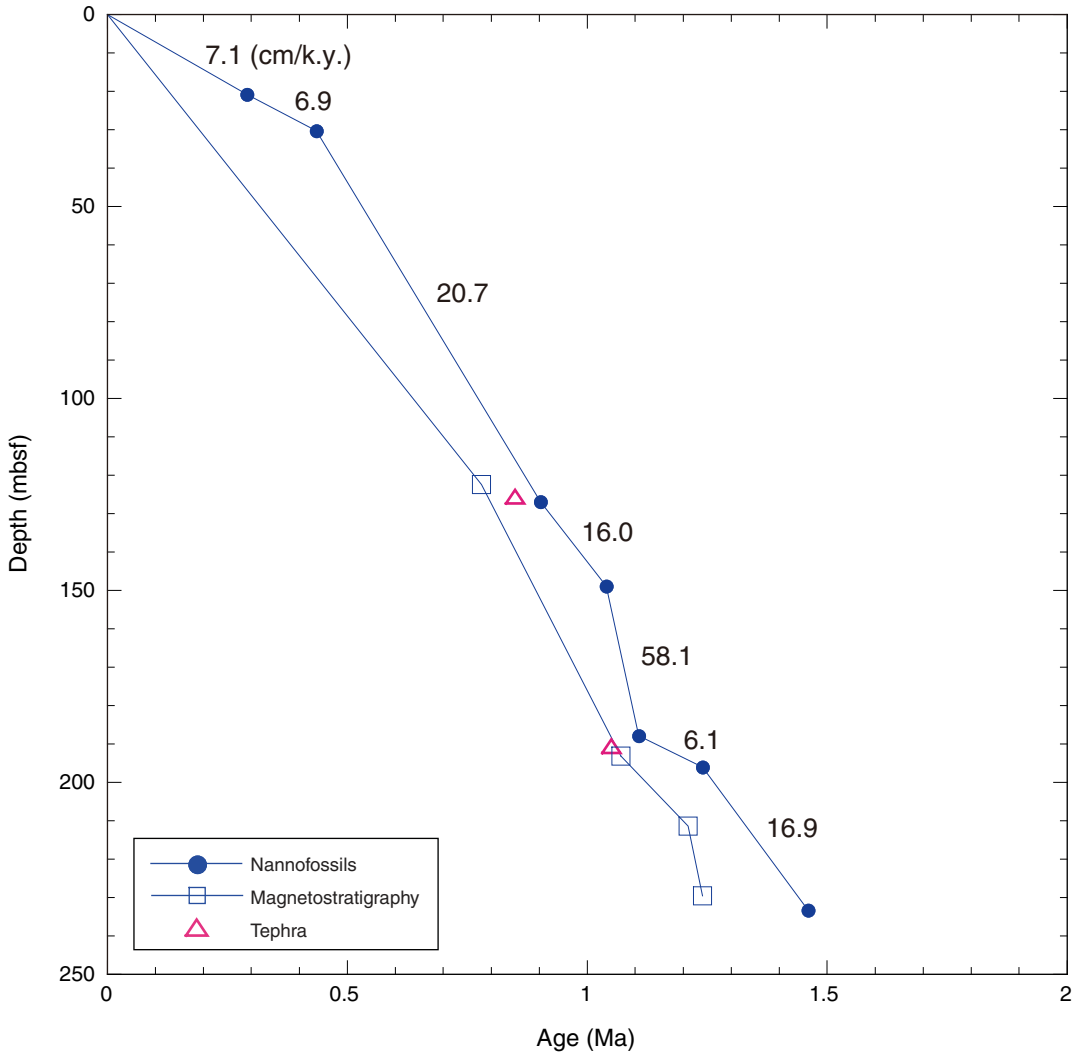

Figure F25. Magnetic susceptibility and remanent magnetization intensity, declination, and inclination of discrete samples as a function of depth, Hole C0018A. Green = natural remanent magnetization (NRM), Blue = 30 mT AF demagnetization. NRM inclinations are biased toward high positive inclinations, suggesting drilling-induced magnetization. AF demagnetization to 30 mT can effectively remove this drilling-induced magnetization, as indicated by changes in its inclination and intensity. MSCL = multisensor core logger. MTD = mass transport deposit.

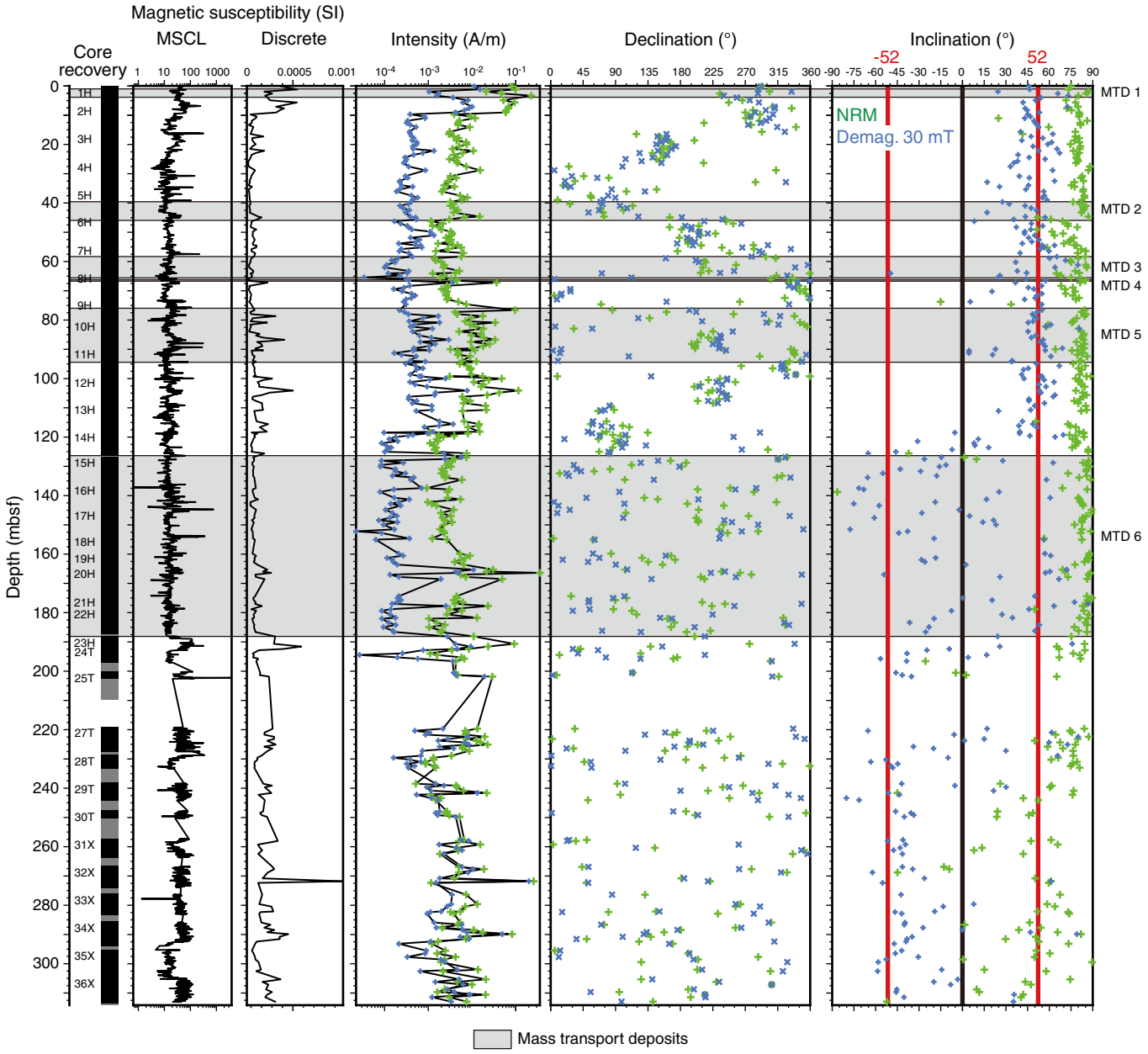

Figure F26. Zijderveld plots and stereonet magnetization directions (equal area lower hemisphere stereographic plot) showing results of AF demagnetization for sediments from (**A**) Sample 333-C0018A-29T-2, 12.0 cm (239.655 mbsf), (**B**) Sample 333-C0018A-33X-7, 84.0 cm (282.125 mbsf), and (**C**) Sample 333-C0018A-8H-7, 80.0 cm (68.418 mbsf). Black and white circles = projection of magnetization vector endpoint on horizontal and vertical planes, respectively, which is then plotted on a equal area lower hemisphere projection. Plots in the center bottom show magnetization of the samples that decrease as demagnetized. NRM = natural remanent magnetization.

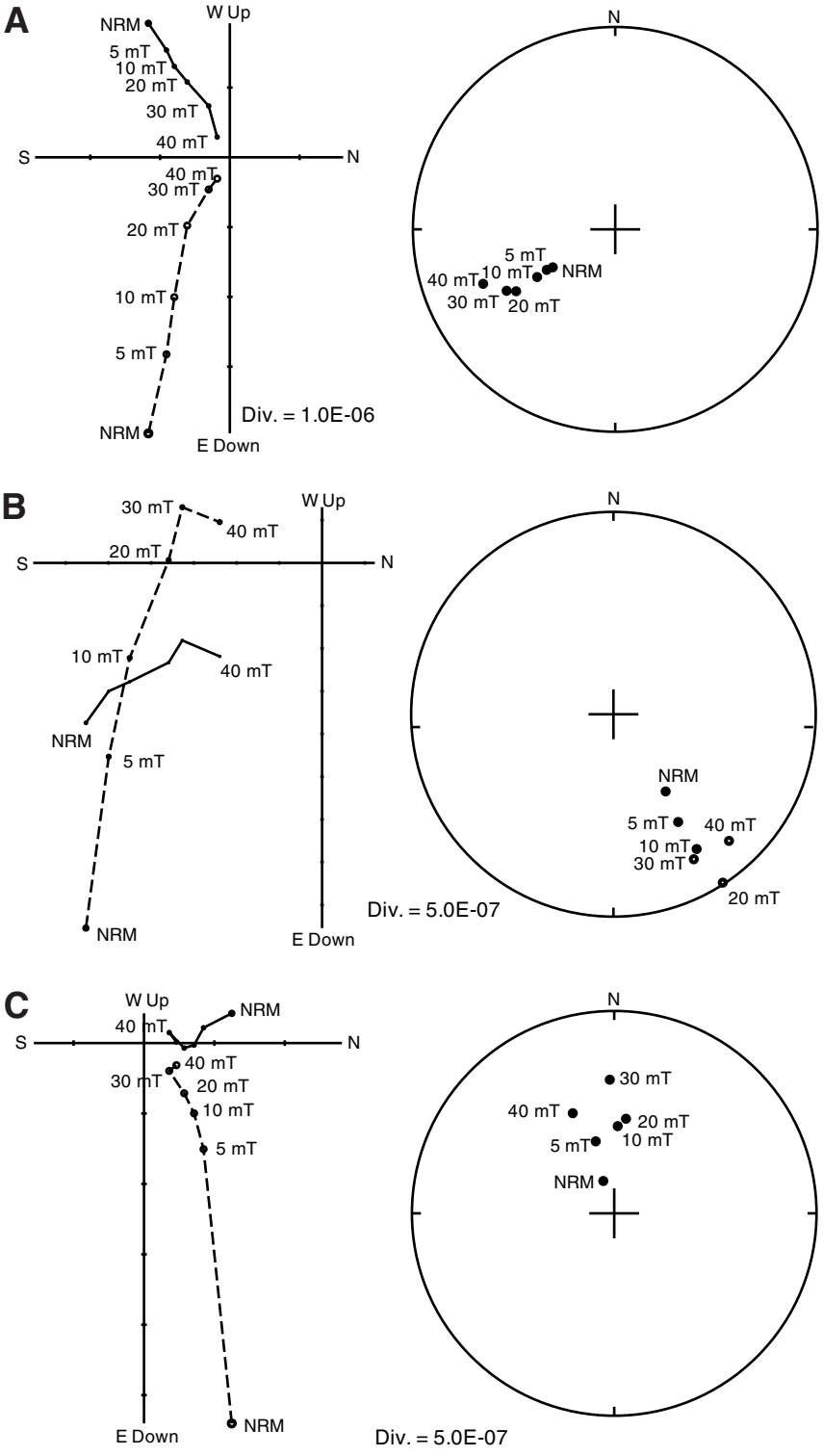

Figure F27. Histogram of inclinations after 30 mT demagnetization on discrete samples from Hole C0018A excluding MTD 6 horizons.

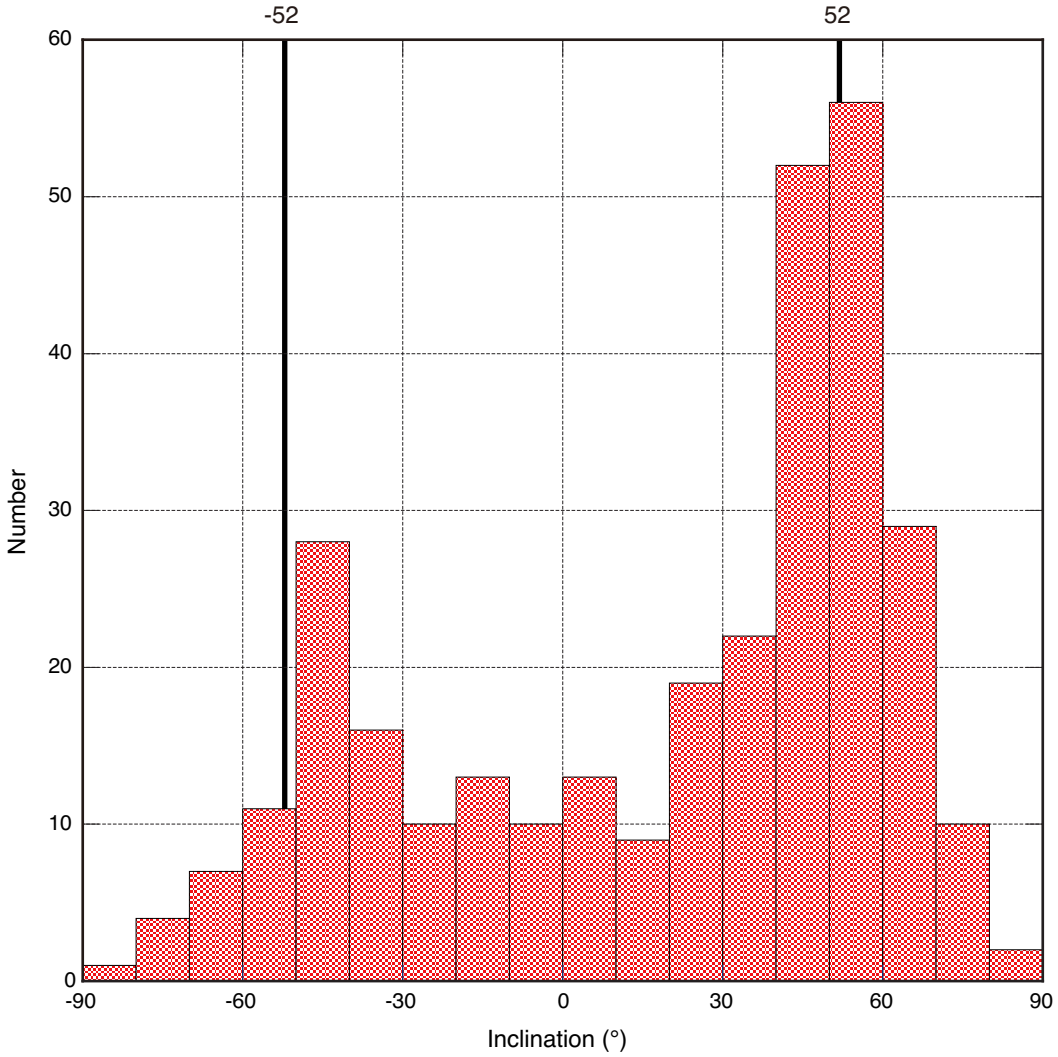

Figure F28. Variation of declinations for Cores 333-C0018A-1H through 13H referring the uppermost samples in each core. No systematic twisting induced by drilling is apparent.

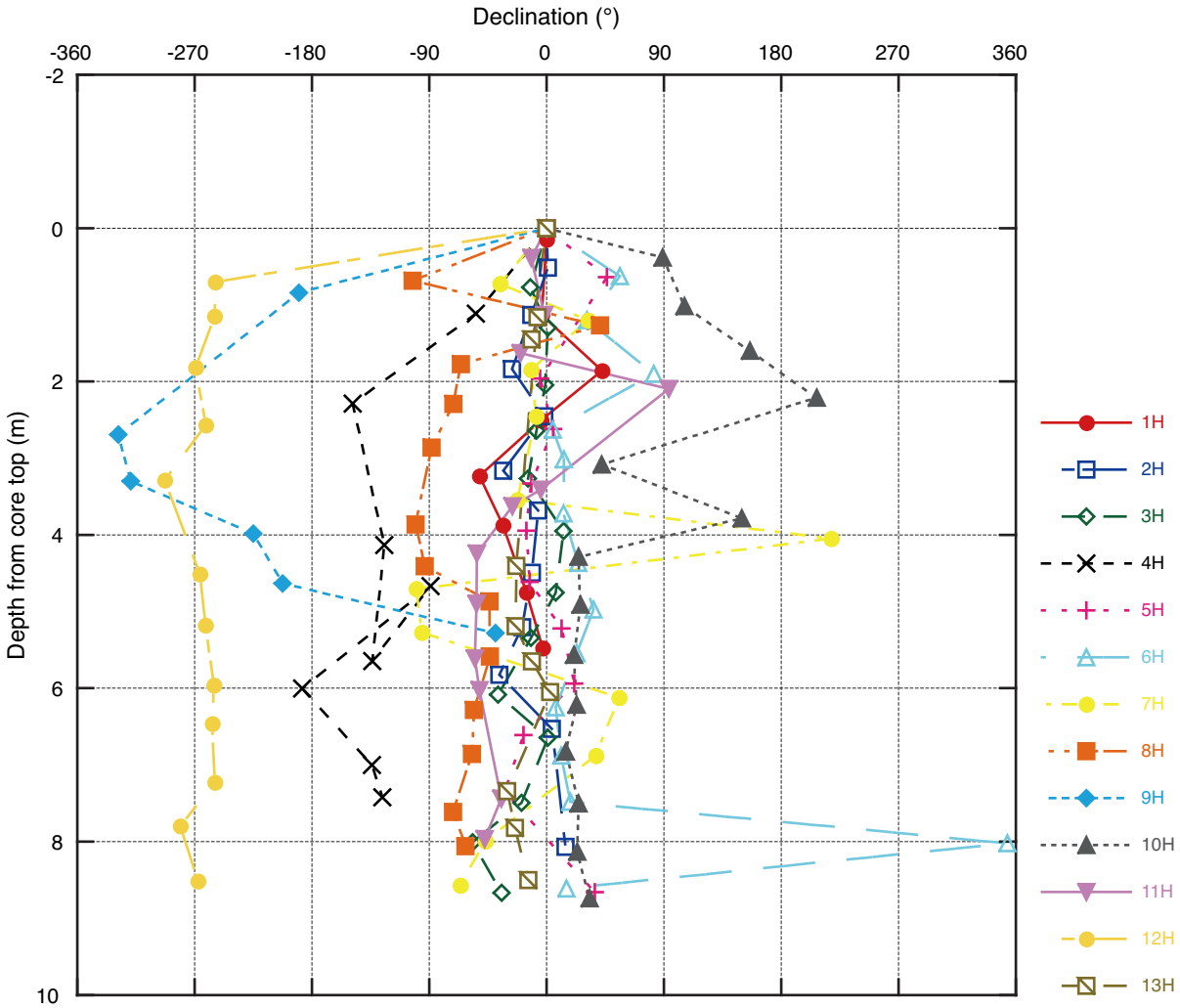

Figure F29. Downhole variation in stable magnetic inclination, inferred polarity, and tephra chronological age for sediments, Site C0018. Black = normal polarity, white = reversed polarity. No interpretation provided for shaded areas. MTD = mass transport deposit.

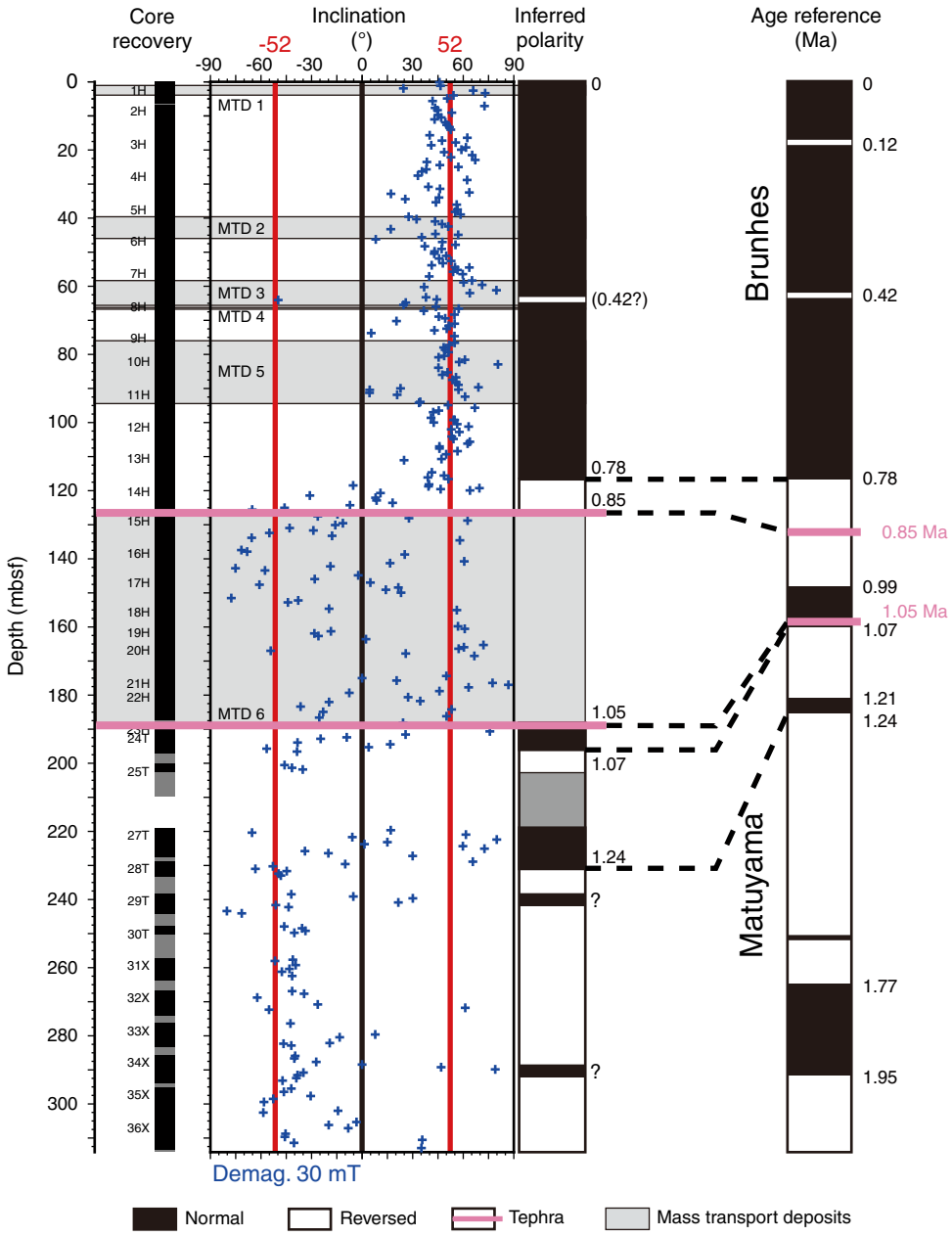

Figure F30. Site C0018 MSCL-W gamma ray attenuation (GRA) density, magnetic susceptibility, electrical resistivity, and natural gamma radiation. Gray shading = mass transport deposit (MTD) 6. CMS = corrected volume magnetic susceptibility, cps = counts per second.

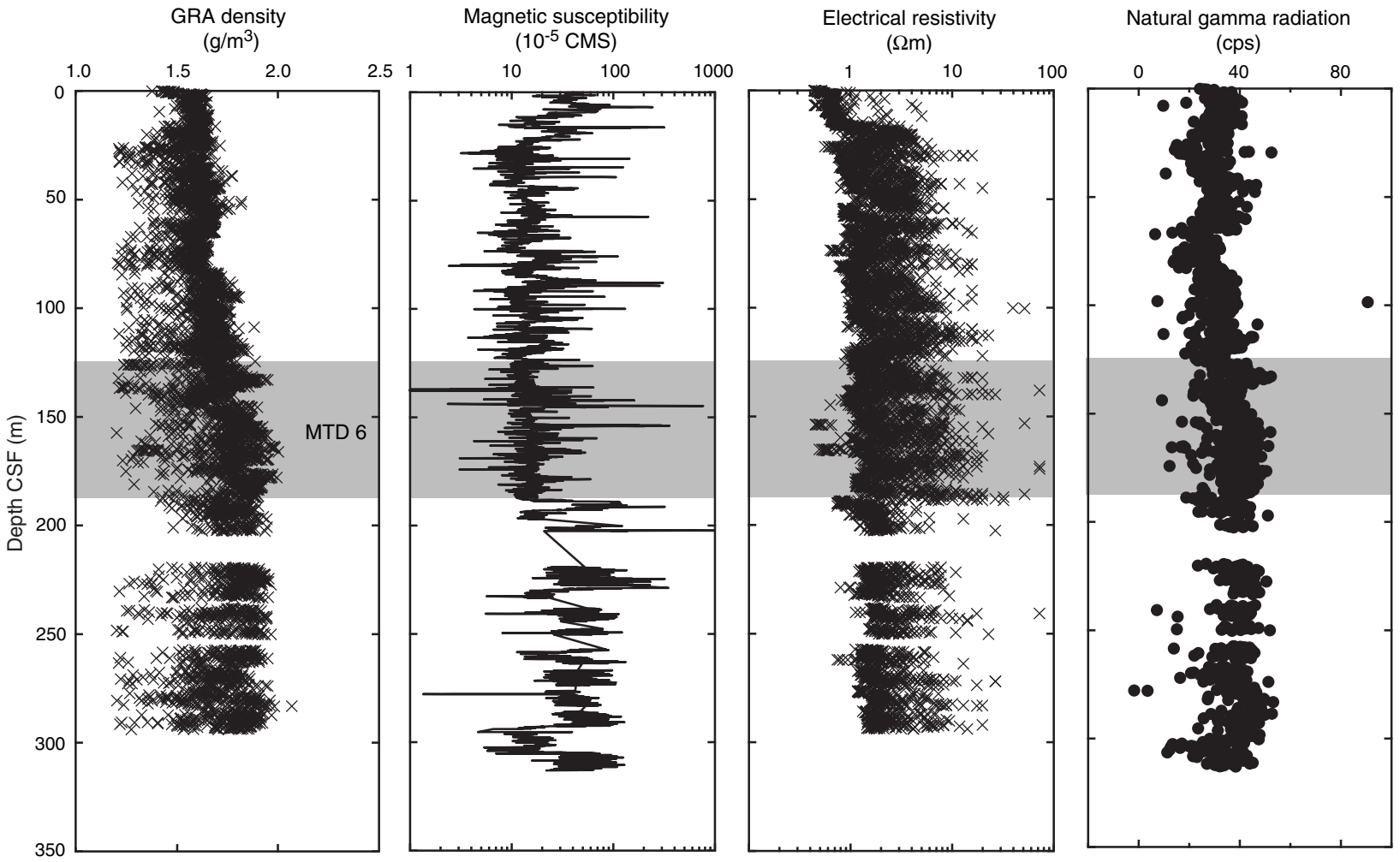

Figure F31. Site C0018 bulk density, porosity, and grain density from discrete MAD samples. Blue = mud and silt samples, red = observed sand or ash samples, gray shading = mass transport deposit (MTD) 6.

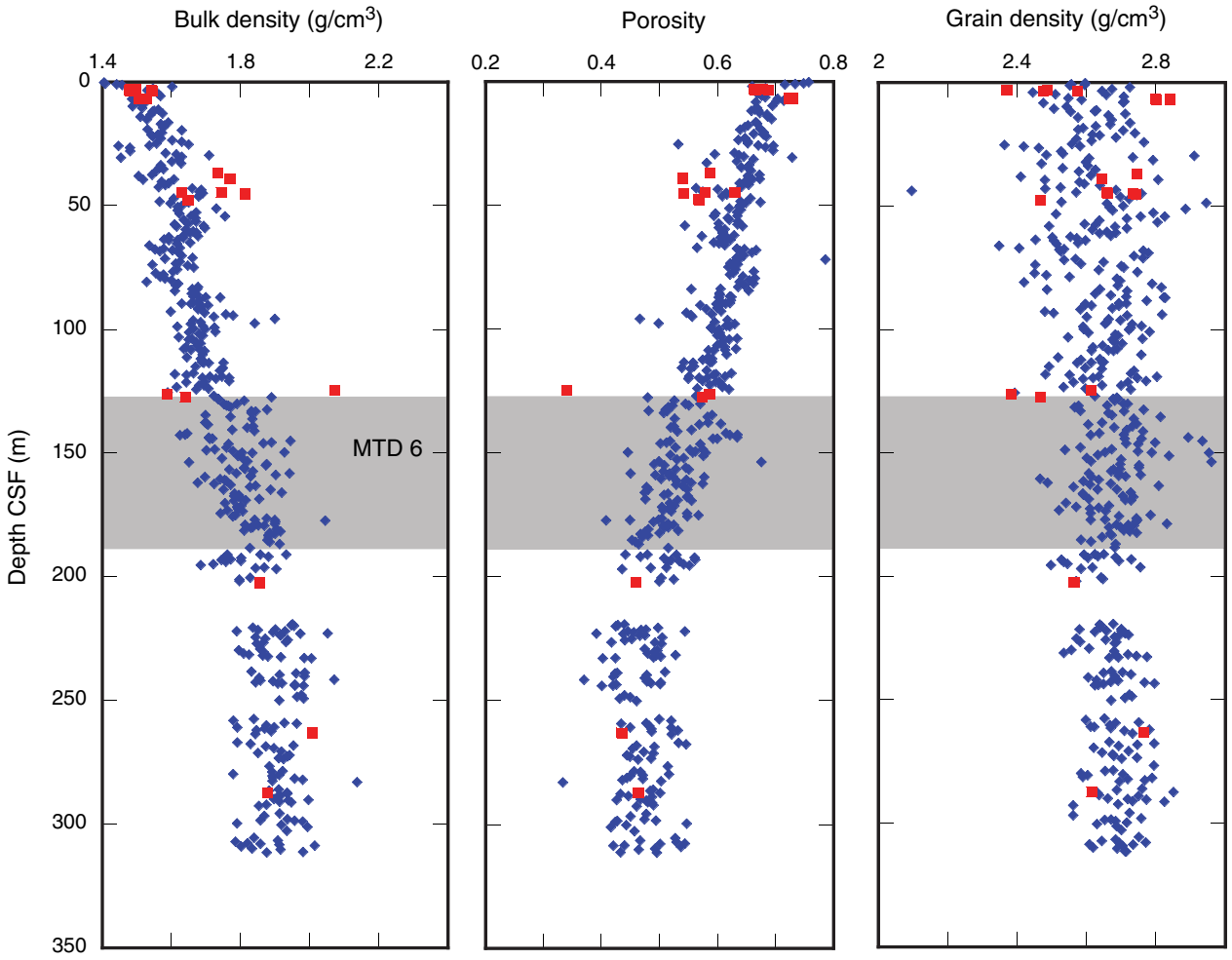

Figure F32. Strength measured with a pocket penetrometer and a vane shear device, Hole C00018A. Gray shading = mass transport deposit (MTD) 6.

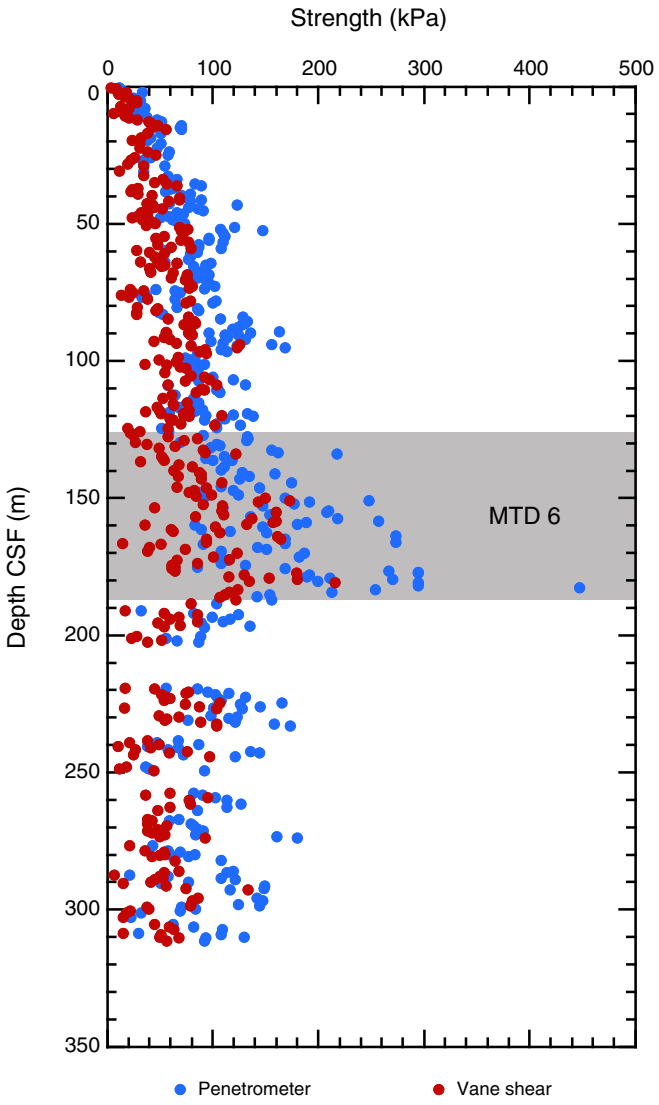

Figure F33. A. Measured resistivity (black) plotted with multisensor core logger (MSCL) resistivity (red), Site C0018A. **B.** Measured resistivity. Gray shading = mass transport deposit (MTD) 6. **C.** Plot of measured resistivity over the MTD 6 interval.

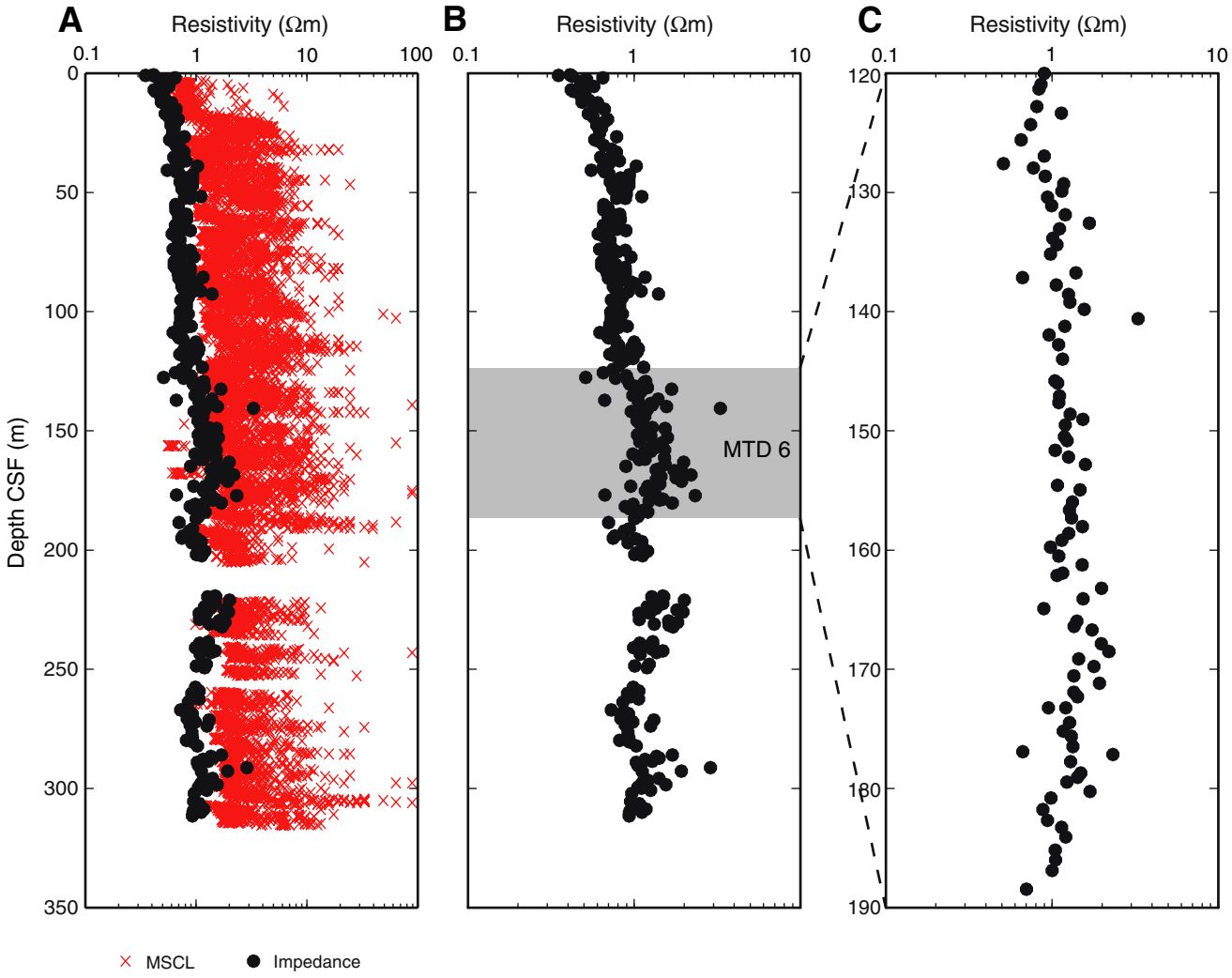

Figure F34. Thermal conductivity as function of depth, Hole C0018A. Gray shading = mass transport deposit (MTD) 6.

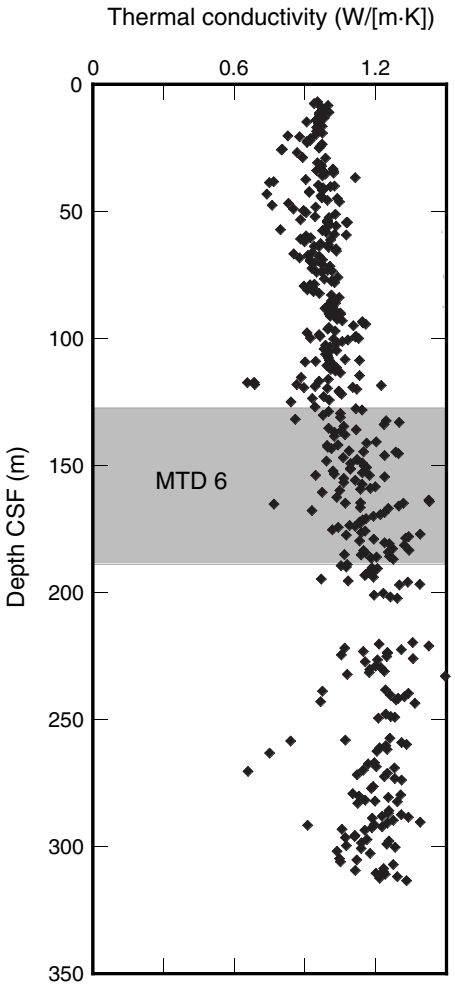

Figure F35. Temperatures obtained by APCT-3 measurements during coring, Hole C0018A. Blue circles = poor quality data, open squares = data considered reliable.

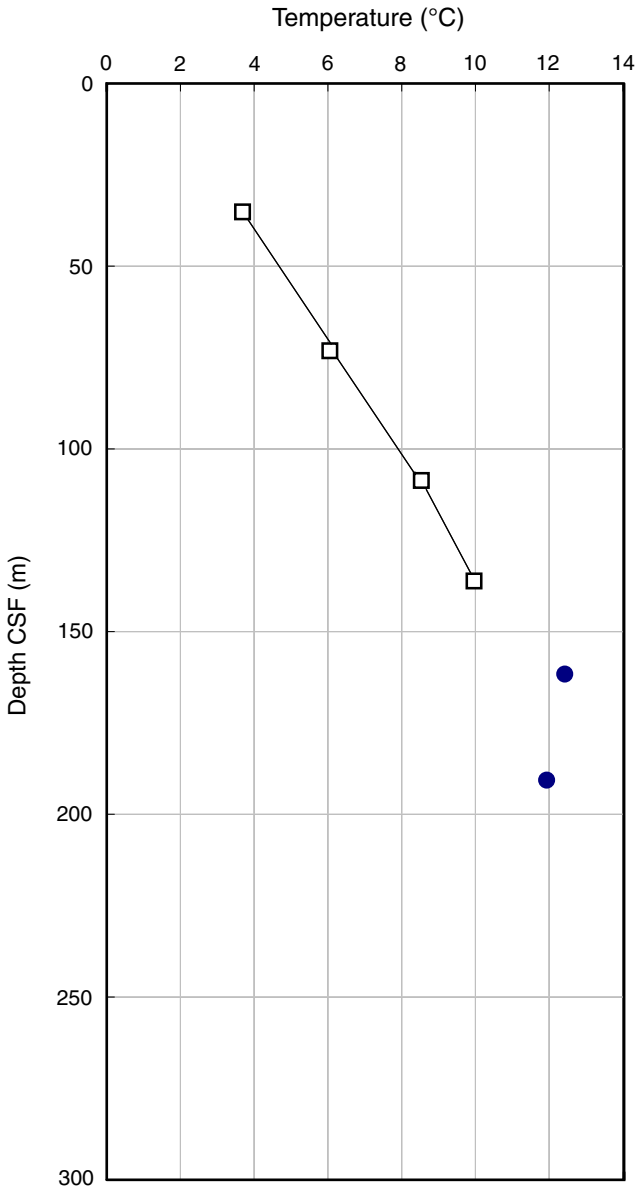

Figure F36. Temperatures projected to the bottom of Hole C0018A, using estimated heat flow (q = 62 mW/m^2) and measured thermal conductivity.

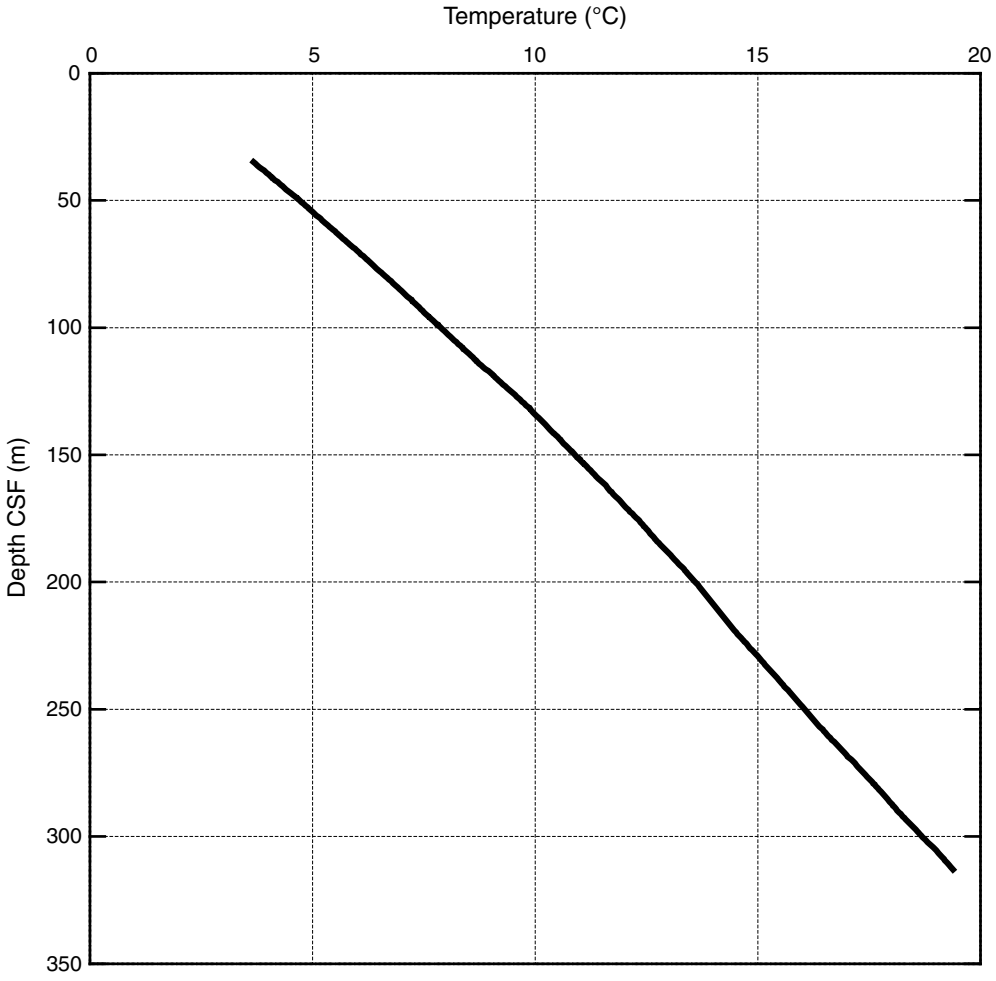

Figure F37. A. Volume of interstitial water recovered, Hole C0018A. **B.** Dissolved sulfate profile, used to estimate the (**C**) percent contamination values (Table T11).

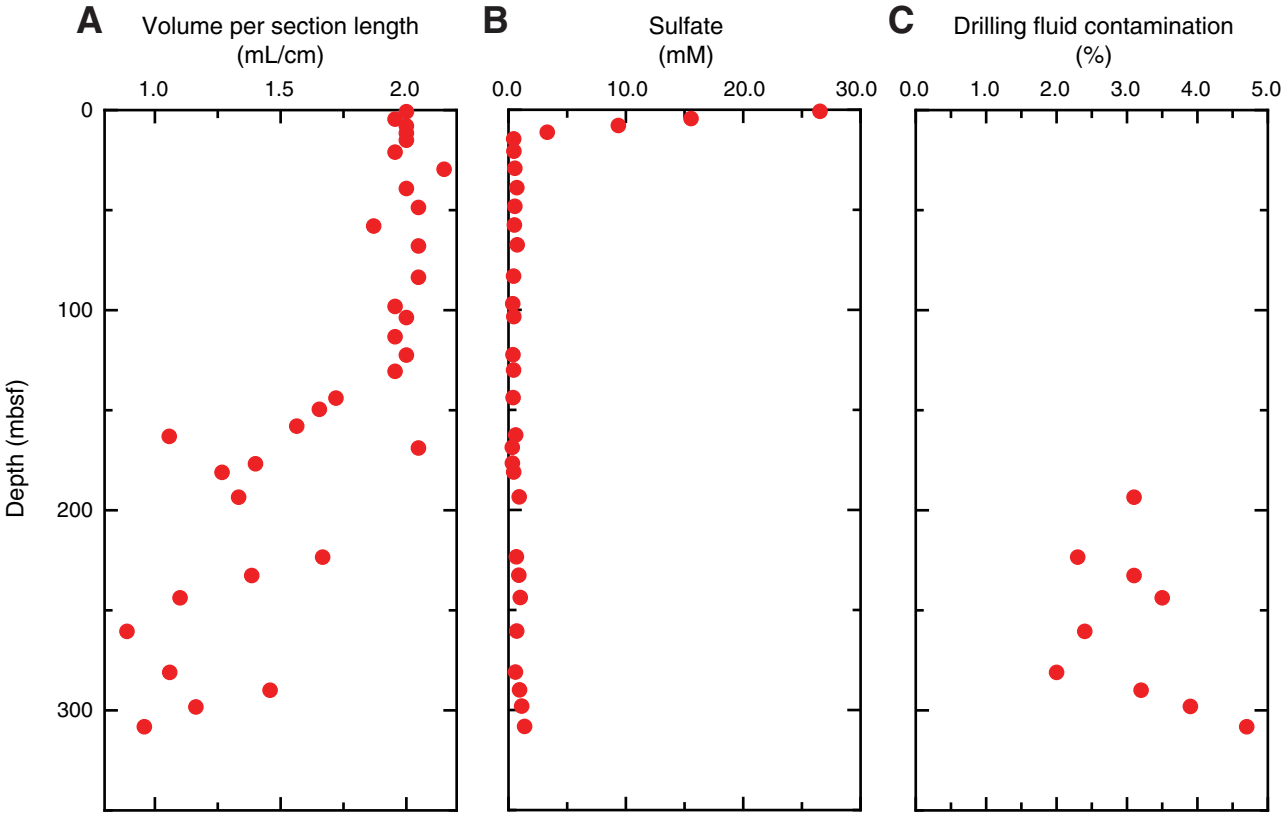

Figure F38. Interstitial water constituents (salinity, chlorinity, bromide, pH, alkalinity, sodium, ammonium, phosphate, Br/Cl, and boron), Hole C0018A (Table T12).

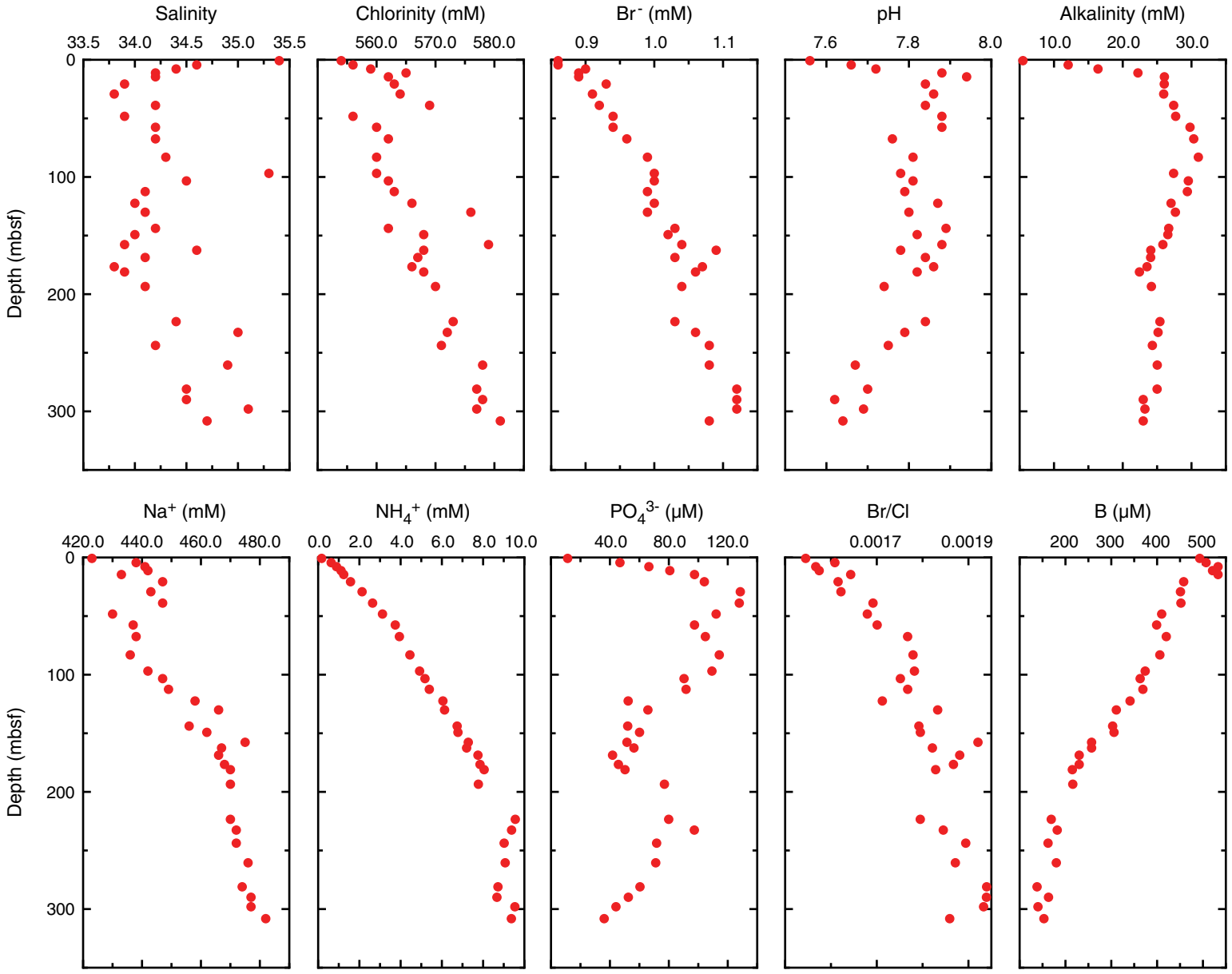

Figure F39. Interstitial water constituents (potassium, magnesium, calcium, silica, iron, lithium, strontium, barium, and manganese), Hole C0018A (Table T12).

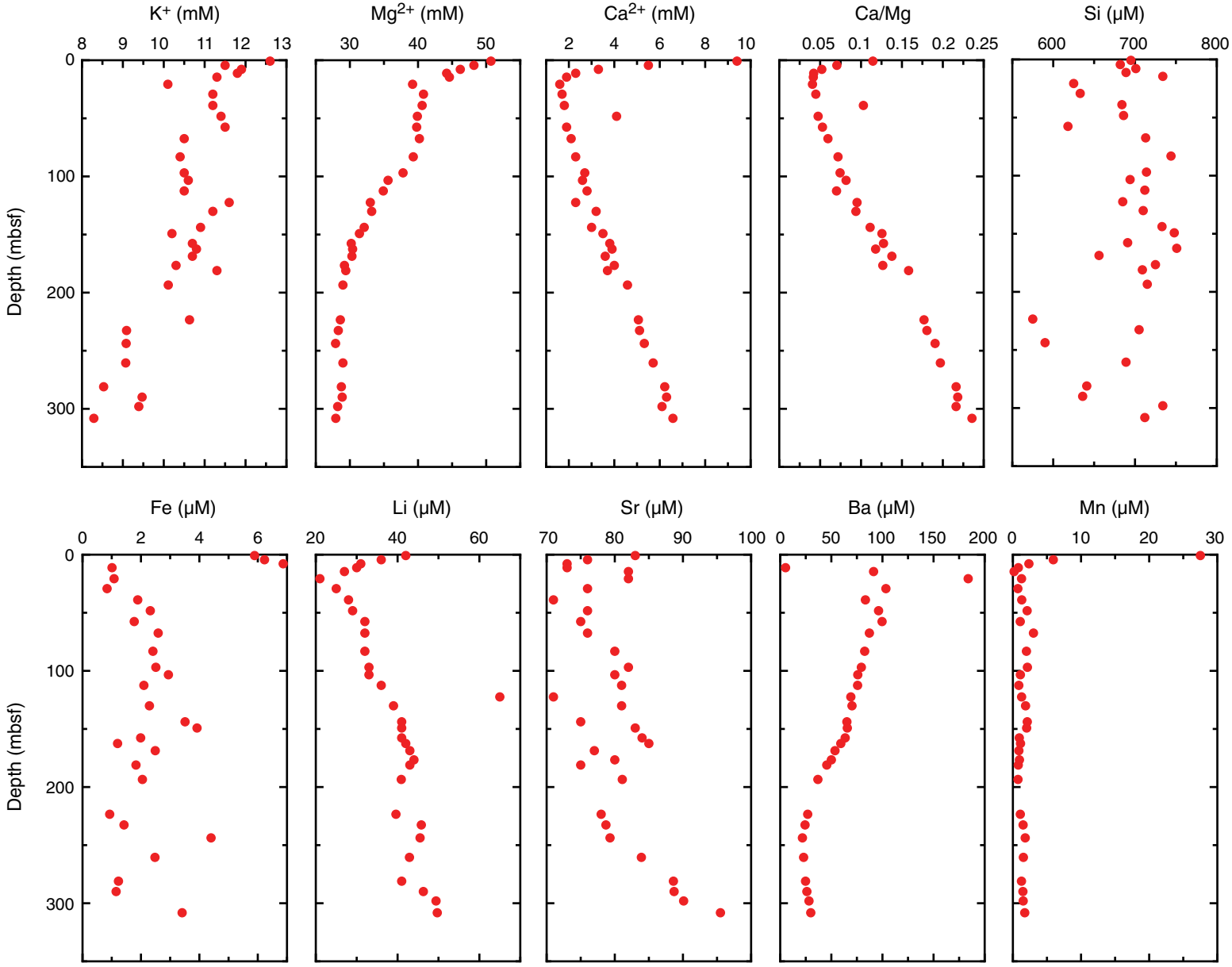

Figure F40. Interstitial water trace element constituents (rubidium, cesium, vanadium, copper, zinc, molybdenum, lead, and uranium), Hole C0018A (Table T11).

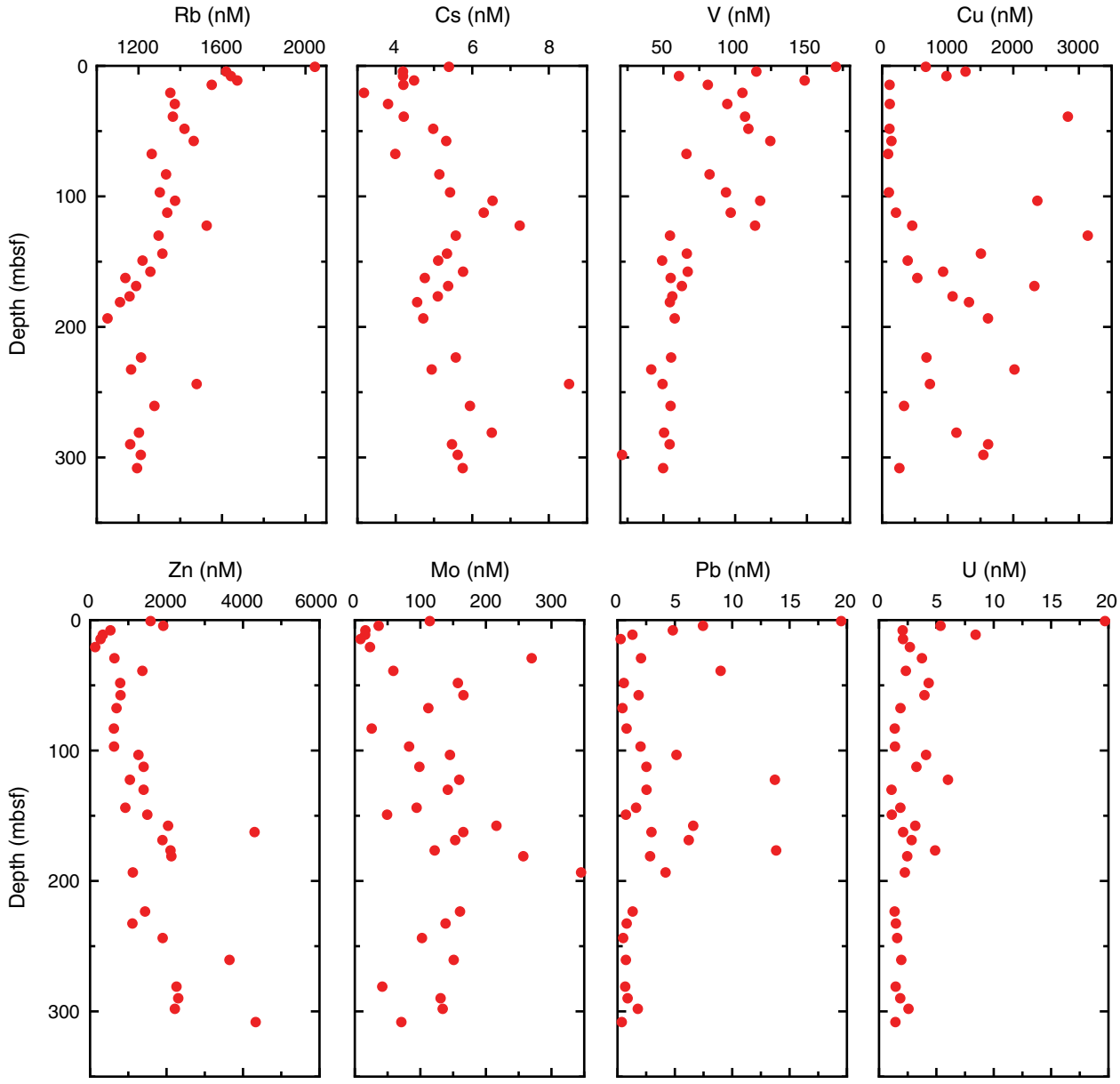

Figure F41. Headspace methane concentration, ethane concentration, and the ratios of methane to ethane (C1/C2), Hole C0018A. Methane and ethane are set at 0.0 when below detection. C1/C2 is set at 100,000 when ethane concentration is below detection. ppmv = parts per million by volume.

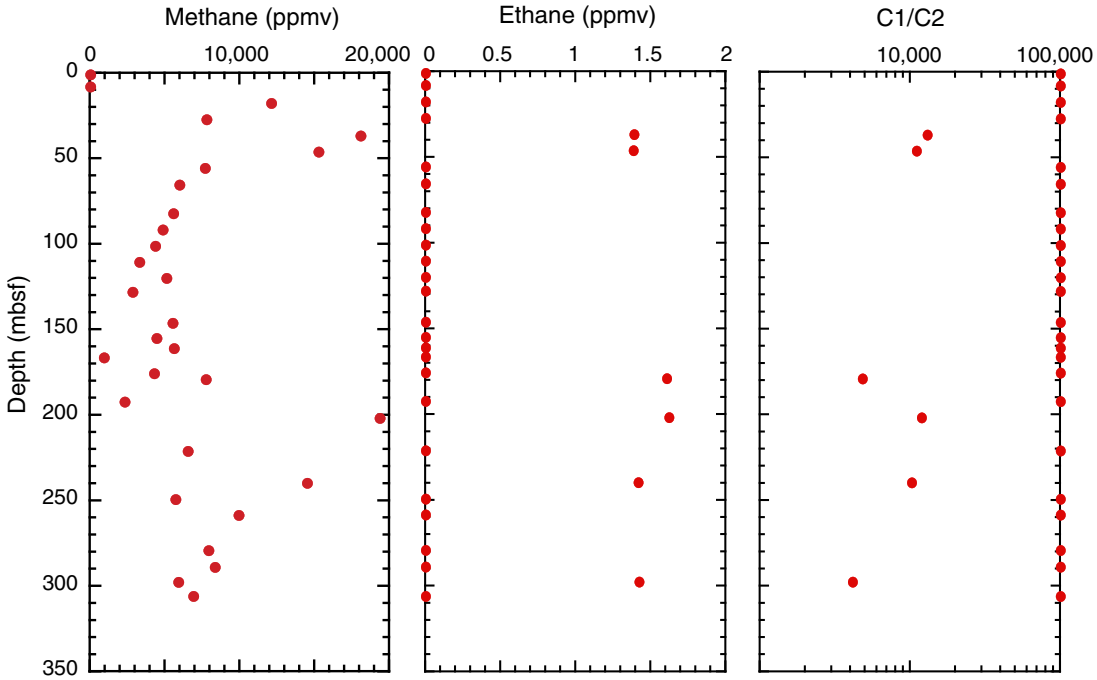

Figure F42. Calcium carbonate ($CaCO_3$), total organic carbon (TOC), total nitrogen (TN), the atomic ratios of TOC to TN (TOC/TN_{at}), and total sulfur (TS) contents in bulk sediment, Hole C0018A.

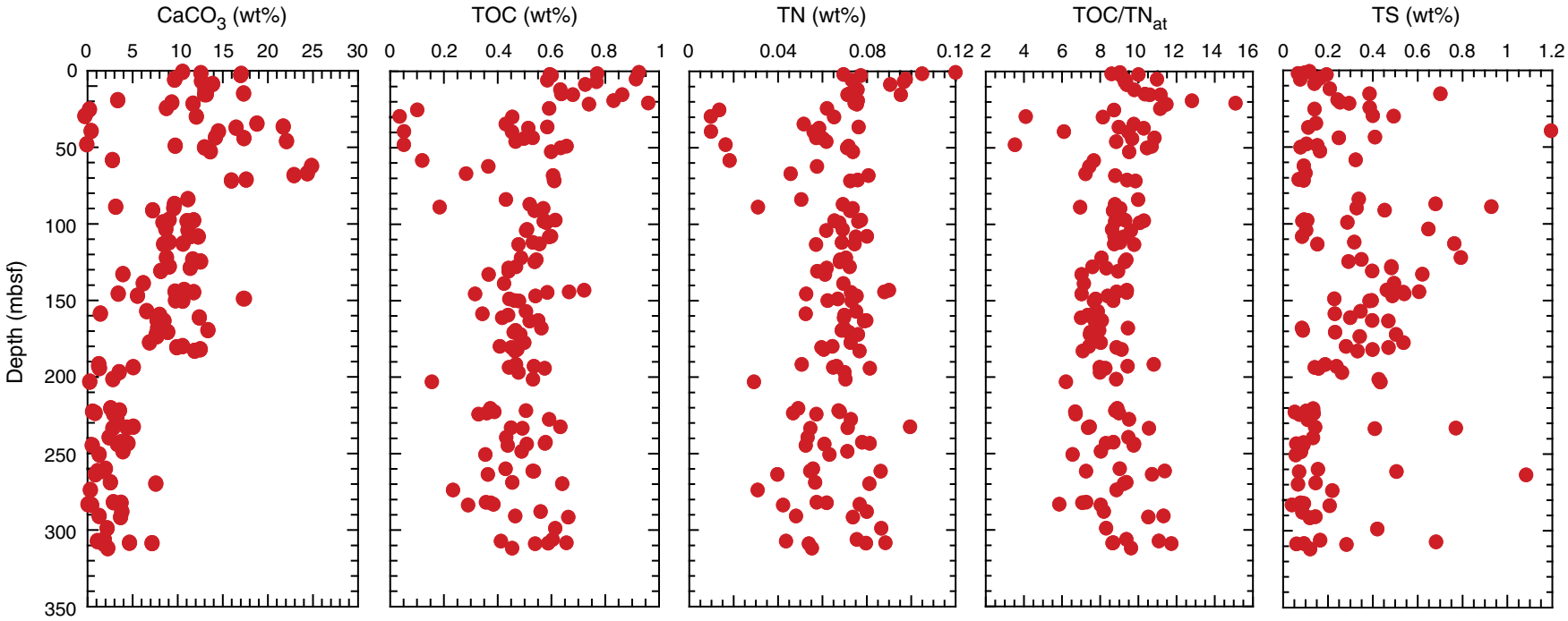

Figure F43. Rock-Eval pyrolysis parameters: S1, S2, T_{max}, hydrogen index (HI), and production index (PI), Hole C0018A. HC = hydrocarbon, TOC = total organic carbon.

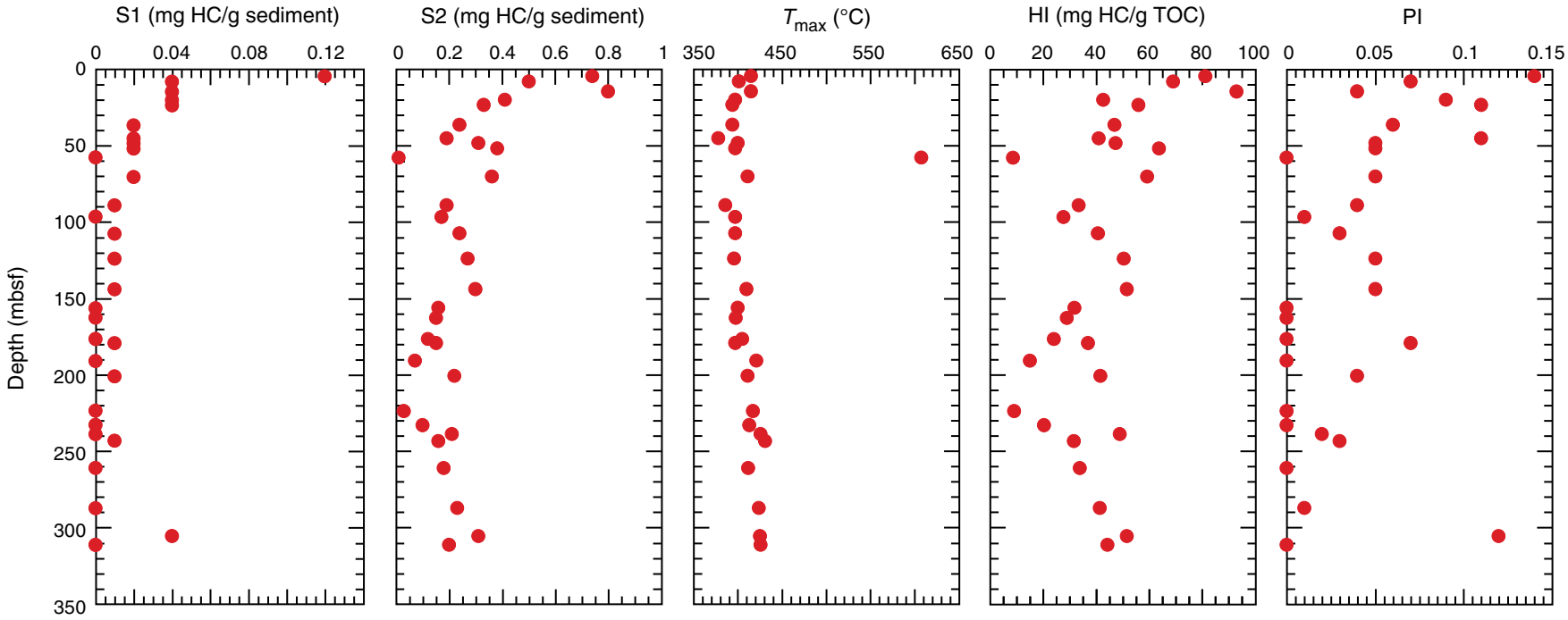

Table T1. Coring summary, Site C0018.

Hole C0018A
Latitude: 33°09.4195′N
Longitude: 136°40.8888′E
Seafloor (DRF, m): 3112.85
Total depth (DRF, m): 3427
Total penetration (DSF, m): 314.15
Total length of cored section (m): 314.15
Total core recovered (m): 271.44
Core recovery (%): 86.4
Total number of cores: 36

Core	Depth CSF (m) Top	Depth CSF (m) Bottom	Advanced (m)	Core recovered (m)	Recovery (%)
333-C0018A-					
1H	0.00	6.65	6.65	6.65	99.8
2H	6.65	16.15	9.50	10.00	105.4
3H	16.15	25.65	9.50	9.91	104.4
4H	25.65	35.15	9.50	10.42	109.8
5H	35.15	44.65	9.50	9.74	103.3
6H	44.65	54.15	9.50	10.56	109.4
7H	54.15	63.65	9.50	10.48	109.7
8H	63.65	73.15	9.50	10.40	111.4
9H	73.15	80.15	7.00	7.38	105.5
10H	80.15	89.65	9.50	10.75	113.2
11H	89.65	99.15	9.50	11.50	116.1
12H	99.15	108.65	9.50	9.80	106.7
13H	108.65	118.15	9.50	11.07	119.6
14H	118.15	126.65	8.50	8.31	97.9
15H	126.65	136.15	9.50	10.66	98.9
16H	136.15	144.65	8.50	8.50	100.5
17H	144.65	153.65	9.00	9.12	93.6
18H	153.65	159.65	6.00	6.10	67.5
19H	159.65	164.65	5.00	5.65	101.6
20H	164.65	174.15	9.50	9.90	57.3
21H	174.15	178.45	4.30	4.33	92.3
22H	178.45	187.95	9.50	8.93	54.9
23H	187.95	190.65	2.70	2.90	108.9
24T	190.65	200.15	9.50	6.55	68.7
25T	200.15	209.65	9.50	2.50	26.1
26T	209.65	219.15	9.50	0.00	0.0
27T	219.15	228.65	9.50	8.37	90.7
28T	228.65	238.15	9.50	4.86	50.1
29T	238.15	247.65	9.50	6.05	65.5
30T	247.65	257.15	9.50	2.80	29.3
31X	257.15	266.65	9.50	6.80	70.8
32X	266.65	276.15	9.50	7.80	78.9
33X	276.15	285.65	9.50	7.83	76.3
34X	285.65	295.15	9.50	8.47	88.7
35X	295.15	304.65	9.50	10.87	114.9
36X	304.65	314.15	9.50	8.67	94.5

DRF = drilling depth below rig floor, DSF = drilling depth below seafloor, CSF = core depth below seafloor. H = hydraulic piston coring system, T = extended punch coring system, X = extended shoe coring system.

Table T2. Summary of the depth of occurrence of intervals with evidence for MTDs identified by VCD and X-ray CT, Site C0018A.

Interval	Core, section, interval (cm)		Depth (mbsf)		Thickness (m)
	Top	Bottom	Top	Bottom	
	333-C0018A-	333-C0018A-			
1	1H-3, 45	1H-5, 56.4	1.425	4.277	2.852
2	5H-5, 35.3	6H-2, 90.5	39.451	46.727	7.276
3	7H-5, 24	8H-3, 59.5	58.013	65.745	7.732
4	8H-4, 20.6	8H-4, 75.5	66.437	66.934	0.497
5	9H-3, 39.5	11H-6, 103.5	75.914	94.37	18.456
6	15H-2, 91.5	23H-1, 68.7	127.545	188.573	61.028

Table T3. Results of bulk powder X-ray diffraction analysis, Hole C0018A. (Continued on next three pages.)

Lith. unit	Core, section, interval (cm)	Depth (mbsf)	Measured values of X-ray diffraction peaks: Peak intensity (counts/step)				Measured values of X-ray diffraction peaks: Integrated peak area (total counts)				Abundance calculated from SVD normalization factors: Absolute (wt%)					Abundance calculated from SVD normalization factors: Relative (wt%)			
			Clay minerals	Quartz	Feldspar	Calcite	Clay minerals	Quartz	Feldspar	Calcite	Clay minerals	Quartz	Feldspar	Calcite	Total	Clay minerals	Quartz	Feldspar	Calcite
	333-C0018A-																		
IAi	1H-1, 10	0.10	29	723	141	299	2,224	26,067	10,636	11,463	29.0	14.6	12.7	12.1	68.4	42	21	19	18
	1H-2, 21.5	0.98	39	752	121	331	2,939	26,600	9,766	12,675	35.5	14.8	11.2	13.2	74.7	47	20	15	18
	1H-6, 22	4.59	35	809	123	301	2,553	28,603	9,781	11,369	31.5	16.0	11.3	11.7	70.5	45	23	16	17
	1H-7, 69.5	5.28	33	744	124	252	2,621	28,120	10,070	10,255	32.4	15.7	11.7	10.2	70.0	46	22	17	15
	1H-8, 27.5	6.24	34	718	199	328	2,533	27,171	12,538	12,574	33.4	15.1	15.1	13.3	76.9	43	20	20	17
	2H-2, 21.5	8.06	36	668	128	347	2,676	25,131	9,514	13,653	32.8	14.0	11.0	14.7	72.5	45	19	15	20
	2H-6, 21.5	11.42	31	698	139	364	2,290	25,095	10,947	13,524	30.0	14.0	13.1	14.8	71.9	42	19	18	21
	2H-9, 20	14.27	33	620	121	391	2,104	22,425	9,893	15,763	27.6	12.5	11.8	18.0	69.9	40	18	17	26
	2H-10, 21.5	14.75	32	693	123	344	2,460	25,861	10,081	12,736	31.0	14.4	11.8	13.7	70.9	44	20	17	19
	2H-11, 8	14.84	35	704	121	353	2,826	27,417	9,885	13,788	34.4	15.3	11.4	14.7	75.8	45	20	15	19
	3H-2, 133	18.71	31	781	169	185	1,906	29,126	11,766	7,396	26.4	16.3	14.2	6.9	63.8	41	26	22	11
	3H-4, 46	20.19	36	740	121	302	2,702	27,159	10,420	12,310	33.6	15.1	12.2	12.9	73.7	46	21	17	17
	3H-5, 22	20.90	31	762	125	313	2,364	27,175	10,418	12,624	30.2	15.2	12.3	13.5	71.2	42	21	17	19
	3H-8, 15	23.71	31	780	180	216	2,174	31,707	13,964	9,745	30.6	17.7	17.0	9.6	74.9	41	24	23	13
															Average:	44	21	18	18
IAii	4H-4, 20	29.42	13	73	71	26	1,162	4,310	6,017	1,369	34.0	16.1	12.0	12.5	74.6	46	22	16	17
	5H-1, 70	35.80	33	793	139	330	2,755	28,871	10,394	12,067	33.5	11.9	7.8	23.4	76.6	44	16	10	31
	5H-2, 20	36.65	28	588	89	499	2,875	21,416	7,112	20,266	28.0	15.4	12.5	19.0	75.0	37	21	17	25
	5H-4, 21.5	39.11	25	777	125	414	2,111	27,517	10,580	16,675	26.0	11.4	12.0	17.3	66.7	39	17	18	26
	5H-7, 127	43.02	26	559	126	389	1,928	20,579	9,923	15,085	33.8	15.1	14.2	15.9	79.0	43	19	18	20
	5H-8, 30	43.45	37	653	111	322	2,740	22,945	8,309	12,041	32.6	12.7	9.5	12.7	67.5	48	19	14	19
	6H-4, 21	48.43	39	814	140	266	3,048	29,822	10,511	10,864	36.9	16.6	12.1	10.6	76.2	48	22	16	14
	6H-5, 124.5	49.56	33	773	151	349	2,638	28,265	10,493	14,392	33.0	15.8	12.2	15.6	76.6	43	21	16	20
	6H-7, 118	52.04	32	612	140	331	2,395	23,331	9,532	13,119	30.1	13.0	11.2	14.3	68.6	44	19	16	21
	6H-9, 13.0	53.27	19	153	96	51	1,714	6,374	8,191	2,587	22.7	3.1	10.4	1.6	37.9	60	8	28	4
															Average:	45	18	17	20
IAiii	7H-3, 47	57.13	15	244	189	87	1,445	8,852	15,662	4,069	25.5	4.3	20.6	3.4	53.8	47	8	38	6
	7H-3, 80	57.43	24	592	111	726	1,394	21,319	8,270	27,789	20.0	12.0	9.8	34.3	76.2	26	16	13	45
	7H-4, 23	57.79	21	249	205	106	2,051	9,920	13,163	3,927	29.6	5.0	17.0	2.8	54.3	54	9	31	5
	7H-9, 134	61.65	30	609	112	659	2,093	22,998	7,667	25,112	26.3	12.9	8.7	30.3	78.2	34	17	11	39
	8H-6, 21	66.83	26	624	105	665	2,244	22,685	8,247	23,320	28.1	12.7	9.5	27.8	78.1	36	16	12	36
	8H-9, 37	67.69	38	660	111	459	2,576	24,515	9,470	17,971	32.0	13.7	11.0	20.5	77.1	41	18	14	27
	8H-9, 112.5	70.45	40	752	131	374	2,703	27,525	9,306	15,428	32.9	15.4	10.6	17.0	75.9	43	20	14	22
	9H-4, 119	71.13	25	429	133	337	1,677	15,736	11,030	13,401	24.4	8.6	13.8	15.4	62.2	39	14	22	25
	9H-4, 130	77.99	25	586	103	598	1,679	20,991	9,290	23,146	23.4	11.8	11.2	28.0	74.3	31	16	15	38
	10H-2, 68	78.10	27	561	88	406	2,431	20,588	7,455	14,774	29.1	11.4	8.5	16.6	65.7	44	17	13	25
	10H-4, 21	81.21	29	589	109	315	2,570	22,432	9,815	12,248	32.0	12.4	11.6	13.1	69.1	46	18	17	19
	10H-7, 63	83.32	26	697	148	255	2,403	24,938	11,994	9,496	31.7	13.8	14.5	9.4	69.5	46	20	21	14
	10H-8, 129	86.36	17	275	172	106	1,530	10,451	14,781	5,039	25.6	5.3	19.3	4.6	54.8	47	10	35	8
	10H-9, 8	88.22	31	726	149	241	2,471	26,004	11,809	9,979	32.2	14.4	14.2	10.0	70.8	46	20	20	14
	10H-9, 87	88.40	35	739	131	218	2,622	27,058	10,926	9,267	33.0	15.1	12.9	8.9	69.9	47	22	18	13
	11H-2, 55	89.10	40	867	140	191	2,911	31,038	11,268	7,517	35.9	17.3	13.1	6.3	72.6	49	24	18	9

Table T3 (continued). (Continued on next page.)

Lith. unit	Core, section, interval (cm)	Depth (mbsf)	Measured values of X-ray diffraction peaks: Peak intensity (counts/step): Clay minerals	Quartz	Feldspar	Calcite	Integrated peak area (total counts): Clay minerals	Quartz	Feldspar	Calcite	Abundance calculated from SVD normalization factors: Absolute (wt%): Clay minerals	Quartz	Feldspar	Calcite	Total	Relative (wt%): Clay minerals	Quartz	Feldspar	Calcite
	11H-8, 94	90.68	38	838	131	246	3,000	30,666	10,195	9,522	36.1	17.1	11.6	8.9	73.7	49	23	16	12
	11H-9, 22	96.71	39	772	117	307	3,251	27,082	9,096	12,529	38.0	15.1	10.2	12.8	76.1	50	20	13	17
	11H-10, 61	97.13	42	811	134	259	3,052	29,193	10,120	10,885	36.6	16.3	11.6	10.7	75.2	49	22	15	14
	11H-11, 18.5	97.66	29	739	116	215	2,665	26,775	9,633	9,022	32.5	14.9	11.1	8.6	67.2	48	22	17	13
	12H-4, 68	98.48	38	808	161	223	2,792	30,098	11,089	9,082	34.7	16.8	12.9	8.5	72.9	48	23	18	12
	12H-5, 21.5	102.88	37	776	137	312	2,434	28,065	11,531	12,667	31.7	15.7	13.7	13.5	74.5	43	21	18	18
	12H-8, 120.5	103.56	34	731	142	298	2,763	26,947	10,596	11,857	34.3	15.0	12.4	12.2	73.9	46	20	17	17
	12H-9, 20	107.32	33	795	152	310	3,200	29,253	11,281	12,092	39.0	16.2	13.1	12.1	80.5	48	20	16	15
	13H-4, 125.5	107.70	33	824	160	239	2,402	28,849	13,008	9,454	32.3	16.1	15.7	9.2	73.3	44	22	21	13
	13H-5, 108.5	111.37	32	731	144	286	2,389	26,124	11,475	10,728	31.2	14.5	13.8	11.0	70.5	44	21	20	16
	13H-6, 22	112.40	29	963	173	258	2,647	33,298	13,650	9,028	34.9	18.6	16.3	8.3	78.2	45	24	21	11
	14H-4, 20	112.67	38	804	148	243	3,134	28,414	10,148	9,406	37.5	15.8	11.6	8.7	73.6	51	21	16	12
	14H-5, 21.5	121.37	35	808	162	323	2,559	30,013	11,118	12,454	32.5	16.8	13.0	13.1	75.4	43	22	17	17
	14H-6, 128	122.64	29	752	129	370	2,736	27,448	10,137	13,437	33.7	15.3	11.7	14.3	75.1	45	20	16	19
	14H-7, 30	123.93	35	661	112	451	2,533	24,036	8,887	18,103	31.2	13.4	10.2	20.7	75.5	41	18	14	27
	14H-7, 49	124.39	42	888	129	313	3,113	31,770	10,615	11,769	37.5	17.8	12.1	11.7	79.1	47	22	15	15
	15H-2, 65	124.58	49	789	133	222	2,821	28,293	9,930	9,552	34.2	15.8	11.4	9.2	70.6	48	22	16	13
	15H-2, 68	127.31	35	743	132	258	3,235	27,787	10,229	10,303	38.6	15.4	11.7	9.8	75.6	51	20	16	13
	15H-2, 107	127.34	31	735	137	242	2,525	25,411	10,100	11,985	31.6	14.1	11.9	12.6	70.3	45	20	17	18
	15H-3, 33	127.68	35	860	154	267	2,495	30,368	11,238	11,955	31.9	17.0	13.2	12.4	74.6	43	23	18	17
	15H-5, 22	128.07	33	869	181	226	2,580	32,012	13,092	9,163	33.9	17.9	15.6	8.6	76.1	45	24	21	11
	15H-7, 80	130.27	45	1,073	189	100	3,380	38,199	14,161	4,427	42.1	21.3	16.6	1.6	81.7	52	26	20	2
	15H-9, 71	132.26	32	855	136	312	2,798	29,770	10,386	13,107	34.4	16.7	12.0	13.8	76.8	45	22	16	18
IAiii	15H-9, 84	134.70	33	628	216	298	3,086	22,236	12,635	11,770	39.2	12.1	15.3	12.0	78.5	50	15	20	15
	16H-2, 60	134.81	35	837	142	156	3,207	30,615	10,811	6,421	38.4	17.0	12.4	4.7	72.6	53	23	17	6
	16H-11, 12	138.22	39	768	155	277	2,713	29,033	11,060	11,231	34.0	16.2	13.0	11.4	74.5	46	22	17	15
	16H-11, 122	142.57	31	796	166	238	2,666	29,883	11,623	9,918	33.8	16.7	13.7	9.6	73.9	46	23	19	13
	16H-12, 25	143.66	32	776	126	362	2,530	28,614	10,174	13,160	31.6	16.0	11.8	14.1	73.6	43	22	16	19
	17H-1, 50	144.10	35	1,130	225	95	3,062	41,236	18,949	3,820	42.3	23.0	23.1	0.8	89.2	47	26	26	1
	17H-2, 39	145.11	37	925	160	146	2,915	32,836	12,183	6,156	36.4	18.3	14.3	4.4	73.5	50	25	19	6
	17H-3, 110	146.32	32	700	110	393	2,234	25,770	9,061	16,328	28.2	14.5	10.5	18.6	71.7	39	20	15	26
	17H-5, 26	148.28	37	784	210	280	2,738	28,966	13,029	11,275	35.7	16.1	15.7	11.3	78.8	45	20	20	14
	17H-6, 19	149.43	44	799	138	238	3,285	29,014	11,018	10,237	39.6	16.1	12.7	9.7	78.1	51	21	16	12
	18H-3, 11.5	149.61	37	865	162	187	2,782	32,060	12,123	7,470	35.2	17.9	14.3	6.3	73.6	48	24	19	9
	18H-4, 27.5	156.35	36	1,085	247	50	2,973	38,903	18,155	2,473	40.9	21.6	22.2	0.1	84.8	48	26	26	Tr
	18H-5, 98.5	157.95	39	881	195	206	2,536	31,841	13,059	8,029	33.4	17.8	15.6	7.2	74.0	45	24	21	10
	19H-1, 121.5	158.88	35	812	226	305	2,697	29,091	13,552	12,471	35.7	16.1	16.4	12.9	81.1	44	20	20	16
	19H-3, 46.5	160.67	49	900	130	192	3,023	31,215	9,840	8,022	35.9	17.5	11.1	6.9	71.4	50	24	16	10
	19H-4, 26.5	162.39	44	811	128	229	3,572	30,083	9,978	9,346	41.6	16.7	11.2	8.3	77.8	53	21	14	11
	19H-5, 59	162.75	51	973	149	159	3,431	36,112	12,762	6,483	41.8	20.2	14.8	4.4	81.1	52	25	18	5
	19H-6, 8	163.25	35	1,055	157	123	2,855	36,720	12,313	4,618	35.7	20.6	14.3	2.3	72.9	49	28	20	3
	20H-3, 44	163.94	40	930	159	102	3,382	34,234	12,571	4,831	41.2	19.1	14.6	2.3	77.2	53	25	19	3
	20H-3, 123.5	166.60	45	881	130	227	3,493	30,810	10,319	8,269	41.0	17.1	11.6	6.9	76.7	53	22	15	9
	20H-5, 21	168.89	38	731	123	361	3,035	26,816	10,139	14,184	36.7	14.9	11.7	15.1	78.4	47	19	15	19
	20H-6, 125	170.10	36	889	146	228	3,252	31,514	12,451	9,384	40.2	17.5	14.6	8.4	80.7	50	22	18	10
	20H-7, 129.5	171.54	37	909	142	202	2,968	32,176	11,361	7,996	36.5	18.0	13.2	6.9	74.4	49	24	18	9
	20H-8, 119	172.83	37	862	143	206	3,193	30,381	11,545	8,144	38.9	16.9	13.4	6.9	76.1	51	22	18	9

Table T3 (continued). (Continued on next page.)

Lith. unit	Core, section, interval (cm)	Depth (mbsf)	Measured values of X-ray diffraction peaks: Peak intensity (counts/step): Clay minerals	Quartz	Feldspar	Calcite	Integrated peak area (total counts): Clay minerals	Quartz	Feldspar	Calcite	Abundance calculated from SVD normalization factors: Absolute (wt%): Clay minerals	Quartz	Feldspar	Calcite	Total	Relative (wt%): Clay minerals	Quartz	Feldspar	Calcite
IAiii	21H-3, 20	176.79	38	925	177	206	2,721	33,814	13,168	7,767	35.2	18.9	15.6	6.6	76.4	46	25	20	9
	21H-5, 17	177.18	43	941	187	153	3,028	35,440	13,862	6,880	38.7	19.8	16.4	5.2	80.0	48	25	21	6
	22H-2, 35	179.26	37	703	136	231	2,568	25,879	11,065	10,442	32.7	14.4	13.2	10.5	70.8	46	20	19	15
	22H-2, 110	180.01	35	701	149	250	2,601	26,636	10,758	10,058	32.7	14.8	12.7	10.0	70.3	47	21	18	14
	22H-5, 29	181.35	35	753	178	355	2,884	27,428	12,984	12,543	37.2	15.1	15.6	12.9	80.9	46	19	19	16
	22H-7, 55	182.39	35	760	132	274	2,929	27,885	9,457	11,498	35.0	15.6	10.7	11.7	73.0	48	21	15	16
															Average:	46	21	18	15
IB	24T-1, 36	191.01	35	1,522	432	25	2,262	54,068	21,979	1,302	35.9	30.5	26.9	0.1	93.4	38	33	29	Tr
	24T-2, 20	192.26	40	1,012	190	34	3,350	36,019	12,993	1,296	41.0	20.1	15.1	0.1	76.3	54	26	20	Tr
	24T-2, 102	193.08	36	1,058	197	125	2,885	37,177	14,241	5,029	37.4	20.8	16.9	2.8	77.9	48	27	22	4
	24T-3, 27	193.74	44	1,124	184	31	3,732	38,336	13,911	1,287	45.3	21.3	16.2	0.1	82.9	55	26	19	Tr
	24T-5, 114	196.29	35	1,124	229	76	2,649	39,517	14,254	2,929	34.8	22.2	16.9	0.1	74.1	47	30	23	Tr
	25T-1, 66	200.81	44	1,167	221	59	3,062	42,532	15,284	2,805	39.5	23.9	18.0	0.1	81.5	48	29	22	Tr
	25T-2, 93	202.49	24	2,182	566	18	1,256	71,383	31,966	1,287	32.4	40.4	40.1	0.1	113.0	29	36	35	Tr
	27T-2, 52	219.98	25	1,599	428	50	1,595	54,835	24,265	2,242	31.0	30.9	30.2	0.1	92.2	34	34	33	Tr
	27T-3, 44	221.37	39	1,243	237	59	2,734	43,450	14,761	2,367	35.8	24.5	17.4	0.1	77.8	46	31	22	Tr
	27T-3, 116	222.09	42	1,144	215	20	3,458	40,479	16,656	1,171	44.5	22.5	19.9	0.1	87.0	51	26	23	Tr
	27T-4, 66	222.97	27	1,804	379	31	1,784	61,940	23,322	1,378	31.8	35.1	28.5	0.1	95.5	33	37	30	Tr
	27T-5, 24	223.66	37	1,270	221	60	2,540	46,069	16,926	2,509	35.4	26.0	20.3	0.1	81.7	43	32	25	Tr
	27T-8, 47	226.79	35	1,420	528	48	2,222	49,414	25,171	1,832	38.1	27.6	31.5	0.1	97.3	39	28	32	Tr
	27T-8, 80	227.12	35	1,160	261	46	2,790	40,507	15,678	1,952	37.2	22.7	18.8	0.1	78.8	47	29	24	Tr
	28T-3, 43	231.90	50	922	132	83	4,364	33,095	9,640	4,138	48.8	18.4	10.4	0.8	78.4	62	23	13	1
	28T-3, 105	232.52	34	1,329	316	91	2,533	45,893	17,768	3,674	36.0	25.8	21.4	0.9	84.1	43	31	25	1
	28T-4, 26	232.87	30	1,733	356	78	2,025	59,133	25,484	3,288	35.9	33.4	31.5	0.0	100.9	36	33	31	Tr
	29T-1, 68	238.83	36	1,518	294	35	2,618	50,251	19,317	1,351	37.7	28.3	23.3	0.1	89.4	42	32	26	Tr
	29T-4, 52	242.00	47	1,078	152	52	3,781	37,478	11,035	2,211	43.8	21.0	12.2	0.1	77.1	57	27	16	Tr
	29T-4, 127	242.75	44	936	181	89	2,933	35,242	13,302	3,513	37.2	19.7	15.7	0.9	73.4	51	27	21	1
	29T-5, 43	243.29	37	1262	246	68	2,703	43,088	16,209	2,764	36.6	24.2	19.4	0.1	80.3	46	30	24	Tr
	29T-6, 30	244.05	37	1,355	230	24	2,539	47,049	15,574	510	34.3	26.6	18.4	0.1	79.3	43	34	23	Tr
	30T-1, 30.5	247.96	44	902	166	40	3,457	34,725	11,628	1,593	41.1	19.4	13.3	0.1	73.9	56	26	18	Tr
	30T-2, 104	250.11	39	1,115	304	21	3,496	39,989	17,613	859	45.6	22.2	21.2	0.1	89.1	51	25	24	Tr
	31X-2, 105.5	259.38	32	1,396	264	52	2,769	48,299	18,335	2,224	38.6	27.2	22.0	0.1	87.9	44	31	25	Tr
	31X-4, 31.5	260.84	32	1,378	324	52	2,333	47,175	19,907	2,352	35.4	26.5	24.4	0.1	86.4	41	31	28	Tr
	31X-5, 14	260.99	47	981	136	21	4,102	34,469	10,956	1,075	47.0	19.1	12.2	0.1	78.4	60	24	16	Tr
	31X-6, 69	262.99	24	1,840	355	37	1,110	58,575	28,356	1,562	28.9	33.0	35.8	0.1	97.8	30	34	37	Tr
	32X-2, 17	268.23	30	1,442	300	64	2,310	48,200	20,245	2,755	35.4	27.1	24.8	0.1	87.4	41	31	28	Tr
	32X-2, 101.5	269.07	45	908	179	119	2,648	33,676	13,773	4,142	34.8	18.8	16.5	1.9	72.0	48	26	23	3
	32X-5, 92	273.20	26	1,933	485	20	1,367	64,246	30,982	737	33.1	36.2	39.0	0.1	108.4	31	33	36	Tr
	33X-6, 25.5	281.28	41	1,193	206	38	3,696	41,220	15,582	1,664	46.0	23.0	18.3	0.1	87.5	53	26	21	Tr
	33X-7, 31	281.60	47	1,126	206	31	3,769	40,397	14,569	1,737	46.1	22.5	17.0	0.1	85.7	54	26	20	Tr
	33X-8, 37	282.60	53	1,069	168	17	4,193	37,803	12,422	613	48.8	21.0	14.0	0.1	83.9	58	25	17	Tr
	33X-9, 36	283.13	24	1,695	339	22	1,849	57,873	25,618	727	34.2	32.6	31.8	0.1	98.8	35	33	32	Tr
	34X-2, 19	287.34	44	938	150	13	3,770	32,405	11,212	581	44.0	18.0	12.7	0.1	74.8	59	24	17	Tr
	34X-6, 24	290.17	32	1,388	311	20	2,126	47,713	20,457	995	33.7	26.8	25.2	0.1	85.8	39	31	29	Tr
	34X-7, 83	291.01	44	998	201	53	3,345	34,683	13,701	2,284	41.5	19.3	16.2	0.1	77.1	54	25	21	Tr

Table T3 (continued).

Lith. unit	Core, section, interval (cm)	Depth (mbsf)	Measured values of X-ray diffraction peaks: Peak intensity (counts/step)				Measured values of X-ray diffraction peaks: Integrated peak area (total counts)				Abundance calculated from SVD normalization factors: Absolute (wt%)					Abundance calculated from SVD normalization factors: Relative (wt%)			
			Clay minerals	Quartz	Feldspar	Calcite	Clay minerals	Quartz	Feldspar	Calcite	Clay minerals	Quartz	Feldspar	Calcite	Total	Clay minerals	Quartz	Feldspar	Calcite
IB	35X-4, 21.5	298.23	47	896	128	60	4,329	32,609	10,346	2,351	48.9	18.0	11.4	0.1	78.4	62	23	14	Tr
	36X-2, 63	305.55	42	1,017	205	41	3,571	36,590	13,099	1,963	43.2	20.4	15.2	0.1	78.9	55	26	19	Tr
	36X-3, 85	306.62	23	1,630	341	41	1,320	53,784	27,604	1,868	30.7	30.2	34.9	0.1	95.9	32	32	36	Tr
	36X-4, 92	307.77	42	872	159	101	3,568	31,827	11,344	4,205	42.2	17.7	13.0	1.5	74.4	57	24	17	2
	36X-4, 110	307.95	43	965	153	192	3,398	34,259	11,124	6,746	40.4	19.1	12.6	4.8	77.0	52	25	16	6
	36X-5, 24	308.43	34	1,525	271	50	2,401	50,969	21,042	2,314	36.8	28.7	25.7	0.1	91.3	40	31	28	Tr
	36X-8, 52	311.29	37	1,222	282	33	2,630	42,203	17,632	1,166	36.9	23.6	21.4	0.1	82.1	45	29	26	Tr
															Average:	46	29	24	1

SVD = singular value decomposition. Tr = trace.

Table T4. Intervals with evidence for mass transport deposits (MTDs) identified by visual core description (VCD) and X-ray computed tomography (CT), Hole C0018A. (Continued on next three pages.)

Interval	Core, section, interval (cm) Top	Core, section, interval (cm) Bottom	Depth (mbsf) Top	Depth (mbsf) Bottom	Thickness (m)	Internal structures and observation from X-ray CT: Core, section, interval (cm) Top	Internal structures and observation from X-ray CT: Core, section, interval (cm) Bottom	Internal structures and observation from X-ray CT: Depth (mbsf) Top	Internal structures and observation from X-ray CT: Depth (mbsf) Bottom	Internal structures and observation from X-ray CT: Thickness (m)	Description notes
	333-C0018A-	333-C0018A-				333-C0018A-	333-C0018A-				
1	1H-3, 45	1H-5, 56.4	1.425	4.277	2.852	1H-3, 45	1H-3, 135	1.425	2.3	0.875	Coherent interval with relatively higher CT number, consistent tilt of strata (as evidenced by high-CT number lines).*
						1H-3, 135	1H-5, 56.4	2.3	4.277	1.977	Mud clasts "flowing" in matrix, which shows some sort of lamination in the lower part of this interval. Subvertical high-CT number lines extend for several tens of centimeters and crosscut layers and clast. Base is defined by a sharp change in CT number from lower (above) to higher (below); there potentially could be a thin layer but CT image is not conclusive. The strata immediately above the base is faintly horizontally "laminated," which may indicate shear. The reasoning behind this interpretation is that primary lamination in bioturbated strata is not expected. It cannot completely excluded from CT scan that below, there is some more tilted and deformed strata. Therefore the base of this interval is not clearly defined.
2	5H-5, 35.3	6H-2, 90.5	39.451	46.727	7.276	5H-5, 24	5H-5, 35.3	39.346	39.451	0.105	Succession of thin, few millimeter thick volcaniclastic sand laminae, overlying a thin 1 cm thick layer with mud clasts. This layer immediately overlies the "debrite" defined as top of MTD Interval 2 and is interpreted as the turbidite deposit associated to this "mass-movement event."
						5H-5, 35.3	5H-8, 44	39.451	43.579	4.128	Chaotic mixed sediment, convolute bedding with folded and disturbed ash layers (debrite).
						5H-8, 44	6H-2, 90.5	43.579	46.727	3.148	Tilted strata as evidenced both from inclined layers and tilted orientation of high-CT number lines. Boundary between upper mixed sediment and lower tilted strata is a thin millimeter thick inclined higher CT number laminae that truncates high-CT number lines. High-CT number lines immediately below this thin layer are all oriented parallel to this inclined layer, possibly indicating shear. Interval 6H-2, 90 cm, prominent, slightly inclined contact between high CT number (above) and low CT number (below). High-CT number lines are well pronounced and parallel to inclined contact and may indicate shear. Below in low-CT number strata, no occurrence of high-CT number lines, but homogeneous bioturbated mud. Ash layer below at interval 6H-3, 10–20 cm, is horizontally stratified and looks undisturbed.
3	7H-05, 24	8H-3, 59.5	58.013	65.745	7.732	7H-5, 24	7H-5, 60.3	58.013	58.342	0.329	This interval has been described as mixed sediment on VCD. In CT images no associated features can be identified.
						7H-5, 60.3	8H-3, 59.5	58.342	65.745	7.403	Below interval 7H-5, 61 cm, high-CT number lines are chaotically oriented in the uppermost part but develop clear tilted orientation further downsection. Dipping layers occur at intervals 7H-7, 38 cm; 7H-10, 29 cm; 7H-11, 28 cm; and 7H-11, 63 cm. Persistent orientation of tilted high-CT number lines occasionally abruptly change orientation along inclined millimeter thick layers with higher CT numbers (interval 7H-10, 29–31 cm, and 7H-11, 81–91 cm). These layers possibly indicate internal shear zones. A structure indicating folding of a diffuse, slightly higher CT number layer is observed in interval 7H-8, 18–22 cm.

Table T4 (continued). (Continued on next page.)

Interval	Core, section, interval (cm) Top	Core, section, interval (cm) Bottom	Depth (mbsf) Top	Depth (mbsf) Bottom	Thickness (m)	Internal structures and observation from X-ray CT: Core, section, interval (cm) Top	Core, section, interval (cm) Bottom	Depth (mbsf) Top	Depth (mbsf) Bottom	Thickness (m)	Description notes
											The base of interval 8H-3, 60 cm, is a thin, high CT number, 2 mm thick layer, mapped as clay in VCD. Above, high-CT number lines are scattered but show a clear tendency to orient parallel to the clay layer immediately above it, possibly indicating enhanced shear above this clay layer, which may potentially represent the base of MTD within this interval. Below, high-CT number lines are rare, and normal faults are present.
4	8H-4, 20.6	8H-4, 75.5	66.437	66.934	0.497	8H-4, 20.6	8H-4, 75.5	66.437	66.934	0.497	Folded volcaniclastic sand or ash layer (smear slide description shows texture = 60% sand, and composition = dominant volcanic glass) identified in VCD. X-ray CT is inconclusive because of heavy gas expansion at the top of this layer; however, fold axis appears to be perpendicular to coring axis. Above and below this layer the strata look undisturbed, however, affected by steeply dipping normal faults.
5	9H-3, 39.5	11H-6, 103.5	75.914	94.37	18.456	9H-3, 39.5	9H-4, 141	75.914	78.203	2.289	Because of heavy coring disturbance (likely due to gas expansion and the fact that this core got jammed in the core barrel) the top of this interval is not well defined. Top 39.5 cm of Section 9H-3 shows flow structures that may be related to coring disturbances. Below Section 9H-3, 39.5 cm, clear evidence for mixed sediment including mud clasts and chaotically-to-partly consistent inclined orientation of high-CT number lines. In the lowermost part of this interval identified as mixed sediment in VCD, is a subhorizontally stratified volcanic fine ash layer that is affected by normal faulting.
						9H-4, 141	10H-8, 130	78.203	88.229	10.026	Below Section 9H-4, 141 cm, CT shows persistent orientation of tilted high-CT number lines that occasionally abruptly change orientation along inclined millimeter-thick layers (Section 10H-6, 38 cm). These layers possibly indicate internal shear zones. Dipping beds occur at intervals 10H-8, 74 cm, and 10H-8, 130 cm. However, this interval also contains a subhorizontal ash layer at interval 10H-7, 141 cm. Some flow structures occur in Section 10H-3 but may be due to coring disturbance/degassing.
						10H-8, 130	10H-9, 10	88.229	88.422	0.193	Thin interval associated with disrupted ash layer showing mixed sediment with mud clasts.
						10H-9, 10	11H-6, 27	88.422	93.712	5.29	This interval shows persistent orientation of tilted high-CT number lines that occasionally change orientation (interval 10H-6, 38 cm). Dipping discrete (often ash) layers occur at intervals 10H-9, 93 cm; 11H-2, 10 cm; 11H-3, 15 cm; 11H-3, 60 cm; and 11H-1, 7–20 cm. The latter interval shows two subhorizontal ash layers, which are slightly dipping in two different directions, possibly indicating folding. The character of persistent tilted high-CT number lines stops at interval 11H-6, 26 cm, immediately above a tilted ash layer.
						11H-6, 27	11H-6, 103.5	93.712	94.37	0.658	Below this tilted ash layer, high-CT number lines are somewhat chaotically oriented in the upper part and become successively strongly aligned, forming subhorizontal lineaments. If high-CT number lines can be assumed to represent stretch lineations, this strongly indicates increased shear toward the bottom of this interval with evidence for MTD. At interval 11H-6, 52 cm, a flat-lying fold with subhorizontal fold axis parallel to lineations indicates soft-sediment deformation in a ductile mode.

Table T4 (continued). (Continued on next page.)

Interval	Core, section, interval (cm) Top	Core, section, interval (cm) Bottom	Depth (mbsf) Top	Depth (mbsf) Bottom	Thickness (m)	Internal structures and observation from X-ray CT: Core, section, interval (cm) Top	Core, section, interval (cm) Bottom	Depth (mbsf) Top	Depth (mbsf) Bottom	Thickness (m)	Description notes
											Below interval 11H-6, 103.5 cm, there is no evidence for deformed sediment in CT, even for the horizontally layered ash layer that appears as broken layer in the split image core photo.
6	15H-2, 91.5	23H-01, 68.7	127.545	188.573	61.028	15H-2, 83	15H-2, 91.5	127.474	127.545	0.071	Turbidite overlying MTD.
						15H-2, 91.5	15H-3, 71	127.545	128.406	0.861	Mixed sediment, debrite.
						15H-3, 71	15H-8, 60	128.406	133.345	4.939	Coherent intervals showing persistent orientation of inclined high-CT number lines perpendicular to tilted strata. Orientation of both high-CT number lines and tilted bed changes approximately between interval 15H-6, 135 cm, and 15H-7, 56 cm; in Section 15H-7, between 60 and 103 cm (this change is associated to a steeply dipping, almost vertical zone). The whole interval occasionally shows internal contacts characterized by irregular transition "dissolving" into debrite. This is particularly evident for discrete beds in intervals 15H-4, 104 cm, and 15H-8, 60 cm. Occasional occurrence of steeply dipping normal faults truncating high-CT number lines.
						15H-8, 60	16H-10, 16.5	133.345	141.844	8.499	Mixed sediment, debrite. CT scans show partly chaotic orientations of high-CT number lines and partly strongly elongated subhorizontal orientation. Original flow structures and convolute structures can be clearly distinguished from drilling-induced flow-in structures to Section 15H-9, 120 cm. Core 15H has coring-induced flow-in below interval 15H-9, 100 cm. Core 16H is heavily disturbed due to core liner splitting and working out from the core barrel, however, shows clear indication for mixed sediment (debrite). There are thin intervals (e.g., 16H-2, 4–97 cm; 16H-2, 105–115 cm; and 16H-4, 125 cm, to 16H-10, 10 cm) that show more coherent tilted strata and inclined high-CT number lines. These intervals can be possibly interpreted as clasts (bigger than core scale) within the debrite.
						16H-10, 16.5	18H-2, 30	141.844	155.136	13.292	More coherent strata, showing subvertical orientation of high-CT number lines and subhorizontal sand layers (e.g., at interval 17H-1, 70 cm) in the upper part, and more steeply dipping beds (e.g., in Section 18H-2) and inclined high-CT number lines in the lower part. Internal, steeply dipping zones at intervals 17H-2, 110 cm; 17H-3, 50–60 cm; and 17H-6, 53–74 cm, separate individual coherent intervals showing persistent orientation of tilted high-CT number lines. Steeply dipping normal faults and web structures (e.g., at interval 17H-7, 20 cm) are occasionally present.
						18H-2, 30	18H-3, 90	155.136	157.092	1.956	Interval showing flow structures, mud clasts, near-vertical slightly folded contacts between two disintegrated sediment masses between intervals 18H-2, 120 cm, and 18H-3, 20 cm, and a slump fold at interval 18H-3, 90 cm.
						19H-top	19H-5, 20	159.65	162.756	3.106	Coherent intervals showing persistent orientation of tilted high-CT number lines. Orientation of high-CT number lines changes along dipping and occasionally folded contacts (e.g., in Section 19H-3).
						19H-5, 20	19H-5, 80	162.924	163.429	0.505	Interval with inclined thin (5 m scale) sand layers.

Table T4 (continued).

Interval	Core, section, interval (cm) Top	Core, section, interval (cm) Bottom	Depth (mbsf) Top	Depth (mbsf) Bottom	Thickness (m)	Internal structures and observation from X-ray CT: Core, section, interval (cm) Top	Core, section, interval (cm) Bottom	Depth (mbsf) Top	Depth (mbsf) Bottom	Thickness (m)	Description notes
						20H-2, 88	21H-2, 40	165.782	175.845	10.063	Core 20H top (above interval 20H-2, 80 cm) is fluidized and fully coring disturbed. Coherent interval with interbedded thin subcentimeter to centimeter sand layers that are partly disrupted and partly show subhorizontal layering (e.g., in Section 20H-3) and coherent mud intervals showing subvertical orientation of high-CT number lines. Partial occurrence of thin intervals, where strata are more deformed (deintegrated: e.g., interval 20H-5, 0–40 cm) and slightly inclined 3 cm thick sand layer at interval 21H-1, 80 cm. The lower parts of Core 20H-6, 1–6 cm, to 20H-CC: flow-in.
						21H-2, 40	21H-4, 10	175.845	176.892	1.047	Interval with folded and distorted thin sand layers. Upper boundary of this interval is a complex fault/shear zone structure. Lower boundary is a ~45° dipping surface truncating inclined sand laminae. High-CT number lines above this contact are aligned, indicating shearing along this contact.
						21H-4, 10	21H-5, 100	176.892	177.963	1.071	Dipping thin 0.5 cm sand laminae in cross-section view. Bedding change in dip at about interval 21H-5, 20 cm, where a fold can be observed in CT. The lower part of Core 21H shows coring-induced flow structures at the bottom.
						22H-1, 20	22H-4, 14	178.65	180.865	2.215	Top of interval 22H-1, 0–20 cm, is likely drilling disturbed with "flow-out" at the top. Coherent-looking homogeneous interval with subvertical orientation of high-CT number lines, with occasional indication for folding (e.g., interval 22H-2, 86–120 cm) and higher CT number deeply inclined to subvertical layers, along which high-CT number lines are preferentially aligned, possibly indicating shear (e.g., in Section 22H-4).
						22H-4, 14	22H-7, 10	180.865	181.94	1.075	Interval showing folds in CT, along which high-CT number lines are preferentially oriented.
						22H-7, 10	22H-8, 56	181.94	183.8	1.86	First appearance on VCD is rather homogeneous with subhorizontal sand layer at interval 22H-7, 116 cm. In CT scan, high-CT number lines show clear preferred orientation (e.g., interval 22H-8, 13–40 cm, with a possible localized shear zone at ~28 cm) and occasional change in orientation along possible fold structures (e.g., interval 22H-7, 115 cm). Section 22H-9 to base of core is coring-induced flow-in.
						23H-1, 0	23H-1, 68.7	187.95	188.573	0.623	Interval heavily coring disturbed because of gas expansion in the underlying sand during core recovery.

* = the term "lines" is being used as a descriptive word here, describing the sublinear features showing high CT number indicative for FeS mineralization (pyrite); this may be either mineralized bioturbation burrows, stretched and/or aligned pyrite minerals occurring as patches in "background" sediment, or may also be related to so-far unknown mineralized dewatering/degassing structures.

Table T5. Results of XRF analysis, Hole C0018A.

Lith. unit	Core, section, interval (cm)	Depth (mbsf)	Major element oxide (wt%)										LOI (wt%)	Total
			SiO_2	Al_2O_3	Fe_2O_3	MnO	MgO	CaO	Na_2O	K_2O	TiO_2	P_2O_5		
	333-C0018A-													
IAi	1H-1, 10.0–13.0	0.12	60.3	14.4	5.17	0.07	2.49	8.55	3.76	2.68	0.60	0.13	12.8	98.2
	1H-2, 21.5–22.5	1.01	59.3	15.0	5.16	0.07	2.37	9.65	3.25	2.87	0.60	0.11	12.7	98.4
	1H-6, 22.0–23.0	4.73	61.3	14.8	5.28	0.06	2.50	7.78	3.21	2.71	0.63	0.12	11.0	98.5
	1H-7, 69.5–72.5	5.45	62.2	14.9	4.83	0.06	2.21	7.41	3.27	3.08	0.58	0.10	10.3	98.6
	2H-2, 21.5–22.5	8.15	59.0	14.7	5.43	0.07	2.47	10.36	2.89	2.80	0.63	0.12	12.5	98.5
	2H-6, 21.5–22.5	11.73	60.2	14.2	4.90	0.07	2.17	9.93	3.12	2.83	0.59	0.12	11.5	98.2
	2H-10, 21.5–22.5	15.27	60.0	13.7	5.29	0.06	2.27	9.74	3.00	2.78	0.62	0.12	11.8	97.6
	3H-5, 22.0–23.0	21.23	59.7	14.3	5.25	0.07	2.23	9.75	3.00	2.80	0.60	0.12	11.5	97.9
IAii	4H-4, 20.0–21.0	29.77	58.8	15.6	5.70	0.08	2.51	8.65	2.72	3.09	0.67	0.11	10.5	97.9
	5H-4, 21.5–22.5	39.41	57.5	14.5	6.14	0.14	2.31	11.78	2.76	2.36	0.67	0.12	11.2	98.3
	6H-3, 26.0–28.0	47.74	73.4	13.2	1.85	0.05	0.45	1.39	4.12	4.40	0.22	0.05	4.7	99.1
	6H-4, 21.0–22.0	48.87	61.2	15.5	5.36	0.08	2.29	7.24	2.92	3.06	0.65	0.11	9.9	98.4
IAiii	7H-4, 23.0–24.0	58.18	65.7	15.1	3.64	0.07	1.38	4.69	3.89	2.88	0.42	0.13	6.0	97.9
	7H-9, 134.0–135.0	62.45	51.7	13.7	5.05	0.09	2.25	19.32	2.40	2.07	0.56	0.12	16.1	97.2
	8H-4, 65.0–67.0	67.19	65.1	14.0	5.70	0.16	1.49	5.20	4.75	1.46	0.66	0.18	5.5	98.8
	8H-6, 21.0–22.0	68.12	54.9	13.3	4.96	0.08	1.98	16.63	2.44	2.27	0.56	0.12	15.6	97.2
	8H-9, 37.0–38.0	71.17	57.6	14.6	4.90	0.11	2.24	12.70	2.65	2.71	0.60	0.12	13.8	98.3
	9H-4, 119.0–121.0	78.30	55.4	14.4	7.27	0.12	2.52	12.14	2.86	1.79	0.66	0.10	9.3	97.3
	9H-4, 130.0–132.0	78.41	52.4	13.2	5.27	0.09	2.10	18.93	2.38	2.01	0.56	0.12	15.7	97.1
	10H-2, 68.0–70.0	81.37	58.9	13.2	6.41	0.08	2.01	11.72	3.03	2.45	0.53	0.11	14.3	98.4
	10H-4, 21.0–22.0	83.76	60.8	14.9	5.08	0.08	2.03	9.04	3.12	2.71	0.60	0.12	10.0	98.5
	10H-7, 63.0–65.0	87.21	59.5	15.5	6.10	0.10	2.43	8.10	3.12	2.80	0.67	0.14	9.4	98.5
	10H-9, 8.0–10.0	89.54	59.5	15.5	5.56	0.09	2.44	8.30	2.96	2.70	0.66	0.13	9.9	97.8
	11H-9, 22.0–23.0	98.35	59.5	15.5	5.66	0.09	2.36	8.66	2.75	3.00	0.66	0.12	10.7	98.3
	12H-5, 21.5–22.5	103.90	59.0	15.2	5.52	0.11	2.32	9.42	2.78	2.79	0.65	0.13	11.0	97.9
	13H-6, 22.0–23.0	113.50	61.9	15.4	5.38	0.07	2.22	6.74	2.86	2.90	0.69	0.12	8.8	98.2
	14H-5, 21.5–22.5	122.65	59.9	15.2	5.58	0.08	2.28	8.76	2.73	2.84	0.64	0.12	10.3	98.1
	14H-7, 31.0–33.0	124.59	61.2	15.3	5.21	0.07	2.13	7.90	2.83	3.00	0.64	0.11	10.0	98.3
	15H-2, 68.0–70.0	127.45	60.6	15.3	5.58	0.08	2.41	6.93	3.00	3.01	0.65	0.12	9.2	97.7
	15H-5, 22.0–23.0	130.78	62.1	15.1	5.39	0.07	2.23	6.25	2.85	2.98	0.63	0.11	8.5	97.7
	15H-9, 71.0–72.0	135.82	58.9	15.3	5.36	0.07	2.34	9.46	2.66	2.77	0.64	0.11	10.3	97.6
	15H-9, 84.0–86.0	135.96	59.7	15.1	5.53	0.07	2.03	8.97	2.79	2.94	0.60	0.12	9.4	97.8
	16H-12, 25.0–26.0	144.19	59.7	15.1	5.49	0.10	2.37	8.96	2.71	2.91	0.64	0.13	10.6	98.0
	17H-5, 26.0–27.0	149.80	60.8	15.4	5.60	0.08	2.22	7.66	2.75	2.83	0.67	0.12	9.3	98.0
	18H-4, 27.5–28.5	158.23	66.1	15.8	5.19	0.06	2.27	2.15	2.82	2.99	0.68	0.11	5.0	98.2
	19H-4, 26.5–27.5	163.34	60.9	15.8	6.08	0.09	2.44	6.58	2.69	2.86	0.69	0.12	9.2	98.2
	19H-6, 6.0–8.0	164.74	64.0	15.4	5.77	0.07	2.01	3.79	2.69	2.92	0.65	0.11	6.8	97.4
	20H-3, 44.0–46.0	166.70	63.5	16.2	5.84	0.08	2.39	3.43	2.89	3.00	0.70	0.11	7.0	98.2
	20H-5, 21.0–22.0	169.10	58.8	15.7	5.82	0.09	2.44	9.79	2.59	2.74	0.69	0.13	11.2	98.8
	21H-3, 20.0–21.0	176.97	61.9	15.9	5.91	0.08	2.32	5.28	2.68	2.89	0.69	0.11	8.0	97.8
	21H-5, 16.0–17.0	177.38	62.7	15.7	5.74	0.08	2.27	5.09	2.71	2.91	0.67	0.12	8.0	97.9
	22H-5, 30.0–31.0	181.35	58.6	15.1	5.78	0.08	2.34	9.37	2.60	2.63	0.65	0.17	9.9	97.4
IB	24T-2, 20.0–22.0	193.74	64.9	16.7	5.70	0.06	2.40	1.64	2.79	3.05	0.75	0.10	6.0	98.1
	25T-1, 66.0–69.0	200.83	66.2	15.7	5.67	0.08	2.10	2.37	2.81	2.99	0.69	0.10	6.4	98.7
	25T-2, 93.0–96.0	202.51	75.1	11.6	3.67	0.05	1.16	1.36	2.69	2.48	0.46	0.06	2.7	98.7
	27T-2, 63.0–65.0	220.10	69.2	12.5	3.65	0.08	1.11	5.07	3.60	2.38	0.41	0.57	7.4	98.5
	27T-2, 86.0–88.0	220.33	68.7	13.4	4.08	0.06	1.44	3.45	2.55	2.77	0.57	0.09	5.4	97.1
	27T-5, 24.0–25.0	223.66	67.7	14.8	4.88	0.07	2.00	2.30	2.70	2.93	0.58	0.10	5.3	98.1
	27T-8, 45.0–47.0	226.78	68.9	14.0	4.54	0.08	1.74	2.11	2.70	2.69	0.59	0.06	5.0	97.4
	28T-4, 26.0–27.0	232.87	66.2	12.5	4.19	0.06	1.38	2.23	2.37	2.59	0.50	0.08	5.2	92.1
	29T-6, 30.0–31.0	244.06	67.9	15.2	4.82	0.07	2.02	1.48	2.72	2.78	0.67	0.09	4.4	97.7
	30T-1, 30.5–33.5	247.97	63.6	16.7	6.75	0.10	2.37	1.91	2.65	3.03	0.74	0.14	6.8	98.0
	31X-4, 31.5–32.5	260.84	69.7	14.1	4.46	0.06	1.54	2.03	2.87	2.76	0.58	0.09	4.9	98.2
	32X-2, 101.5–103.5	269.08	62.0	16.1	6.99	0.11	2.35	3.93	2.71	2.88	0.71	0.16	8.7	98.0
	32X-5, 92.0–95.0	273.22	75.3	12.5	3.29	0.05	1.17	1.46	2.82	2.71	0.47	0.06	3.2	99.8
	33X-6, 25.5–26.5	281.28	66.0	16.6	5.74	0.09	1.97	1.64	2.60	3.05	0.71	0.10	5.9	98.5
	34X-6, 24.0–25.0	290.17	69.3	14.7	4.75	0.08	1.80	1.79	2.84	2.64	0.64	0.09	4.7	98.7
	35X-4, 21.5–22.5	298.52	61.6	17.7	6.15	0.07	2.34	1.91	2.46	3.05	0.75	0.10	6.9	96.2
	36X-5, 24.0–25.0	308.43	69.1	14.5	4.76	0.07	1.66	1.95	2.72	2.78	0.63	0.08	5.1	98.2

LOI = Loss on ignition.

Table T6. Calcareous nannofossil range chart, Hole C0018A.

Age (Ma)	Core, section, interval (cm)	Preservation	*Amaurolithus* spp.	*Calcidiscus leptoporus*	*Calcidiscus macintyrei*	*Ceratolithus rugosus*	*Coccolithus pelagicus*	*Discoaster* sp.	*Emiliania huxleyi*	*Gephyrocapsa caribbeanica*	*Gephyrocapsa muellerae*	*Gephyrocapsa oceanica*	*Gephyrocapsa parallela*	*Gephyrocapsa* spp. (>5.5 µm)	*Gephyrocapsa* spp. (<3.5 µm)	*Helicosphaera carteri*	*Helicosphaera inversa*	*Helicosphaera sellii*	*Oolithotus fragilis*	*Phontosphaera japonica*	*Phontosphaera multipora*	*Phontosphaera* sp.	*Pseudoemiliania lacunosa*	*Reticulofenestra asanoi*	*Reticulofenestra pseudoumbilicus*	*Reticulofenestra* spp. (5–6 µm)	*Reticulofenestra* spp. (4–5 µm)	*Reticulofenestra* spp. (2.5–4 µm)	*Reticulofenestra* spp. (<2.5 µm)	*Rhabdosphaera clavigera*	*Rhabdosphaera stylifera*	*Scapholithus fossilis*	*Sphenolithus abies*	*Syracosphaera pulchra*	*Umbellosphaera irregularis*	*Umbilicosphaera sibogae*
	333-C0018A-																																			
0–0.291	1H-CC	W		C					C		R	A	C		A	C				R									R	R	+		R	+	R
	1H-CC	W		C					C		R	A	C		A	C				R									R	R	+		R	+	R
0.291–0.436	3H-CC	W		R		R	R				+	A	C		C	C				R		R						R	R	R	+		R	R	R
0.436–0.905	4H-CC	W		R		R	R				R	C	C		A	C				R		R	R					R	R	R	R	+	R	+	R
	5H-CC	W	r	R		R					+	C	R		C	C	+			R		R	C					R	R	R	R		R		C
	6H-CC	W		R		R	R	r			R	C	R		A	C	R			R			C					R	R	R	R		R		C
	7H-CC	W		R			R					R	R		A	R				+		+	C					R	R	R	R		R		R
	8H-CC	W		R			R				+	R	R		A	C			+	R		R	C					R	R	R	R		R		R
	9H-CC	W		R		+	R					A	C		A	C				R		R	C					R	R	R	R		R		R
	10H-CC	W		R		+	R					A	C		C	R				R		R	A					R	R	R	R		R		C
	11H-CC	W	r	R		+	R					C	C		C	R				R		R	A		r			R	R	R	R		R		R
	12H-CC	W		R		+	R					C	C		C	R			+	R		R	A	r?				R	R	R	R	+	R		R
	13H-CC	W		R		+	R	r				C	C		C	R				+		+	A					R	R	R	+		R		R
	14H-3, 69–70	W		C		+	R					+	+		A	R			+	+		R	C					R	R	R	+		R		C
	14H-6, 5–6	M		R			R					R	R		A	R				+		+	R				+	R	R	+			R		R
	14H-7, 105–106	W		C		+	C					C	C		A	R				R		R	C					R	R	R	+		R		C
	14H-CC	M		R			R					C	C		C	R			+	+		+	C					C	C	+			+		R
0.905–1.04	15H-2, 71–72	W		R		+	R					C	C		A	R			+	+		R	C	R		R	R	C	C	+	+		+		R
	15H-6, 70–71	W		R	r	+	R					C	C		A	R			+	+		R	C	R		R	C	C	C	+	+		+		R
	15H-CC	W		R			R					C	C		A	R			+	R		R	C	C		C	C	C	C	R			R		R
	16H-CC	M		R	r	+	R					C	C		A	C			R	R		R	C					C	C	R			R		C
1.04–1.136	17H-CC	M		R	r	+	R								C	R				+		R	C	C		C	C	C	C	R			R		C
?	18H-CC	P		+	r		+	r				r			R	R							R					R	R						R
1.04–1.136	19H-CC	M		R	r		R	r							+	R					R	R	C	R	r	C	C	C	C	R		r	R		R
	20H-CC	P		R	r		R								+	R					+		C	+				C	C						+
	21H-1, 61–62	M		R	r	+	R	r							R	R					+	+	C	R		C	C	C	C	+			R		R
	21H-5, 7–8	W		R	r		R	r							R	R					+	+	C	R		R	C	C	C	+		r	+		+
?	21H-CC	W		R	r		R			r		r			R	R					R	+	C	R	r	C	C	C	C			r	R		R
1.04–1.136	22H-CC	W		C			R								R	R					R	+	C	C		C	C	C	C	R			R		R
1.136–1.24	23H-1, 38–39	M		R	r	+	R	r							R	R				+		+	C			C	C	C	C	R		r	R		R
	23H-CC	M		R			R								R	R					R	R	C			R	C	C	C	R			R		R
	24T-1, 97–98	M		+			R								R	+							C					+	C				+		R
	24T-4, 129–130	W		R		+	+								C	R					+	R	C				C	C	A	R					C
1.24–1.46	24T-6, 52–53	M		R			R			R		C		C	C	R					R	+	C					R	C	+					R
	24T-CC	W		R			R			C		C		C	C	R					R	R	R				C	C	C	R			R		R
	25T-CC	M		R			R			C		C		C	C	R					R	R	R				+	C	C	R			+		R
	27T-2, 118–119	W		R			R			C		C		C	C	R					R	R	R					C	C	R			R		R
	27T-CC	W		R			R			C		C		C?	C	R					R	R	R					R	C	R			+		R
	28T-1, 36–37	W		R			R			C		C		C	C	R		+				+	R					R	R	R			R		R
	28T-2, 89–90	W		R			R			C		C		R	C	+		+				+	R			R	C	R	R	R			R		R
	28T-5, 24–25	W		R			R			C		C		R	C	R		+		+		+	+			R	C	R	R	R			R		R
1.46–1.67	28T-CC	M		+			+			R		R			C	R				+		R	R					C	C	R			R		+
	29T-CC	M		R	R	+	+			C		C			C					+		+	R					R	C				+		R
	30T-CC	M		+	+					R		R			C							+	C						C						+
	31X-CC	W		R	+	+	+			R		C			C	C				+			R				C	C	C			+		R	
	32X-CC	M					+			R		R			R								R						C						
	33X-CC	W		+	+	+	+			R		R			C								R						R			r	+		+
	34X-CC	W		+	+	+	+			C		R			C	R							R				+	R	C						R
	35X-CC	M				+	+			R					C	+						+	+		r		C	C	C			r	+		R
	36X-CC	W		R	+	+	+			C		C			C	R						+	R				C	C	C	R		+		R	R

Preservation: P = poor, M = moderate, W = well. Abundance: A = abundant, C = common, R = rare, + = present, r = reworked, ? = questionable.

Table T7. Calcareous nannofossils events and absolute age, Hole C0018A.

Calcareous nannofossil event	Age (Ma)				Core, section, interval (cm)		Depth (mbsf)				Sedimentation rate (cm/k.y.)
	Upper	Lower	Middle	Error	Top	Bottom	Top	Bottom	Middle	Error	
					333-C0018A-	333-C0018A-					
FO *Emiliania huxleyi*	0.291	0.291	0.291	0	2H-CC	3H-CC	16.05	25.55	20.80	4.75	7.15
LO *Pseudoemiliania lacunosa*	0.436	0.436	0.436	0	3H-CC	4H-CC	25.55	35.04	30.29	4.75	6.95
LO *Reticulofenestra asanoi*	0.901	0.905	0.903	0.002	14H-CC	15H-2, 71–72	126.57	127.37	126.97	0.40	20.70
FO *Gephyrocapsa parallela* (sp. 3)	1.04	1.04	1.04	0	16H-CC	17H-CC	144.62	153.23	148.93	4.31	16.03
FO *Reticulofenestra asanoi*	1.078	1.136	1.107	0.029	22H-CC	23H-1, 38–39	187.47	188.30	187.88	0.42	58.14
LO *Gephyrocapsa* spp. (>5.5 µm)	1.24	1.24	1.24	0	24T-4, 129–130	24T-6, 52–53	195.04	197.08	196.06	1.02	6.15
FO *Gephyrocapsa* spp. (>5.5 µm)	1.46	1.46	1.46	0	28T-5, 24–25	28T-CC	233.12	233.56	233.34	0.22	16.94

Age based on Raffi et al. (2006). FO = first occurrence, LO = last occurrence.

Table T8. Paleomagnetic age datums, Site C0018.

Datum	Boundary age (Ma)	Upper		Lower		Average depth (mbsf)	Note
		Core, section, interval (cm)	Depth (mbsf)	Core, section, interval (cm)	Depth (mbsf)		
Magnetic		333-C0018A-		333-C0018A-			
Emperor	0.42	8H-2, 14	64.01	8H-2, 14	64.01	64.01	Uncertain
Brunhes/Matuyama	0.78	14H-3, 18	119.93	14H-7, 93	125.02	122.47	
Jaramillo (bottom)	1.07	24T-1, 1	190.66	24T-5, 59	195.74	193.20	
Cobb Mountain (top)	1.21	25T-2, 28	[201.84]	27T-3, 3	220.96		Upper uncertain because of no recovery in Core 333-C0018A-26T
Cobb Mountain (bottom)	1.24	28T-1, 25	228.90	28T-2, 20	230.26	229.58	
Tephra							
Azuki volcanic ash bed	0.85	14H-8, 14.5	125.65	14H-CC, 11	126.55	126.18	
Pink volcanic ash bed	1.05	23H-1, 68.5	188.57	23H-CC, 6.5	190.51	189.68	

Table T9. Moisture and density results from discrete samples, Site C0018. (Continued on next six pages.)

Core, section, interval (cm)	Depth CSF (m)	Water content (wt%)	Density (g/cm^3)		Porosity (fractional)	Void ratio	Lithologic note
			Bulk	Grain			
333-C0018A-							
1H-1, 27	0.27	0.49	1.41	2.60	0.76	2.38	
1H-1, 73	0.73	0.49	1.41	2.56	0.75	2.50	
1H-2, 21.5	1.01	0.47	1.44	2.59	0.73	2.35	
1H-3, 26	1.28	0.45	1.46	2.55	0.72	2.00	
1H-3, 99	2.01	0.48	1.60	2.72	0.66	2.28	
1H-4, 27	2.70	0.45	1.55	2.67	0.68	2.01	
1H-4, 61	3.04	0.46	1.50	2.49	0.68	2.10	
1H-4, 66	3.09	0.46	1.48	2.37	0.66	1.96	
1H-4, 100	3.43	0.44	1.53	2.65	0.69	1.98	
1H-4, 103	3.46	0.46	1.54	2.57	0.66	2.20	
1H-4, 107	3.50	0.44	1.48	2.48	0.69	1.98	
1H-5, 26	4.10	0.44	1.49	2.45	0.67	2.04	
1H-6, 22	4.73	0.44	1.50	2.51	0.68	1.93	
1H-7, 26	5.00	0.44	1.56	2.66	0.67	2.06	
1H-7, 100	5.74	0.46	1.57	2.71	0.68	2.18	
1H-8, 27.5	6.42	0.47	1.51	2.55	0.68	2.19	
2H-1, 5	6.70	0.55	1.53	2.84	0.72	3.12	
2H-1, 17	6.82	0.54	1.50	2.80	0.73	2.98	
2H-1, 39	7.04	0.46	1.49	2.59	0.70	2.26	
2H-1, 107	7.72	0.43	1.51	2.71	0.71	2.00	
2H-2, 21.5	8.15	0.44	1.53	2.71	0.70	2.02	
2H-3, 26	8.42	0.42	1.51	2.48	0.67	1.88	
2H-4, 26	9.82	0.42	1.49	2.54	0.69	1.84	
2H-4, 102	10.58	0.45	1.52	2.51	0.67	2.06	
2H-5, 24	11.21	0.40	1.56	2.63	0.66	1.77	
2H-6, 21.5	11.72	0.44	1.55	2.62	0.67	2.13	
2H-7, 25	11.98	0.43	1.55	2.55	0.66	1.96	
2H-7, 105	12.78	0.45	1.58	2.71	0.67	2.12	
2H-8, 25	13.39	0.45	1.54	2.66	0.69	2.17	
2H-8, 102	14.16	0.42	1.51	2.58	0.69	1.84	
2H-10, 21.5	15.27	0.41	1.53	2.67	0.69	1.75	
3H-1, 22	16.37	0.41	1.59	2.73	0.67	1.87	
3H-1, 85	17.00	0.43	1.57	2.67	0.67	1.88	
3H-2, 20	17.76	0.33	1.58	2.63	0.65	1.14	
3H-2, 98	18.54	0.45	1.58	2.59	0.65	2.04	
3H-3, 20	19.20	0.49	1.53	2.58	0.67	2.30	
3H-3, 55	19.55	0.47	1.63	2.71	0.64	2.15	
3H-4, 58	20.59	0.48	1.57	2.74	0.68	2.29	
3H-5, 22	21.23	0.41	1.56	2.62	0.66	1.70	
3H-6, 20	21.44	0.38	1.54	2.64	0.68	1.47	
3H-6, 102	22.26	0.38	1.55	2.69	0.68	1.76	
3H-7, 20	22.88	0.41	1.57	2.57	0.65	1.82	
3H-7, 96	23.64	0.51	1.60	2.62	0.64	2.69	
3H-8, 15	24.24	0.42	1.63	2.77	0.65	1.96	
3H-8, 88	24.97	0.41	1.56	2.56	0.65	1.73	
3H-8, 120	25.29	0.37	1.65	2.36	0.53	1.39	
3H-9, 34	25.83	0.43	1.54	2.58	0.67	1.90	
4H-1, 25	25.90	0.42	1.45	2.42	0.70	1.79	
4H-1, 100	26.65	0.43	1.48	2.46	0.68	1.90	
4H-2, 82	27.97	0.43	1.48	2.53	0.70	1.92	
4H-3, 20	28.85	0.35	1.58	2.53	0.63	1.42	
4H-3, 74	29.39	0.45	1.61	2.48	0.60	2.05	
4H-4, 20	29.77	0.44	1.71	2.91	0.64	1.88	
4H-5, 58	30.36	0.31	1.63	2.73	0.65	1.17	
4H-5, 92	30.70	0.43	1.45	2.61	0.73	2.06	
4H-6, 22	31.50	0.45	1.62	2.79	0.66	1.95	
4H-6, 102	32.30	0.42	1.60	2.60	0.63	1.84	
4H-7, 18	32.95	0.41	1.63	2.47	0.58	1.76	
4H-7, 98	33.75	0.42	1.57	2.60	0.66	1.89	
4H-8, 50	34.77	0.42	1.57	2.53	0.64	1.79	
5H-1, 17	35.32	0.35	1.58	2.63	0.65	1.29	
5H-1, 95	36.10	0.36	1.56	2.58	0.66	1.51	
5H-2, 36	36.93	0.48	1.73	2.74	0.59	2.19	Sand/Ash
5H-2, 105	37.62	-0.23	1.54	2.61	0.67	–0.38	
5H-3, 8	38.14	0.35	1.51	2.41	0.65	1.35	
5H-3, 103	39.09	0.46	1.77	2.64	0.54	2.05	Sand/Ash
5H-4, 21.5	39.41	0.31	1.61	2.81	0.67	1.18	

Table T9 (continued). (Continued on next page.)

Core, section, interval (cm)	Depth CSF (m)	Water content (wt%)	Density (g/cm³)		Porosity (fractional)	Void ratio	Lithologic note
			Bulk	Grain			
5H-5, 12	39.54	0.40	1.52	2.48	0.66	1.70	
5H-5, 100	40.42	0.34	1.57	2.58	0.65	1.37	
5H-6, 27	41.09	0.37	1.59	2.59	0.64	1.60	
5H-6, 95	41.77	0.37	1.58	2.64	0.65	1.61	
5H-7, 22	42.55	0.37	1.56	2.53	0.64	1.55	
5H-7, 77	43.10	0.42	1.66	2.48	0.56	1.92	
5H-7, 127	43.60	0.35	1.69	2.69	0.60	1.31	
5H-8, 22	43.98	0.42	2.75	2.10	-0.61	1.77	
5H-8, 76	44.52	0.42	1.68	2.57	0.58	2.07	
6H-1, 2	44.67	0.50	1.63	2.66	0.63	2.52	
6H-1, 16	44.81	0.42	1.74	2.73	0.58	1.94	
6H-1, 39	45.04	0.42	1.69	2.76	0.62	1.85	
5H-CC, 35	45.30	0.45	1.81	2.74	0.54	2.15	
6H-1, 103	45.68	0.40	1.68	2.75	0.62	1.77	
6H-2, 26	46.32	0.40	1.68	2.70	0.61	1.76	
6H-2, 118	47.24	0.37	1.61	2.72	0.66	1.63	
6H-3, 22	47.69	0.47	1.65	2.47	0.57	2.15	Sand/Ash
6H-3, 93	48.40	0.41	1.57	2.53	0.64	1.78	
6H-4, 21	48.86	0.39	1.65	2.95	0.67	1.73	
6H-5, 25	49.12	0.38	1.60	2.66	0.65	1.48	
6H-5, 124.5	50.12	0.35	1.63	2.71	0.64	1.46	
6H-6, 32	50.60	0.39	1.62	2.67	0.64	1.74	
6H-6, 98	51.26	0.38	1.73	2.89	0.62	1.62	
6H-7, 20	51.90	0.39	1.62	2.68	0.64	1.63	
6H-7, 115	52.85	0.39	1.67	2.79	0.63	1.75	
6H-8, 17	53.28	0.37	1.62	2.51	0.60	1.51	
7H-1, 8	54.23	0.40	1.66	2.76	0.63	1.74	
6H-9, 28	54.39	0.33	1.76	2.83	0.59	1.19	
7H-1, 100	55.15	0.41	1.67	2.72	0.62	1.80	
7H-2, 30	55.85	0.36	1.64	2.64	0.62	1.52	
7H-2, 102	56.57	0.38	1.67	2.81	0.64	1.58	
7H-3, 44	57.41	0.37	1.65	2.59	0.60	1.56	
7H-3, 72	57.69	0.37	1.61	2.63	0.63	1.56	
7H-4, 23	58.17	0.38	1.69	2.49	0.54	1.56	
7H-5, 30	58.48	0.39	1.62	2.68	0.64	1.69	
7H-5, 90	59.08	0.35	1.70	2.72	0.60	1.34	
7H-7, 22	59.70	0.40	1.64	2.62	0.61	1.60	
7H-7, 98	60.46	0.38	1.66	2.66	0.61	1.53	
7H-8, 22	60.93	0.39	1.67	2.69	0.61	1.65	
7H-9, 10	61.20	0.40	1.66	2.64	0.61	1.58	
7H-9, 98	62.08	0.40	1.63	2.67	0.63	1.61	
7H-9, 134	62.44	0.37	1.68	2.55	0.57	1.46	
7H-10, 22	62.82	0.38	1.59	2.50	0.62	1.52	
7H-11, 20	63.14	0.41	1.64	2.57	0.61	1.58	
8H-1, 15	63.80	0.36	1.58	2.45	0.61	1.30	
7H-11, 100	63.94	0.41	1.62	2.60	0.62	1.73	
8H-2, 25	64.16	0.43	1.59	2.51	0.62	1.83	
8H-2, 108	64.99	0.43	1.65	2.58	0.59	2.00	
8H-3, 12	65.49	0.42	1.62	2.51	0.60	1.77	
8H-3, 78	66.15	0.42	1.54	2.35	0.61	1.94	
8H-4, 60	67.13	0.41	1.63	2.41	0.57	1.82	
8H-4, 98	67.51	0.39	1.58	2.54	0.63	1.73	
8H-5, 8	67.76	0.41	1.55	2.52	0.65	1.77	
8H-6, 21	68.11	0.60	1.60	2.76	0.67	3.68	
8H-7, 35	68.47	0.40	1.57	2.53	0.64	1.70	
8H-7, 94	69.06	0.40	1.62	2.78	0.66	1.65	
8H-8, 102	70.34	0.42	1.63	2.74	0.65	1.74	
8H-9, 37	71.16	0.39	1.66	2.76	0.63	1.69	
8H-9, 72	71.51	0.38	1.58	2.57	0.64	1.63	
8H-9, 115.5	71.95	0.40	1.35	2.54	0.79	1.72	
8H-10, 44	72.72	0.42	1.63	2.65	0.63	1.97	
8H-10, 124	73.52	0.41	1.61	2.58	0.62	1.69	
9H-1, 75	73.90	0.40	1.55	2.45	0.64	1.64	
9H-2, 13	74.32	0.42	1.65	2.70	0.63	1.81	
9H-2, 78	74.97	0.43	1.67	2.71	0.62	1.98	
9H-3, 23	75.92	0.42	1.62	2.64	0.63	1.90	
9H-3, 109	76.78	0.43	1.61	2.75	0.66	1.77	
9H-4, 22.5	77.32	0.42	1.55	2.45	0.63	1.96	
9H-4, 93	78.03	0.41	1.58	2.48	0.62	1.83	

Table T9 (continued). (Continued on next page.)

Core, section, interval (cm)	Depth CSF (m)	Water content (wt%)	Density (g/cm^3)		Porosity (fractional)	Void ratio	Lithologic note
			Bulk	Grain			
9H-5, 26.5	78.78	0.39	1.57	2.55	0.64	1.74	
9H-6, 27	79.50	0.37	1.58	2.69	0.66	1.53	
10H-1, 17	80.32	0.34	1.60	2.70	0.66	1.25	
10H-2, 27	80.95	0.42	1.53	2.42	0.64	1.89	
10H-2, 87	81.55	0.37	1.62	2.79	0.66	1.52	
10H-3, 21	82.30	0.37	1.61	2.69	0.65	1.53	
10H-3, 88	82.97	0.38	1.68	2.82	0.64	1.64	
10H-4, 21	83.75	0.38	1.66	2.64	0.61	1.66	
10H-5, 10	83.86	0.35	1.68	2.49	0.55	1.51	
10H-5, 71	84.47	0.38	1.61	2.72	0.65	1.65	
10H-6, 41	85.57	0.37	1.66	2.63	0.60	1.55	
10H-6, 106	86.22	0.38	1.68	2.67	0.60	1.64	
10H-7, 22.5	86.80	0.39	1.66	2.71	0.62	1.59	
10H-7, 46	87.03	0.34	1.70	2.82	0.62	1.33	
10H-7, 63	87.20	0.37	1.74	2.83	0.60	1.49	
10H-8, 34	88.37	0.37	1.68	2.77	0.62	1.52	
10H-8, 131	89.34	0.36	1.68	2.69	0.61	1.50	
10H-9, 11	89.56	0.35	1.66	2.72	0.62	1.39	
10H-9, 26	89.71	0.39	1.63	2.60	0.61	1.54	
11H-1, 14	89.79	0.33	1.66	2.60	0.60	1.20	
10H-9, 87	90.32	0.34	1.71	2.62	0.57	1.44	
11H-2, 18.5	90.48	0.32	1.69	2.69	0.60	1.24	
11H-2, 116	91.46	0.33	1.68	2.68	0.60	1.26	
11H-3, 31	91.97	0.25	1.68	2.58	0.58	0.87	
11H-3, 116	92.82	0.38	1.60	2.48	0.61	1.62	
11H-4, 28	93.35	0.36	1.70	2.51	0.55	1.47	
11H-5, 13	94.02	0.28	1.76	2.82	0.59	0.99	
11H-6, 30	94.41	0.39	1.78	2.72	0.55	1.70	
11H-6, 88	94.99	0.37	1.72	2.60	0.56	1.60	
11H-7, 36	95.88	0.39	1.90	2.66	0.47	1.64	
11H-7, 86	96.38	0.36	1.66	2.70	0.62	1.44	
11H-8, 24	97.16	0.35	1.69	2.66	0.60	1.43	
11H-8, 74	97.66	0.36	1.84	2.65	0.50	1.52	
11H-8, 94	97.86	0.36	1.66	2.73	0.63	1.50	
11H-10, 33	98.69	0.37	1.69	2.76	0.62	1.52	
11H-10, 61	98.97	0.37	1.62	2.59	0.62	1.52	
12H-1, 26	99.41	0.36	1.72	2.73	0.59	1.50	
11H-11, 18.5	99.92	0.38	1.67	2.59	0.59	1.55	
12H-2, 30	100.13	0.39	1.70	2.72	0.60	1.73	
12H-2, 115	100.98	0.39	1.73	2.78	0.60	1.64	
12H-3, 28	101.35	0.37	1.65	2.61	0.60	1.55	
12H-3, 100	102.07	0.37	1.68	2.68	0.60	1.54	
12H-4, 14	102.62	0.37	1.69	2.69	0.60	1.50	
12H-4, 68	103.16	0.38	1.62	2.55	0.61	1.58	
12H-5, 21.5	103.90	0.40	1.66	2.76	0.63	1.72	
12H-6, 29	104.20	0.38	1.65	2.67	0.62	1.59	
12H-6, 130	105.21	0.36	1.67	2.68	0.61	1.41	
12H-7, 44	105.76	0.36	1.69	2.70	0.61	1.46	
12H-7, 132	106.64	0.37	1.67	2.65	0.60	1.60	
12H-8, 53	107.27	0.36	1.64	2.62	0.61	1.41	
12H-8, 120.5	107.94	0.36	1.64	2.69	0.63	1.44	
12H-9, 20	108.35	0.35	1.66	2.66	0.61	1.35	
12H-9, 42	108.57	0.36	1.69	2.61	0.58	1.44	
13H-1, 10	108.75	0.35	1.70	2.68	0.59	1.42	
13H-3, 100	110.27	0.32	1.69	2.76	0.62	1.19	
13H-4, 67	111.34	0.33	1.65	2.52	0.58	1.26	
13H-4, 125.5	111.92	0.34	1.69	2.64	0.59	1.27	
13H-5, 27	112.35	0.32	1.69	2.58	0.57	1.17	
13H-5, 108.5	113.17	0.32	1.69	2.65	0.59	1.24	
13H-6, 22	113.50	0.34	1.69	2.65	0.59	1.39	
13H-6, 22	113.50	0.38	1.75	2.61	0.54	1.66	
13H-7, 10	113.61	0.37	1.71	2.57	0.56	1.46	
13H-9, 67	115.10	0.37	1.67	2.49	0.56	1.59	
13H-9, 122	115.65	0.35	1.75	2.60	0.54	1.40	
13H-10, 18	116.00	0.38	1.75	2.64	0.55	1.49	
13H-10, 88	116.70	0.32	1.74	2.74	0.58	1.23	
13H-12, 13	117.85	0.33	1.66	2.73	0.62	1.32	
14H-1, 8	118.23	0.33	1.61	2.48	0.60	1.22	
13H-13, 54	118.49	0.33	1.64	2.55	0.59	1.35	

Table T9 (continued). (Continued on next page.)

Core, section, interval (cm)	Depth CSF (m)	Water content (wt%)	Density (g/cm³)		Porosity (fractional)	Void ratio	Lithologic note
			Bulk	Grain			
14H-2, 73.5	119.09	0.36	1.75	2.64	0.55	1.52	
13H-13, 120	119.15	0.37	1.71	2.80	0.61	1.48	
14H-2, 128.5	119.64	0.35	1.77	2.75	0.57	1.42	
13H-14, 30	119.65	0.37	1.69	2.62	0.58	1.55	
14H-3, 25	120.00	0.39	1.73	2.59	0.55	1.55	
14H-3, 117	120.92	0.34	1.77	2.77	0.57	1.30	
14H-4, 16	121.34	0.38	1.70	2.72	0.60	1.63	
14H-4, 20	121.38	0.17	1.64	2.56	0.60	0.52	
14H-5, 21.5	122.65	0.38	1.69	2.65	0.59	1.42	
14H-6, 15	122.81	0.38	1.68	2.70	0.61	1.42	
14H-6, 72.5	123.38	0.33	1.62	2.53	0.61	1.29	
14H-6, 128	123.94	0.36	1.71	2.60	0.57	1.34	
14H-7, 21	124.31	0.26	1.67	2.73	0.62	0.92	
14H-7, 43	124.53	0.44	2.07	2.61	0.34	2.03	Sand/Ash
14H-8, 10	125.61	0.34	1.59	2.39	0.59	1.33	
14H-8, 68	126.19	0.44	1.59	2.38	0.59	2.09	Sand/Ash
15H-2, 17	126.93	0.34	1.72	2.62	0.56	1.34	
15H-2, 65	127.41	0.46	1.64	2.47	0.57	2.15	Sand/Ash
15H-2, 85	127.61	0.30	1.89	2.69	0.48	1.11	
15H-3, 21	128.15	0.31	1.73	2.68	0.57	1.20	
15H-3, 33	128.27	0.33	1.74	2.69	0.57	1.33	
15H-3, 86	128.80	0.32	1.81	2.68	0.53	1.22	
15H-4, 86	130.22	0.30	1.79	2.71	0.54	1.09	
15H-4, 92	130.28	0.30	1.75	2.72	0.57	1.06	
15H-5, 22	130.78	0.28	1.76	2.66	0.55	1.04	
15H-6, 13	130.92	0.27	1.77	2.58	0.52	0.93	
15H-6, 78	131.57	0.28	1.77	2.57	0.52	1.05	
15H-7, 27	132.51	0.28	1.88	2.77	0.51	1.03	
15H-7, 80	133.04	0.36	1.83	2.58	0.48	1.44	
15H-7, 99	133.23	0.34	1.84	2.71	0.51	1.40	
15H-8, 18	133.86	0.29	1.83	2.66	0.51	1.11	
15H-8, 98	134.66	0.35	1.70	2.67	0.59	1.41	
15H-9, 31	135.42	0.36	1.77	2.81	0.58	1.54	
15H-9, 111	136.22	0.34	1.83	2.74	0.53	1.32	
16H-2, 14	137.78	0.29	1.70	2.65	0.58	1.10	
16H-2, 60	138.24	0.29	1.70	2.75	0.61	1.08	
16H-2, 90	138.54	0.32	1.71	2.61	0.57	1.25	
16H-3, 7	139.21	0.30	1.84	2.73	0.52	1.13	
16H-3, 66	139.80	0.38	1.82	2.68	0.52	1.59	
16H-4, 37	140.62	0.40	1.78	2.72	0.56	1.74	
16H-4, 98	141.23	0.39	1.84	2.76	0.53	1.64	
16H-10, 32	142.06	0.38	1.65	2.64	0.61	1.73	
16H-11, 12	142.64	0.36	1.64	2.71	0.63	1.50	
16H-11, 28	142.80	0.35	1.62	2.61	0.62	1.46	
16H-11, 122	143.74	0.27	1.71	2.89	0.63	1.08	
16H-12, 25	144.19	0.28	1.72	2.76	0.60	1.05	
16H-13, 10	144.30	0.28	1.71	2.71	0.59	1.01	
17H-1, 50	145.15	0.33	1.94	2.93	0.52	1.33	
17H-1, 118	145.83	0.31	1.89	2.80	0.51	1.12	
17H-2, 7	146.13	0.34	1.87	2.71	0.50	1.35	
17H-2, 39	146.45	0.33	1.77	2.75	0.57	1.24	
17H-3, 40	147.86	0.32	1.76	2.58	0.53	1.28	
17H-3, 110	148.56	0.24	1.73	2.67	0.57	0.80	
17H-3, 138	148.84	0.32	1.70	2.54	0.55	1.26	
17H-4, 48	149.36	0.32	1.78	2.75	0.56	1.38	
17H-5, 26	149.80	0.30	1.93	2.65	0.45	1.08	
17H-6, 8	149.89	0.33	1.80	2.79	0.56	1.36	
17H-6, 19	150.00	0.32	1.83	2.95	0.58	1.18	
17H-6, 108	150.89	0.30	1.80	2.63	0.52	1.13	
17H-7, 3	151.26	0.28	1.79	2.84	0.58	1.00	
17H-7, 88	152.11	0.42	1.75	2.60	0.54	2.08	
17H-8, 10	152.75	0.27	1.81	2.70	0.53	0.96	
17H-8, 72	153.37	0.28	1.82	2.61	0.50	1.03	
18H-1, 10	153.75	0.31	1.65	2.96	0.68	1.20	
18H-1, 93	154.58	0.30	1.88	2.70	0.49	1.12	
18H-2, 8	155.01	0.32	1.87	2.75	0.51	1.23	
18H-2, 110	156.03	0.28	1.81	2.75	0.55	1.03	
18H-3, 11.5	156.53	0.30	1.81	2.70	0.53	1.07	
18H-3, 34	156.75	0.24	1.77	2.68	0.55	0.82	

Table T9 (continued). (Continued on next page.)

Core, section, interval (cm)	Depth CSF (m)	Water content (wt%)	Density (g/cm³)		Porosity (fractional)	Void ratio	Lithologic note
			Bulk	Grain			
18H-3, 104	157.45	0.27	1.84	2.67	0.51	0.97	
18H-4, 27.5	158.22	0.29	1.79	2.61	0.52	1.07	
18H-5, 6	158.29	0.29	1.94	2.69	0.45	1.10	
18H-5, 64	158.87	0.35	1.90	2.76	0.49	1.36	
18H-5, 98.5	159.22	0.30	1.83	2.69	0.52	1.01	
18H-6, 13	159.51	0.32	1.83	2.71	0.52	1.21	
19H-1, 8	159.73	0.31	1.70	2.61	0.58	1.13	
19H-1, 86	160.51	0.34	1.74	2.47	0.50	1.25	
19H-1, 121.5	160.87	0.34	1.75	2.64	0.55	1.35	
19H-2, 40	161.43	0.31	1.76	2.59	0.53	1.12	
19H-2, 107	162.10	0.30	1.68	2.49	0.55	1.18	
19H-3, 8	162.52	0.27	1.72	2.67	0.57	0.92	
19H-3, 46.5	162.91	0.26	1.77	2.61	0.53	0.93	
19H-4, 26.5	163.33	0.32	1.84	2.81	0.54	1.21	
19H-5, 41	163.75	0.25	1.83	2.56	0.48	0.90	
19H-6, 18	164.85	0.30	1.89	2.69	0.48	1.06	
20H-1, 20	164.85	0.29	1.75	2.63	0.55	1.03	
20H-2, 105	166.01	0.32	1.92	2.73	0.47	1.22	
20H-3, 22	166.47	0.31	1.78	2.59	0.51	1.21	
20H-3, 75	167.00	0.26	1.79	2.59	0.51	0.91	
20H-3, 123.5	167.49	0.30	1.78	2.70	0.55	1.13	
20H-4, 18	167.87	0.32	1.80	2.74	0.55	1.25	
20H-4, 93	168.62	0.30	1.85	2.61	0.48	1.08	
20H-5, 21	169.09	0.30	1.82	2.71	0.53	1.11	
20H-6, 29	169.39	0.29	1.78	2.73	0.56	1.02	
20H-6, 125	170.35	0.30	1.76	2.54	0.52	1.09	
20H-7, 87	171.43	0.29	1.80	2.66	0.53	1.06	
20H-7, 129.5	171.86	0.29	1.79	2.57	0.50	1.03	
20H-8, 22	172.24	0.29	1.80	2.64	0.52	1.08	
20H-8, 64	172.66	0.32	1.79	2.61	0.52	1.21	
20H-8, 119	173.21	0.33	1.76	2.52	0.51	1.31	
20H-9, 22	173.63	0.32	1.81	2.66	0.52	1.21	
21H-1, 27	174.42	0.28	1.74	2.61	0.55	1.02	
21H-1, 99	175.14	0.28	1.79	2.78	0.57	0.99	
21H-2, 11	175.67	0.24	1.78	2.69	0.55	0.81	
21H-2, 100	176.56	0.20	1.88	2.74	0.50	0.69	
21H-3, 20	176.96	0.26	1.84	2.65	0.50	0.96	
21H-4, 20	177.17	0.28	1.90	2.61	0.45	1.06	
21H-5, 10	177.31	0.30	2.04	2.75	0.41	1.10	
21H-5, 70	177.91	0.28	1.90	2.74	0.49	1.05	
22H-1, 21	178.66	0.28	1.90	2.83	0.52	1.03	
22H-2, 15	179.06	0.29	1.81	2.69	0.52	1.06	
22H-2, 35	179.26	0.28	1.85	2.72	0.51	1.04	
22H-2, 52	179.43	0.26	1.87	2.74	0.51	0.93	
22H-2, 110	180.01	0.30	1.84	2.70	0.52	1.14	
22H-3, 8	180.23	0.25	1.83	2.67	0.51	0.91	
22H-4, 5	180.78	0.27	1.91	2.72	0.48	1.00	
22H-5, 30	181.35	0.25	1.81	2.71	0.53	0.88	
22H-6, 34	181.70	0.26	1.92	2.73	0.48	0.93	
22H-7, 55	182.39	0.26	1.88	2.75	0.50	0.89	
22H-7, 84	182.68	0.25	1.90	2.67	0.47	0.83	
22H-8, 6	183.30	0.25	1.88	2.67	0.48	0.85	
22H-9, 28	184.09	0.25	1.88	2.64	0.47	0.87	
22H-10, 38	185.19	0.29	1.88	2.58	0.45	1.06	
22H-11, 55	186.01	0.23	1.88	2.61	0.46	0.79	
22H-12, 44	186.90	0.26	1.91	2.68	0.46	0.92	
23H-1, 47	188.42	0.31	1.83	2.68	0.52	1.12	
24T-1, 36	191.01	0.25	1.93	2.65	0.44	0.88	
24T-1, 42	191.07	0.33	1.86	2.62	0.48	1.28	
24T-1, 48	191.13	0.29	1.76	2.59	0.53	1.03	
24T-1, 128	191.93	0.32	1.88	2.63	0.47	1.28	
24T-2, 20	192.26	0.31	1.75	2.68	0.56	1.09	
24T-2, 38	192.44	0.30	1.80	2.60	0.51	1.15	
24T-2, 102	193.08	0.30	1.77	2.73	0.56	1.06	
24T-2, 122	193.28	0.32	1.75	2.53	0.52	1.18	
24T-3, 27	193.74	0.34	1.80	2.69	0.53	1.23	
24T-4, 30	194.05	0.28	1.76	2.53	0.51	1.05	
24T-4, 120	194.95	0.27	1.72	2.55	0.54	0.94	
24T-5, 23	195.38	0.23	1.68	2.50	0.55	0.77	

Table T9 (continued). (Continued on next page.)

Core, section, interval (cm)	Depth CSF (m)	Water content (wt%)	Density (g/cm³)		Porosity (fractional)	Void ratio	Lithologic note
			Bulk	Grain			
24T-5, 114	196.29	0.28	1.87	2.76	0.51	1.01	
24T-5, 134	196.49	0.30	1.84	2.62	0.49	1.10	
24T-6, 36	196.92	0.28	1.90	2.58	0.44	1.00	
25T-1, 30	200.45	0.25	1.83	2.64	0.50	0.85	
25T-1, 94	201.09	0.23	1.80	2.65	0.52	0.78	
25T-2, 30	201.86	0.23	1.80	2.57	0.50	0.75	
25T-2, 79	202.35	0.52	1.86	2.56	0.46	2.76	Sand/Ash
27T-1, 16	219.31	0.22	1.95	2.68	0.44	0.74	
27T-2, 11	219.57	0.28	1.95	2.64	0.43	0.99	
27T-2, 52	219.98	0.26	1.96	2.64	0.42	0.91	
27T-2, 117	220.63	0.26	1.84	2.64	0.50	0.88	
27T-3, 44	221.37	0.24	1.90	2.70	0.48	0.81	
27T-3, 64	221.57	0.31	1.85	2.58	0.47	1.19	
27T-3, 111	222.04	0.25	1.93	2.66	0.45	0.84	
27T-3, 116	222.09	0.20	1.79	2.70	0.54	0.64	
27T-4, 14	222.45	0.23	1.89	2.62	0.46	0.78	
27T-4, 66	222.97	0.25	2.05	2.71	0.39	0.91	
27T-4, 74	223.05	0.25	1.97	2.71	0.44	0.87	
27T-5, 24	223.66	0.28	1.92	2.72	0.48	1.02	
27T-6, 14	223.81	0.25	1.92	2.70	0.47	0.83	
27T-6, 85	224.52	0.23	1.84	2.68	0.51	0.79	
27T-7, 23	225.15	0.22	1.87	2.57	0.45	0.72	
27T-7, 67	225.59	0.27	1.94	2.66	0.44	0.97	
27T-8, 20	226.52	0.28	1.93	2.58	0.42	1.01	
27T-8, 30	226.62	0.26	1.87	2.69	0.49	0.90	
27T-8, 80	227.12	0.28	1.85	2.68	0.50	0.99	
28T-1, 54	229.19	0.27	1.86	2.61	0.47	0.97	
28T-1, 110	229.75	0.27	1.80	2.56	0.50	0.92	
28T-2, 23	230.29	0.30	1.87	2.68	0.49	1.12	
28T-2, 100	231.06	0.27	1.81	2.54	0.48	0.98	
28T-3, 10	231.57	0.27	1.83	2.72	0.53	1.01	
28T-3, 43	231.90	0.26	1.86	2.69	0.49	0.96	
28T-3, 75	232.22	0.22	1.88	2.74	0.50	0.74	
28T-3, 105	232.52	0.21	1.92	2.78	0.49	0.67	
28T-4, 26	232.87	0.28	1.98	2.69	0.42	1.04	
28T-5, 16	233.04	0.22	2.01	2.67	0.40	0.75	
29T-1, 29	238.44	0.22	1.83	2.67	0.51	0.73	
29T-1, 68	238.83	0.26	1.99	2.70	0.43	0.92	
29T-1, 92	239.07	0.22	1.96	2.65	0.42	0.73	
29T-2, 15	239.69	0.26	1.91	2.73	0.48	0.90	
29T-3, 27	240.34	0.18	1.99	2.68	0.42	0.59	
29T-3, 84	240.91	0.27	1.85	2.60	0.47	0.93	
29T-4, 10	241.58	0.26	2.07	2.69	0.37	0.92	
29T-4, 52	242.00	0.28	1.86	2.63	0.48	1.01	
29T-4, 79	242.27	0.26	1.89	2.69	0.48	0.94	
29T-4, 127	242.75	0.27	1.84	2.67	0.50	1.01	
29T-5, 22	243.08	0.22	1.92	2.77	0.49	0.74	
29T-5, 43	243.29	0.22	1.91	2.80	0.50	0.72	
29T-5, 72	243.58	0.21	1.96	2.65	0.43	0.67	
29T-6, 30	244.05	0.23	1.96	2.63	0.42	0.78	
29T-7, 5	244.11	0.23	1.98	2.62	0.40	0.82	
30T-1, 25	247.90	0.22	1.98	2.72	0.44	0.76	
30T-1, 95	248.60	0.25	1.96	2.73	0.45	0.85	
30T-2, 22	249.29	0.28	1.98	2.71	0.43	1.00	
30T-2, 104	250.11	0.30	1.91	2.67	0.46	1.08	
31X-1, 40	257.55	0.25	1.84	2.65	0.50	0.91	
31X-1, 103	258.18	0.23	1.78	2.60	0.52	0.77	
31X-2, 78	259.11	0.26	1.93	2.75	0.48	0.93	
31X-2, 105.5	259.38	0.24	1.96	2.68	0.43	0.82	
31X-3, 61	260.15	0.30	1.88	2.67	0.48	1.08	
31X-4, 31.5	260.84	0.27	1.90	2.61	0.45	0.95	
31X-5, 14	260.99	0.29	1.79	2.62	0.52	1.14	
31X-5, 62	261.47	0.26	1.87	2.67	0.49	0.95	
31X-5, 120	262.05	0.22	1.85	2.78	0.53	0.77	
31X-6, 20	262.50	0.29	1.89	2.71	0.49	1.09	
31X-6, 69	262.99	0.48	2.01	2.77	0.43	2.61	Sand/Ash
31X-6, 138	263.68	0.30	1.84	2.73	0.52	1.14	
32X-1, 38	267.03	0.31	1.79	2.67	0.53	1.20	
32X-1, 98	267.63	0.24	1.83	2.80	0.55	0.85	

Table T9 (continued).

Core, section, interval (cm)	Depth CSF (m)	Water content (wt%)	Density (g/cm^3)		Porosity (fractional)	Void ratio	Lithologic note
			Bulk	Grain			
32X-2, 17	268.23	0.27	1.95	2.75	0.46	0.96	
32X-2, 58	268.64	0.24	1.87	2.69	0.49	0.83	
32X-2, 130	269.36	0.25	1.90	2.62	0.45	0.90	
32X-3, 124	270.71	0.27	1.92	2.72	0.47	0.96	
32X-4, 44	271.32	0.23	1.85	2.65	0.49	0.80	
32X-4, 121	272.09	0.24	1.94	2.68	0.44	0.82	
32X-5, 34	272.62	0.26	1.94	2.68	0.45	0.94	
32X-5, 114	273.42	0.25	1.91	2.75	0.49	0.86	
32X-6, 12	273.81	0.28	1.92	2.70	0.46	1.06	
33X-1, 42	276.57	0.24	1.88	2.79	0.51	0.84	
33X-2, 102	278.58	0.25	1.92	2.68	0.46	0.88	
33X-3, 21	278.87	0.30	1.89	2.65	0.47	1.07	
33X-4, 86	279.79	0.25	1.78	2.58	0.52	0.89	
33X-5, 17	280.10	0.24	1.91	2.71	0.47	0.82	
33X-5, 54	280.47	0.24	1.89	2.60	0.45	0.80	
33X-6, 25.5	281.28	0.25	1.89	2.59	0.44	0.89	
33X-7, 31	281.60	0.23	1.96	2.79	0.47	0.77	
33X-7, 88	282.17	0.27	1.98	2.72	0.44	1.01	
33X-8, 37	282.60	0.16	1.89	2.77	0.50	0.50	
33X-9, 36	283.13	0.26	2.14	2.70	0.33	0.96	
34X-1, 30	285.95	0.26	1.91	2.76	0.49	0.94	
34X-1, 83	286.48	0.25	1.88	2.69	0.48	0.86	
34X-2, 10	287.25	0.50	1.88	2.62	0.46	2.69	Sand/Ash
34X-2, 19	287.34	0.27	1.94	2.85	0.50	1.01	
34X-2, 62	287.77	0.23	1.94	2.63	0.43	0.76	
34X-3, 22	288.52	0.24	1.92	2.64	0.45	0.81	
34X-4, 31	288.99	0.26	1.91	2.75	0.49	0.95	
34X-5, 31	289.84	0.25	1.90	2.66	0.47	0.88	
34X-6, 24	290.17	0.22	2.00	2.72	0.43	0.74	
34X-7, 20	290.38	0.25	1.94	2.77	0.48	0.91	
34X-7, 83	291.01	0.26	1.91	2.73	0.48	0.92	
34X-8, 16	291.26	0.26	1.95	2.82	0.49	0.95	
34X-9, 24	292.20	0.27	1.88	2.69	0.49	0.96	
34X-9, 72	292.68	0.25	1.85	2.56	0.46	0.85	
35X-1, 66	295.81	0.26	1.91	2.72	0.48	0.91	
35X-2, 49	296.75	0.25	1.87	2.56	0.45	0.82	
35X-3, 31	297.95	0.25	1.94	2.76	0.47	0.90	
35X-4, 21.5	298.51	0.27	1.86	2.67	0.49	0.98	
35X-5, 9	298.61	0.22	1.96	2.65	0.43	0.75	
35X-6, 25	298.99	0.22	1.98	2.68	0.42	0.74	
35X-6, 99	299.73	0.31	1.79	2.72	0.55	1.21	
35X-7, 20	300.32	0.24	1.92	2.63	0.44	0.80	
35X-7, 104	301.16	0.21	1.99	2.69	0.42	0.71	
35X-9, 21	302.74	0.24	1.93	2.70	0.46	0.84	
36X-2, 63	305.55	0.29	1.84	2.75	0.53	1.12	
36X-3, 85	306.62	0.25	1.91	2.68	0.47	0.88	
36X-4, 34.5	307.19	0.30	1.79	2.64	0.53	1.13	
36X-4, 92	307.77	0.31	1.82	2.77	0.54	1.19	
36X-4, 110	307.95	0.28	1.86	2.69	0.50	1.01	
36X-5, 24	308.43	0.24	1.91	2.61	0.44	0.79	
36X-6, 22	308.66	0.21	2.01	2.73	0.42	0.73	
36X-6, 63	309.07	0.31	1.80	2.70	0.54	1.16	
36X-7, 32	309.92	0.28	1.83	2.62	0.49	0.97	
36X-7, 65	310.25	0.25	1.92	2.69	0.46	0.87	
36X-8, 52	311.29	0.22	1.98	2.71	0.43	0.76	
36X-8, 71	311.48	0.27	1.88	2.71	0.50	0.98	

Table T10. Electrical resistivity results from discrete samples determined from impedance, Hole C0018A. (Continued on next page.)

Core, section interval (cm)	Depth CSF (m)	Resistivity (Ωm)
333-C0018A-		
1H-1, 22	0.22	0.351
1H-1, 68	0.68	0.412
1H-3, 29	1.31	0.423
1H-3, 102	2.04	0.650
1H-4, 28	2.71	0.518
1H-4, 98	3.41	0.485
1H-5, 29	4.13	0.477
1H-7, 29	5.03	0.505
1H-7, 97	5.71	0.573
2H-1, 38	7.03	0.418
2H-1, 105	7.70	0.431
2H-3, 16	8.32	0.480
2H-3, 94	9.10	0.507
2H-4, 23	9.79	0.560
2H-4, 109	10.65	0.500
2H-5, 23	11.20	0.505
2H-7, 28	12.01	0.532
2H-7, 101	12.74	0.602
2H-8, 24	13.38	0.537
2H-8, 96	14.10	0.486
2H-9, 13	14.68	0.592
2H-11, 37	15.65	0.662
3H-1, 92	17.07	0.529
3H-2, 94.5	18.51	0.565
3H-3, 53.5	19.53	0.693
3H-4, 55	20.56	0.666
3H-6, 102	22.26	0.595
3H-7, 93	23.61	0.635
3H-8, 82	24.91	0.619
3H-9, 33.5	25.83	0.619
4H-1, 103.5	26.69	0.784
4H-2, 86.5	28.02	0.579
4H-3, 23	28.88	0.616
4H-5, 95	30.73	0.655
4H-6, 109.5	32.38	0.735
4H-7, 96.5	33.74	0.783
4H-8, 49	34.76	0.742
5H-1, 17	35.32	0.628
5H-1, 100	36.15	0.645
5H-2, 34	36.91	0.816
5H-2, 85	37.42	0.690
5H-3, 5	38.11	0.708
5H-3, 108	39.14	1.028
5H-5, 14	39.56	0.652
5H-5, 106	40.48	0.651
5H-6, 32	41.14	0.551
5H-6, 95	41.77	0.666
5H-7, 25	42.58	0.703
5H-7, 83	43.16	0.934
5H-8, 26	44.02	0.930
5H-8, 82	44.58	0.826
6H-1, 44	45.09	0.929
6H-1, 105	45.70	0.718
6H-2, 23	46.29	0.827
6H-2, 122	47.28	0.930
6H-3, 21	47.68	0.775
6H-3, 95	48.42	0.745
6H-5, 24	49.11	0.749
6H-5, 100	49.87	0.803
6H-6, 30	50.58	0.879
6H-6, 100	51.28	0.898
6H-7, 24	51.94	0.809
6H-7, 81	52.51	1.112
6H-8, 20	53.31	0.784
6H-9, 24	54.35	0.885
7H-1, 97	55.12	0.656
7H-2, 34	55.89	0.659
7H-2, 100	56.55	0.694
7H-3, 70	57.67	0.656
7H-5, 26.5	58.45	0.682
7H-5, 87	59.05	0.720
7H-7, 19	59.67	0.817
7H-7, 96	60.44	0.818
7H-8, 21	60.92	0.697
7H-9, 96.5	62.07	0.826
7H-10, 20	62.80	0.724
7H-11, 132	63.84	0.795
8H-1, 19	64.20	0.652
8H-2, 29	64.26	0.716
8H-2, 114.5	65.05	0.803
8H-3, 18	65.55	0.789
8H-3, 81	66.18	0.892
8H-4, 97	67.50	0.668
8H-5, 12.5	67.81	0.608
8H-7, 32.5	68.45	0.646
8H-7, 91.5	69.04	0.663
8H-8, 44	69.76	0.681
8H-8, 108	70.40	0.717
8H-9, 70	71.49	0.703
8H-10, 52	72.80	0.696
8H-10, 131	73.59	0.724
9H-1, 72	73.87	0.620
9H-2, 14	74.33	0.887
9H-2, 80	74.99	0.794
9H-3, 28	75.97	0.751
9H-3, 108	76.77	0.711
9H-4, 25	77.35	0.955
9H-4, 98	78.08	0.669
9H-5, 22	78.73	0.663
9H-6, 29	79.52	0.638
10H-1, 22	80.37	0.779
10H-2, 28	80.96	0.637
10H-2, 88	81.56	0.882
10H-3, 24	82.33	0.667
10H-3, 88	82.97	0.755
10H-5, 10	83.86	0.885
10H-5, 70	84.46	0.689
10H-6, 46	85.62	0.790
10H-6, 105	86.21	1.162
10H-7, 23	86.80	0.699
10H-7, 103	87.60	0.844
10H-8, 34	88.37	0.949
10H-8, 131	89.34	1.019
10H-9, 22	89.67	0.772
10H-9, 100	89.77	0.747
11H-1, 12	90.45	0.782
11H-2, 23	90.53	0.770
11H-2, 122	91.52	1.102
11H-3, 30	91.96	0.921
11H-3, 122	92.88	1.400
11H-4, 34	93.41	0.840
11H-5, 17	94.06	0.817
11H-6, 36.5	94.47	0.851
11H-6, 91	95.02	0.841
11H-7, 42.5	95.94	0.729
11H-7, 89	96.41	0.813
11H-8, 30	97.22	0.784
11H-10, 39.5	98.75	0.817
12H-1, 31	99.46	0.789
12H-2, 36	100.19	0.721
12H-2, 117.5	101.01	0.850
12H-3, 26	101.33	0.750
12H-3, 101	102.08	0.744
12H-4, 18	102.66	0.726
12H-6, 33	104.24	0.728
12H-6, 132	105.23	0.833
12H-7, 50	105.82	0.714
12H-7, 129.5	106.62	0.907
12H-8, 51	107.25	0.831
12H-9, 48	108.63	0.722
13H-1, 15	108.80	0.644
13H-3, 105	110.32	0.741
13H-3, 119.5	110.46	0.713
13H-4, 71	111.38	0.720
13H-5, 26	112.34	0.781
13H-7, 9	113.60	1.019
13H-9, 65	115.08	0.832
13H-9, 120.5	115.63	1.048
13H-10, 24	116.06	0.985
13H-10, 92	116.74	1.076
13H-12, 12	117.84	0.784
13H-13, 58	118.29	1.057
13H-13, 125	118.53	0.901
13H-14, 36.5	119.05	0.734
14H-1, 13.5	119.20	0.763
14H-2, 69	119.68	0.826
14H-2, 132	119.72	1.001
14H-3, 27	120.02	0.910
14H-3, 120	120.95	0.875
14H-4, 16	121.34	0.856
14H-6, 15	122.81	0.859
14H-6, 71	123.37	1.159
14H-7, 22	124.32	0.770
14H-7, 45	124.55	–3.486
14H-8, 10	125.61	0.682
14H-8, 68	126.19	–0.509
15H-2, 22	126.98	0.926
15H-2, 85	127.61	0.665
15H-3, 18	128.12	0.807
15H-3, 86	128.80	0.923
15H-4, 26	129.62	1.185
15H-4, 88	130.24	1.162
15H-6, 12	130.91	0.973
15H-6, 83	131.62	1.021
15H-7, 32	132.56	1.215
15H-7, 103	133.27	1.692
15H-8, 23	133.91	1.136
15H-8, 103	134.71	1.026
15H-9, 31	135.42	1.091
15H-9, 110	136.21	1.026
16H-1, 60	136.75	1.406
16H-1, 100	137.15	0.688
16H-2, 15	137.79	1.062
16H-2, 93	138.57	1.260
16H-3, 10	139.24	1.284
16H-3, 70	139.84	1.569
16H-4, 39	140.64	3.335
16H-4, 103	141.28	1.199
16H-10, 28	142.02	0.962
16H-11, 33	142.85	1.098
16H-13, 13	144.33	1.160
17H-1, 116	145.81	1.042
17H-2, 4	146.10	1.082
17H-2, 113	147.19	1.112
17H-3, 38	147.84	1.098
17H-3, 135	148.81	1.288
17H-4, 46	149.34	1.536
17H-6, 6.5	149.87	1.201
17H-6, 106.5	150.87	1.189
17H-7, 7	151.30	1.232

Table T10 (continued).

Core, section interval (cm)	Depth CSF (m)	Resistivity (Ωm)
17H-7, 87	152.10	1.047
17H-8, 12	152.77	1.260
17H-8, 75.5	153.40	1.588
18H-1, 92	154.57	1.078
18H-2, 10	155.03	1.476
18H-2, 112.5	156.06	1.327
18H-3, 40	156.81	1.272
18H-3, 107	157.48	1.313
18H-5, 7.5	158.31	1.526
18H-5, 63.5	158.87	1.262
18H-6, 15	159.53	1.144
19H-1, 10.5	159.76	0.980
19H-1, 86	160.51	1.099
19H-2, 44	161.47	1.523
19H-2, 112	162.15	1.163
19H-3, 13.5	162.58	1.075
19H-5, 45	163.79	1.987
19H-6, 21	164.88	1.538
20H-1, 26	164.91	0.893
20H-2, 102	165.98	1.416
20H-3, 22	166.47	1.360
20H-3, 52	166.77	1.742
20H-4, 30	167.99	1.979
20H-4, 96	168.65	2.197
20H-6, 23	169.33	1.449
20H-6, 86	169.96	1.786
20H-7, 25	170.81	1.355
20H-7, 88	171.44	1.933
20H-8, 24	172.26	1.354
20H-8, 63	172.65	1.426
20H-9, 21	173.62	1.209
21H-1, 32	174.47	1.335
21H-1, 104	175.19	1.277
21H-2, 16	175.72	0.953
21H-2, 101	176.57	1.307
21H-4, 11	177.08	1.168
21H-5, 12	177.33	0.667
22H-5, 73	177.94	2.326
22H-1, 25	178.70	1.295
22H-2, 15	179.06	1.492
22H-2, 55	179.46	1.423
22H-3, 10	180.25	1.230
22H-4, 8	180.81	1.695
22H-6, 41.5	181.77	0.985
22H-7, 83	182.67	0.882
22H-8, 2.5	183.27	0.940
22H-9, 26	184.07	1.143
22H-10, 37	185.18	1.208
22H-11, 53.5	186.00	1.046
22H-12, 43	186.89	1.053
23H-1, 49.5	188.45	1.002
24T-1, 45.5	191.11	0.702
24T-1, 132	191.97	0.935
24T-2, 44	192.50	0.873
24T-2, 127	193.33	0.873
24T-4, 36	194.11	0.863
24T-4, 123.5	194.98	0.766
24T-5, 23	195.38	0.747
24T-5, 138	196.53	1.026
24T-6, 40	196.96	1.115
25T-1, 33	200.48	0.919
25T-1, 100	201.15	1.206
25T-2, 35	201.91	1.038
25T-2, 83	202.39	1.006
27T-1, 15	219.30	1.125
27T-2, 15	219.61	1.486
27T-2, 17	219.63	1.407
27T-2, 121	220.67	1.275
27T-3, 11	221.04	1.506
27T-3, 62	221.55	2.005
27T-4, 12	222.43	1.331
27T-4, 74	223.05	1.488
27T-6, 12	223.79	1.369
27T-6, 84	224.51	1.197
27T-7, 22	225.14	1.352
27T-7, 106	225.98	1.809
27T-8, 19	226.51	1.962
27T-8, 28	226.60	1.240
28T-1, 52	229.17	1.069
28T-1, 109	229.74	1.073
28T-2, 27	230.33	1.611
28T-2, 102	231.08	1.830
28T-3, 9	231.56	1.320
28T-3, 79	232.26	1.623
28T-5, 15	233.03	1.711
29T-1, 29	238.44	1.296
29T-1, 90	239.05	1.078
29T-2, 14	239.68	1.296
29T-3, 30	240.37	1.155
29T-3, 86	240.93	0.991
29T-4, 9	241.57	1.279
29T-4, 79	242.27	1.488
29T-5, 9	242.95	1.363
29T-5, 78	243.64	1.090
29T-7, 8	244.14	1.455
30T-1, 27	247.92	1.234
30T-1, 97	248.62	1.008
30T-2, 25	249.32	1.195
31X-1, 39	257.54	0.986
31X-1, 102	258.17	1.005
31X-2, 78	259.11	1.068
31X-3, 61	260.15	0.912
31X-5, 66	261.51	0.956
31X-6, 22.5	262.52	1.065
31X-6, 140	263.70	0.856
32X-1, 40	267.05	0.727
32X-1, 97	267.62	0.864
32X-2, 55.5	268.61	0.925
32X-2, 129	269.35	0.923
32X-3, 123	270.70	0.832
32X-4, 42.5	271.30	1.315
32X-4, 120	272.07	0.981
32X-5, 31.5	272.59	0.942
32X-5, 115	273.43	0.882
32X-6, 10	273.78	1.255
33X-1, 41.5	276.57	0.919
33X-2, 100.5	278.57	0.920
33X-3, 20.5	278.86	0.928
33X-4, 87	279.80	0.817
33X-5, 15.5	280.09	0.927
33X-5, 52	280.45	0.941
33X-7, 86	282.15	1.028
34X-1, 28	285.93	1.700
34X-1, 83	286.48	1.364
34X-2, 10	287.25	1.413
34X-2, 60	287.75	1.162
34X-3, 26	288.56	1.283
34X-4, 34	289.02	1.029
34X-5, 35	289.88	1.096
34X-7, 20	290.38	1.054
34X-8, 19	291.29	2.882
34X-9, 75	292.71	1.927
34X-9, 103	292.99	1.121
35X-1, 65	295.80	1.408
35X-2, 49	296.75	1.215
35X-3, 30	297.94	1.116
35X-5, 13	298.65	1.553
35X-6, 14	298.88	1.163
35X-6, 101	299.75	1.052
35X-7, 23	300.35	1.103
35X-7, 107	301.19	1.254
35X-9, 19	302.72	0.967
36X-2, 48	305.40	0.950
36X-3, 54	306.31	1.071
36X-4, 35	307.20	1.094
36X-6, 26	308.70	1.177
36X-6, 66	309.10	0.948
36X-7, 36	309.96	1.115
36X-7, 63	310.23	0.937
36X-8, 75	311.52	0.931

Table T11. Interstitial water geochemistry (raw data), Hole C0018A. (Continued on next page.)

Core, section	Whole-round length (cm)	Depth (mbsf)	pH	Alkalinity (mM)	Salinity	Chlorinity (mM)	Na^+ (mM)	NH_4^+ (μM)	Ca^{2+} (mM)	Mg^{2+} (mM)	Sr (μM)	Li (μM)	K^+ (mM)	PO_4^{3-} (μM)	SO_4^{2-} (mM)	Mn (μM)	Br^- (mM)	Ba (μM)	B (μM)	Fe (μM)	Si (μM)	V (nM)
333-C0018A-																						
1H-2	21.5	0.8	7.56	5.48	35.4	554	423	0.17	9.4	50.7	83	42	12.6	11.29	26.54	27.51	0.86	ND	493	5.89	695	170
1H-6	22	4.4	7.66	12.06	34.6	556	438	0.63	5.5	48.2	76	36	11.5	46.81	15.55	5.93	0.86	ND	507	6.23	682	115
2H-2	21.5	7.9	7.72	16.40	34.4	559	441	0.89	3.3	46.2	73	31	11.9	66.45	9.36	2.35	0.90	ND	533	6.87	701	61
2H-6	21.5	11.2	7.88	22.21	34.2	565	442	1.11	2.3	44.2	73	30	11.8	80.66	3.30	0.80	0.89	5.21	521	1.01	689	148
2H-10	21.5	14.6	7.94	26.06	34.2	562	433	1.24	1.9	44.6	82	27	11.3	97.42	0.44	0.18	0.89	91.32	533	ND	734	81
3H-5	22	20.7	7.84	26.04	33.9	563	447	1.57	1.6	39.2	82	21	10.1	104.11	0.46	1.27	0.93	183.86	458	1.08	625	105
4H-4	20	29.2	7.86	25.96	33.8	564	443	2.13	1.7	40.8	76	25	11.2	128.52	0.54	0.73	0.91	103.39	451	0.84	633	95
5H-4	21.5	38.9	7.84	27.41	34.2	569	447	2.64	1.8	40.6	71	28	11.2	127.82	0.71	1.30	0.92	83.34	452	1.89	684	107
6H-4	21	48.2	7.88	27.70	33.9	556	430	3.12	4.1	39.9	76	29	11.4	112.10	0.54	2.09	0.94	96.20	410	2.32	686	109
7H-4	23	57.6	7.88	29.79	34.2	560	437	3.74	1.9	39.8	75	32	11.5	97.41	0.50	1.08	0.94	99.62	399	1.77	618	124
8H-6	21	67.5	7.76	30.33	34.2	562	438	3.94	2.1	40.2	76	32	10.5	104.80	0.74	3.02	0.96	87.23	420	2.59	713	66
10H-4	21	83.1	7.81	31.00	34.3	560	436	4.45	2.3	39.3	80	32	10.4	114.23	0.43	1.99	0.99	82.63	406	2.41	744	82
11H-9	22	96.9	7.78	27.40	35.3	560	442	4.92	2.7	37.8	82	33	10.5	109.26	0.36	2.13	1.00	79.37	374	2.51	714	94
12H-5	21.5	103.4	7.81	29.54	34.5	562	447	5.18	2.6	35.6	80	33	10.6	90.32	0.45	1.10	1.00	75.87	363	2.94	694	117
13H-6	22	112.5	7.79	29.40	34.1	563	449	5.39	2.8	34.9	81	36	10.5	91.69	ND	0.87	0.99	75.69	369	2.10	712	97
14H-5	21.5	122.4	7.87	27.03	34.0	566	458	6.05	2.3	33.0	71	65	11.6	52.38	0.38	1.28	1.00	69.08	341	ND	685	114
15H-5	22	130.1	7.80	27.66	34.1	576	466	6.13	3.2	33.2	81	39	11.2	65.78	0.43	1.86	0.99	70.21	311	2.29	710	55
16H-12	25	143.9	7.89	26.69	34.2	562	456	6.74	3.0	32.1	75	41	10.9	52.07	0.39	2.11	1.03	65.21	303	3.51	733	66
17H-5	26	149.2	7.82	26.56	34.0	568	462	6.78	3.5	31.4	83	41	10.2	60.10	ND	2.02	1.02	65.62	306	3.92	748	49
18H-4	27.5	157.7	7.88	25.84	33.9	579	475	7.28	3.8	30.2	84	41	10.7	51.56	ND	0.94	1.04	63.55	257	1.99	691	67
19H-4	26.5	162.5	7.78	24.08	34.6	568	467	7.20	3.9	30.4	85	42	10.8	56.31	0.61	1.12	1.09	59.27	257	1.20	751	55
20H-5	21	168.7	7.84	24.06	34.1	567	466	7.75	3.6	30.3	77	43	10.7	41.79	0.32	0.88	1.03	53.58	230	2.49	656	63
21H-3	20	176.6	7.86	23.53	33.8	566	468	7.85	4.0	29.2	80	44	10.3	45.76	0.33	0.96	1.07	50.02	230	ND	725	56
22H-5	30	181.0	7.82	22.43	33.9	568	470	8.05	3.7	29.4	75	43	11.3	50.24	0.44	0.79	1.06	45.54	215	1.83	709	54
24T-3	27	193.5	7.74	23.49	34.2	570	470	7.77	4.8	29.8	81	40	10.1	74.67	0.91	0.72	1.04	35.70	223	2.05	697	58
27T-5	24	223.4	7.84	24.88	34.4	572	470	9.56	5.2	29.2	78	39	10.6	78.10	0.67	1.06	1.02	26.27	175	0.93	565	55
28T-4	26	232.6	7.79	24.44	35.0	572	472	9.38	5.3	29.1	79	45	9.1	94.44	0.88	1.46	1.05	23.54	190	1.42	688	42
29T-6	30	243.8	7.75	23.54	34.2	571	472	9.02	5.5	28.8	80	45	9.1	69.32	1.00	1.75	1.07	20.97	171	4.40	575	49
31X-4	31.5	260.5	7.67	24.47	34.9	577	476	9.07	5.8	29.6	84	42	9.1	69.49	0.70	1.50	1.07	22.33	185	2.48	676	55
33X-6	25.5	281.0	7.70	24.54	34.5	576	474	8.72	6.3	29.3	89	41	8.6	59.28	0.59	1.23	1.11	24.28	143	1.23	631	50
34X-6	24	289.9	7.62	22.31	34.5	578	477	8.67	6.4	29.7	89	46	9.5	50.92	0.94	1.42	1.11	25.24	172	1.15	620	54
35X-4	21.5	298.0	7.69	22.42	35.1	576	477	9.54	6.3	29.2	90	48.5	9.4	42.50	1.12	1.45	1.10	27.07	151	ND	712	21
36X-5	24	308.2	7.64	22.00	34.7	580	482	9.37	6.8	29.2	95	48.6	8.4	34.53	1.37	1.65	1.07	28.48	166	3.41	685	50

ND = not detected.

Table T11 (continued).

Core, section	Whole-round length (cm)	Depth (mbsf)	Cu (nM)	Zn (nM)	Rb (nM)	Mo (nM)	Cs (nM)	Pb (nM)	U (nM)
333-C0018A-									
1H-2	21.5	0.8	666	1582	2045	114	5.39	19.50	19.70
1H-6	22	4.4	1272	1914	1620	36	4.19	7.45	5.36
2H-2	21.5	7.9	981	532	1643	16	4.19	4.82	2.06
2H-6	21.5	11.2	ND	333	1673	16	4.48	1.30	8.42
2H-10	21.5	14.6	114	274	1551	9	4.20	0.27	2.09
3H-5	22	20.7	ND	134	1352	23	3.17	ND	2.69
4H-4	20	29.2	117	637	1374	270	3.80	2.05	3.74
5H-4	21.5	38.9	2832	1368	1365	59	4.21	8.99	2.34
6H-4	21	48.2	113	788	1420	157	4.98	0.55	4.33
7H-4	23	57.6	143	796	1464	166	5.32	1.84	3.96
8H-6	21	67.5	92	692	1263	112	3.99	0.43	1.87
10H-4	21	83.1	ND	622	1332	26	5.14	0.79	1.37
11H-9	22	96.9	103	627	1302	83	5.42	2.01	1.39
12H-5	21.5	103.4	2367	1265	1375	145	6.53	5.14	4.10
13H-6	22	112.5	212	1400	1338	99	6.30	2.52	3.26
14H-5	21.5	122.4	459	1041	1527	159	7.24	13.72	6.01
15H-5	22	130.1	3135	1400	1296	142	5.57	2.53	1.09
16H-12	25	143.9	1506	923	1314	94	5.34	1.62	1.86
17H-5	26	149.2	390	1497	1219	49	5.11	0.73	1.11
18H-4	27.5	157.7	930	2040	1257	216	5.76	6.60	3.16
19H-4	26.5	162.5	537	4302	1137	165	4.76	2.96	2.10
20H-5	21	168.7	2321	1893	1189	153	5.37	6.21	2.84
21H-3	20	176.6	1074	2103	1157	122	5.10	13.83	4.89
22H-5	30	181.0	1325	2126	1111	257	4.56	2.84	2.46
24T-3	27	193.5	1614	1118	1052	345	4.72	4.19	2.25
27T-5	24	223.4	676	1438	1212	160	5.57	1.32	1.36
28T-4	26	232.6	2018	1107	1165	138	4.94	0.80	1.47
29T-6	30	243.8	729	1899	1478	102	8.53	0.49	1.58
31X-4	31.5	260.5	334	3646	1276	151	5.94	0.73	1.94
33X-6	25.5	281.0	1133	2260	1202	42	6.51	0.67	1.45
34X-6	24	289.9	1616	2306	1160	131	5.47	0.88	1.85
35X-4	21.5	298.0	1544	2218	1211	134	5.62	1.77	2.57
36X-5	24	308.2	264	4331	1193	71	5.75	0.37	1.43

Table T12. Interstitial water geochemistry corrected for drill fluid contamination, Hole C0018A.

Core, section	Whole-round length (cm)	Depth (mbsf)	pH	Alkalinity (mM)	Salinity	Chlorinity (mM)	Na^+ (mM)	NH_4^+ (μM)	Ca^{2+} (mM)	Mg^{2+} (mM)	Sr (μM)	Li (μM)	K^+ (mM)	PO_4^{3-} (μM)	SO_4^{2-} (mM)	Mn (μM)	Br^- (mM)	Ba (μM)	B (μM)	Fe (μM)	Si (μM)
333-C0018A-																					
1H-2	21.5	0.8	7.56	5.48	35.4	554	423	0.17	9.4	50.7	83	42	12.6	11.29	26.54	27.51	0.86	ND	493	5.89	695
1H-6	22	4.4	7.66	12.06	34.6	556	438	0.63	5.5	48.2	76	36	11.5	46.81	15.55	5.93	0.86	ND	507	6.23	682
2H-2	21.5	7.9	7.72	16.40	34.4	559	441	0.89	3.3	46.2	73	31	11.9	66.45	9.36	2.35	0.90	ND	533	6.87	701
2H-6	21.5	11.2	7.88	22.21	34.2	565	442	1.11	2.3	44.2	73	30	11.8	80.66	3.30	0.80	0.89	5.21	521	1.01	689
2H-10	21.5	14.6	7.94	26.06	34.2	562	433	1.24	1.9	44.6	82	27	11.3	97.42	0.44	0.18	0.89	91.32	533	ND	734
3H-5	22	20.7	7.84	26.04	33.9	563	447	1.57	1.6	39.2	82	21	10.1	104.11	0.46	1.27	0.93	183.86	458	1.08	625
4H-4	20	29.2	7.86	25.96	33.8	564	443	2.13	1.7	40.8	76	25	11.2	128.52	0.54	0.73	0.91	103.39	451	0.84	633
5H-4	21.5	38.9	7.84	27.41	34.2	569	447	2.64	1.8	40.6	71	28	11.2	127.82	0.71	1.30	0.92	83.34	452	1.89	684
6H-4	21	48.2	7.88	27.70	33.9	556	430	3.12	4.1	39.9	76	29	11.4	112.10	0.54	2.09	0.94	96.20	410	2.32	686
7H-4	23	57.6	7.88	29.79	34.2	560	437	3.74	1.9	39.8	75	32	11.5	97.41	0.50	1.08	0.94	99.62	399	1.77	618
8H-6	21	67.5	7.76	30.33	34.2	562	438	3.94	2.1	40.2	76	32	10.5	104.80	0.74	3.02	0.96	87.23	420	2.59	713
10H-4	21	83.1	7.81	31.00	34.3	560	436	4.45	2.3	39.3	80	32	10.4	114.23	0.43	1.99	0.99	82.63	406	2.41	744
11H-9	22	96.9	7.78	27.40	35.3	560	442	4.92	2.7	37.8	82	33	10.5	109.26	0.36	2.13	1.00	79.37	374	2.51	714
12H-5	21.5	103.4	7.81	29.54	34.5	562	447	5.18	2.6	35.6	80	33	10.6	90.32	0.45	1.10	1.00	75.87	363	2.94	694
13H-6	22	112.5	7.79	29.40	34.1	563	449	5.39	2.8	34.9	81	36	10.5	91.69	ND	0.87	0.99	75.69	369	2.10	712
14H-5	21.5	122.4	7.87	27.03	34.0	566	458	6.05	2.3	33.0	71	65	11.6	52.38	0.38	1.28	1.00	69.08	341	ND	685
15H-5	22	130.1	7.80	27.66	34.1	576	466	6.13	3.2	33.2	81	39	11.2	65.78	0.43	1.86	0.99	70.21	311	2.29	710
16H-12	25	143.9	7.89	26.69	34.2	562	456	6.74	3.0	32.1	75	41	10.9	52.07	0.39	2.11	1.03	65.21	303	3.51	733
17H-5	26	149.2	7.82	26.56	34.0	568	462	6.78	3.5	31.4	83	41	10.2	60.10	ND	2.02	1.02	65.62	306	3.92	748
18H-4	27.5	157.7	7.88	25.84	33.9	579	475	7.28	3.8	30.2	84	41	10.7	51.56	ND	0.94	1.04	63.55	257	1.99	691
19H-4	26.5	162.5	7.78	24.08	34.6	568	467	7.20	3.9	30.4	85	42	10.8	56.31	0.61	1.12	1.09	59.27	257	1.20	751
20H-5	21	168.7	7.84	24.06	34.1	567	466	7.75	3.6	30.3	77	43	10.7	41.79	0.32	0.88	1.03	53.58	230	2.49	656
21H-3	20	176.6	7.86	23.53	33.8	566	468	7.85	4.0	29.2	80	44	10.3	45.76	0.33	0.96	1.07	50.02	230	ND	725
22H-5	30	181.0	7.82	22.43	33.9	568	470	8.05	3.7	29.4	75	43	11.3	50.24	0.44	0.79	1.06	45.54	215	1.83	709
24T-3	27	193.5	7.74	24.17	34.1	570	470	7.77	4.6	29.0	81	41	10.1	76.99	0.91	0.75	1.04	36.85	216	2.05	715
27T-5	24	223.4	7.84	25.41	34.4	573	470	9.56	5.1	28.6	78	40	10.6	79.88	0.67	1.09	1.03	26.89	169	0.93	575
28T-4	26	232.6	7.79	25.14	35.0	572	472	9.38	5.1	28.3	79	46	9.1	97.33	0.88	1.50	1.06	24.28	182	1.42	705
29T-6	30	243.8	7.75	24.31	34.2	571	472	9.02	5.3	27.9	79	45	9.1	71.71	1.00	1.81	1.08	21.72	162	4.40	590
31X-4	31.5	260.5	7.67	25.02	34.9	578	476	9.07	5.7	29.0	84	43	9.1	71.14	0.70	1.54	1.08	22.88	180	2.48	689
33X-6	25.5	281.0	7.70	25.00	34.5	577	474	8.72	6.2	28.8	89	41	8.5	60.44	0.59	1.26	1.12	24.78	138	1.23	641
34X-6	24	289.9	7.62	22.98	34.5	578	477	8.67	6.3	28.9	89	46	9.5	52.52	0.94	1.47	1.12	26.08	163	1.15	636
35X-4	21.5	298.0	7.69	23.23	35.1	577	477	9.54	6.1	28.2	90	49	9.4	44.09	1.12	1.51	1.12	28.15	140	ND	734
36X-5	24	308.2	7.64	22.98	34.7	581	482	9.37	6.6	27.9	96	50	8.3	36.10	1.37	1.74	1.08	29.89	153	3.41	712

ND = not detected.

Table T13. Headspace methane concentration, ethane concentration, and the ratios of methane to ethane (C1/C2), Hole C0018A.

Core, section, interval (cm)	Depth (mbsf)	Methane (ppmv)	Ethane (ppmv)	C1/C2
333-C0018A-				
1H-1, 75–79	0.7	0.0	0.0	100,000
2H-1, 124–128	7.8	6.7	0.0	100,000
3H-1, 137–141	17.4	12,093.6	0.0	100,000
4H-1, 146–150	27.0	7,769.1	0.0	100,000
5H-1, 137.5–141.5	36.4	18,073.1	1.4	13,008
6H-1, 136.5–140.5	45.9	15,255.0	1.4	11,011
7H-1, 136–140	55.4	7,666.7	0.0	100,000
8H-2, 142.5–146.5	65.2	5,961.9	0.0	100,000
10H-2, 137–141	81.8	5,552.1	0.0	100,000
11H-2, 132–136	91.3	4,843.5	0.0	100,000
12H-2, 119.5–123.5	100.9	4,332.4	0.0	100,000
13H-3, 136–140	110.3	3,281.6	0.0	100,000
14H-2, 135.5–139.5	119.7	5,101.0	0.0	100,000
15H-2, 114.5–118.5	127.7	2,823.9	0.0	100,000
17H-1, 136.5–140.5	145.9	5,503.8	0.0	100,000
18H-1, 124–128	154.8	4,428.3	0.0	100,000
19H-1, 133.5–137.5	160.8	5,583.1	0.0	100,000
20H-2, 125.5–129.5	166.1	919.4	0.0	100,000
21H-1, 136.5–140.5	175.4	4,270.1	0.0	100,000
22H-1, 42–46	178.9	7,729.8	1.6	4,808
24T-1, 136.5–140.5	192.0	2,309.8	0.0	100,000
25T-1, 137–141	201.5	19,338.7	1.6	11,926
27T-2, 142.5–146.5	220.9	6,522.1	0.0	100,000
29T-1, 134.5–138.5	239.5	14,496.4	1.4	10,228
30T-1, 137.5–141.5	249.0	5,693.6	0.0	100,000
31X-1,113.5–117.5	258.3	9,916.7	0.0	100,000
33X-4, 0–4	278.9	7,904.3	0.0	100,000
34X-3, 33.5–37.5	288.6	8,328.3	0.0	100,000
35X-2, 134–138	297.4	5,888.8	1.4	4,139
36X-2, 81–84	305.7	6,891.9	0.0	100,000

Methane and ethane are set at 0.0 when below detection. C1/C2 is set at 100,000 when ethane concentration is below detection.

Table T14. Bulk sediment calcium carbonate and elemental analyses data, Hole C0018A. (Continued on next page.)

Core, section, interval (cm)	Depth (mbsf)	$CaCO_3$ (wt%)	TOC (wt%)	TN (wt%)	TOC/TN_{at}	TS (wt%)
333-C0018A-						
1H-1, 10–13	0.1	11.04	0.92	0.12	9.0	0.11
1H-2, 21.5–22.5	1.0	13.09	0.77	0.10	8.6	0.09
1H-3, 49.5–50.5	1.5	17.56	0.59	0.07	10.0	0.06
1H-3, 133.5–134.5	2.3	17.50	0.60	0.08	9.1	0.19
1H-6, 22–23	4.6	10.22	0.91	0.10	10.9	0.16
1H-7, 69.5–72.5	5.3	10.17	0.58	0.07	9.3	0.07
1H-8, 27.5–28.5	6.2	13.15	0.76	0.10	9.3	0.15
2H-2, 21.5–22.5	8.1	14.37	0.72	0.09	9.4	0.14
2H-6, 21.5–22.5	11.4	13.53	0.63	0.08	9.8	0.21
2H-9, 20–22	14.3	17.82	0.63	0.07	10.3	ND
2H-10, 21.5–22.5	14.8	13.51	0.86	0.10	10.6	0.38
2H-11, 8–9	14.8	13.69	0.68	0.07	11.1	0.70
3H-2, 134–135	18.7	3.85	0.83	0.08	12.8	0.24
3H-4, 46–47	20.2	9.85	0.96	0.07	15.1	0.25
3H-5, 22–23	20.9	12.21	0.74	0.08	11.4	0.29
3H-8, 15–16	23.7	9.26	0.59	0.06	11.1	0.38
3H-8, 125–126	24.7	0.73	0.10	0.01	8.7	0.14
4H-3, 62.5–63.5	29.0	0.22	0.03	0.01	4.1	0.40
4H-4, 20–21	29.4	12.58	0.45	0.06	8.1	0.49
4H-8, 39.5–41.5	33.9	19.29	0.43	0.05	9.7	0.14
5H-1, 70–72	35.8	22.21	0.58	0.08	8.9	ND
5H-2, 20–22	36.7	16.99	0.51	0.06	10.3	0.11
5H-3, 110–111	38.9	0.91	0.05	0.01	6.1	1.19
5H-4, 21.5–22.5	39.1	15.04	0.45	0.06	9.4	ND
5H-7, 127–128	43.0	14.69	0.53	0.06	10.8	0.41
5H-8, 31–32	43.5	17.86	0.50	0.06	9.6	0.25
6H-1, 81–82	45.4	22.57	0.46	0.06	8.8	ND
6H-3, 26–28	47.4	0.43	0.05	0.02	3.5	0.10
6H-4, 21–22	48.4	10.23	0.65	0.07	10.7	0.15
6H-5, 124.5–125.5	49.6	13.48	0.63	0.07	10.4	0.07
6H-7, 118–120	52.0	14.12	0.60	0.07	9.5	0.16
7H-4, 23–24	57.8	3.27	0.12	0.02	7.6	0.32
7H-9, 134–135	61.7	25.36	0.36	0.06	7.4	0.09
8H-4, 19–20	66.4	24.88	0.28	0.05	7.2	0.10
8H-6, 21–22	67.7	23.40	0.60	0.08	8.8	ND
8H-9, 37–38	70.4	18.10	0.61	0.08	9.4	0.07
8H-9, 112.5–115.5	71.1	16.47	0.61	0.07	9.8	0.09
10H-4, 21–22	83.3	11.63	0.43	0.05	10.0	0.33
10H-7, 63–65	86.4	10.15	0.52	0.07	8.7	0.68
10H-8, 129–131	88.2	3.64	0.18	0.03	6.9	0.93
10H-9, 87–88	89.1	10.08	0.57	0.07	9.0	0.32
11H-2, 55–57	90.7	7.73	0.53	0.07	8.6	0.45
11H-8, 94–95	96.7	9.55	0.61	0.08	9.3	0.09
11H-9, 22–23	97.1	12.27	0.57	0.07	10.3	0.10
11H-10, 61–62	97.7	11.55	0.57	0.08	8.8	0.08
11H-11, 18.5–19.5	98.5	8.87	0.58	0.07	10.0	0.28
12H-4, 68–69	102.9	9.20	0.51	0.07	8.6	0.64
12H-5, 21.5–22.5	103.6	11.66	0.50	0.06	9.6	0.10
12H-8, 120.5–121.5	107.3	11.99	0.60	0.08	8.7	ND
12H-9, 20–21	107.7	12.79	0.59	0.07	9.2	0.08
13H-4, 125.5–126.5	111.4	9.56	0.53	0.07	9.0	0.31
13H-5, 108.5–109.5	112.4	11.10	0.55	0.07	8.7	0.76
13H-6, 22–23	112.7	8.94	0.47	0.06	9.7	0.15
14H-4, 20–21	121.4	9.26	0.48	0.07	8.0	0.79
14H-5, 21.5–22.5	122.6	12.17	0.54	0.07	9.3	0.35
14H-6, 128–129	123.9	13.05	0.54	0.07	9.3	0.29
15H-2, 65–66	127.3	9.57	0.47	0.07	7.6	0.48
15H-3, 33–34	128.1	11.90	0.44	0.06	8.3	0.48
15H-5, 22–23	130.3	8.64	0.44	0.06	8.9	0.39
15H-7, 80–81	132.3	4.43	0.36	0.06	7.0	0.62
16H-2, 60–61	138.2	6.70	0.42	0.07	7.1	0.49
16H-11, 12–13	142.6	11.22	0.72	0.09	9.4	0.46
16H-11, 122–123	143.7	10.21	0.66	0.09	8.8	0.60
16H-12, 25–26	144.1	12.29	0.58	0.07	9.4	0.53
17H-1, 50–51	145.1	3.90	0.31	0.05	7.0	0.54
17H-2, 39–40	146.3	6.05	0.54	0.08	8.4	0.48

Table T14 (continued).

Core, section, interval (cm)	Depth (mbsf)	$CaCO_3$ (wt%)	TOC (wt%)	TN (wt%)	TOC/TN_{at}	TS (wt%)
17H-3, 110–111	148.3	17.85	0.44	0.07	7.7	0.22
17H-5, 26–27	149.4	10.27	0.46	0.06	8.7	0.39
17H-6, 19–20	149.6	11.07	0.48	0.07	7.6	0.38
18H-3, 11.5–12.5	156.4	7.08	0.50	0.07	7.8	0.34
18H-4, 27.5–28.5	157.9	1.92	0.34	0.05	7.6	0.23
18H-5, 98.5–99.5	158.9	8.51	0.44	0.07	7.3	ND
19H-1, 121.5–122.5	160.7	12.91	0.41	0.07	7.0	0.30
19H-3, 46.5–47.5	162.4	8.22	0.55	0.08	8.1	0.39
19H-4, 26.5–27.5	162.7	8.99	0.52	0.08	7.7	0.47
20H-3, 123.5–124.5	167.4	8.29	0.56	0.07	9.4	0.08
20H-5, 21–22	168.9	13.85	0.46	0.07	7.9	0.08
20H-6, 125–126	170.1	9.40	0.46	0.07	7.5	0.23
20H-7, 129.5–130.5	171.5	8.13	0.48	0.08	7.4	0.50
20H-8, 119–120	172.8	8.20	0.48	0.07	7.7	0.34
21H-3, 20–21	176.8	7.38	0.50	0.07	8.0	0.53
22H-2, 35–36	179.3	11.04	0.41	0.06	7.4	0.28
22H-2, 110–111	180.0	10.40	0.45	0.06	8.8	0.47
22H-5, 30–31	181.3	13.01	0.47	0.06	9.1	0.40
22H-7, 55–56	182.4	12.40	0.46	0.08	7.1	0.33
24T-1, 36–37	191.0	1.77	0.47	0.05	10.8	0.18
24T-2, 20–22	192.3	1.75	0.53	0.07	9.4	0.24
24T-2, 102–103	193.1	5.58	0.44	0.06	7.9	0.14
24T-3, 27–28	193.7	1.84	0.57	0.08	8.2	0.16
24T-5, 114–115	196.3	4.02	0.47	0.07	8.0	0.26
25T-1, 66–69	200.8	3.32	0.53	0.07	8.8	0.42
25T-2, 93–96	202.5	0.75	0.15	0.03	6.2	0.43
27T-2, 52–53	220.0	3.09	0.37	0.05	8.9	0.13
27T-3, 44–45	221.4	4.06	0.50	0.07	8.8	0.10
27T-3, 116–117	222.1	1.06	0.38	0.07	6.7	0.05
27T-4, 66–67	223.0	1.35	0.36	0.05	9.0	0.13
27T-5, 24–25	223.7	3.41	0.33	0.06	6.7	0.07
27T-8, 80–81	227.1	3.78	0.59	0.07	9.5	0.11
28T-3, 43–44	231.9	5.59	0.63	0.10	7.4	0.14
28T-3, 105–106	232.5	4.89	0.45	0.07	7.3	0.77
28T-4, 26–27	232.9	3.33	0.49	0.05	10.5	0.41
29T-1, 68–69	238.8	2.89	0.43	0.05	9.4	0.13
29T-4, 52–53	242.0	4.26	0.58	0.08	8.7	0.09
29T-4, 127–128	242.7	5.00	0.57	0.08	8.3	0.06
29T-5, 43–44	243.3	3.83	0.51	0.06	9.7	0.09
29T-6, 30–31	244.1	1.03	0.43	0.05	9.7	0.08
30T-1, 30.5–33.5	248.0	4.43	0.49	0.07	8.0	0.08
30T-2, 104–105	250.1	1.79	0.35	0.06	6.5	0.05
31X-2, 105.5–106.5	259.4	2.49	0.43	0.06	9.0	0.15
31X-4, 31.5–32.5	260.8	2.30	0.53	0.05	11.4	0.50
31X-5, 14–15	261.0	1.62	0.53	0.09	7.2	0.07
31X-6, 69–70	263.0	1.38	0.36	0.04	10.7	1.08
32X-2, 17–19	268.2	3.05	0.45	0.06	9.3	0.14
32X-2, 101.5–103.5	269.1	8.09	0.64	0.08	9.2	0.06
32X-5, 92–95	273.2	0.82	0.23	0.03	8.8	0.22
33X-6, 25.5–26.5	281.3	3.38	0.35	0.06	7.2	0.07
33X-7, 31–32	281.6	4.23	0.37	0.06	7.0	0.09
33X-8, 37–38	282.6	0.56	0.38	0.08	5.8	0.04
33X-9, 36–37	283.1	0.95	0.29	0.04	8.0	0.20
34X-2, 19–20	287.3	4.31	0.56	0.08	8.2	0.08
34X-6, 24–25	290.2	1.80	0.46	0.05	11.3	0.14
34X-7, 83–84	291.0	4.18	0.66	0.07	10.5	0.12
35X-4, 21.5–22.5	298.2	2.68	0.61	0.09	8.3	0.42
36X-2, 63–64	305.6	2.37	0.60	0.08	9.3	0.16
36X-3, 85–86	306.6	1.60	0.41	0.04	11.0	0.68
36X-4, 92–93	307.8	5.16	0.65	0.09	8.7	0.09
36X-4, 110–111	307.9	7.68	0.59	0.08	8.6	0.06
36X-5, 24–25	308.4	2.31	0.54	0.05	11.7	0.28
36X-8, 52–53	311.3	2.75	0.45	0.05	9.6	0.12

TOC = total organic carbon, TN = total nitrogen, TOC/TN_{at} = atomic ratios of TOC to TN, TS = total sulfur. ND = not determined.

Table T15. Rock-Eval pyrolysis data, Hole C0018A.

Core, section, interval (cm)	Depth (mbsf)	S1 (mg HC/g sediment)	S2 (mg HC/g sediment)	T_{max} (°C)	Hydrogen index (mg HC/g TOC)	Production index
333-C0018A-						
1H-6, 22–23	4.6	0.12	0.74	415	81	0.14
2H-2, 21.5–22.5	8.1	0.04	0.50	401	69	0.07
2H-10, 21.5–22.5	14.8	0.04	0.80	415	93	0.04
3H-4, 46–47	20.2	0.04	0.41	397	42	0.09
3H-8, 15–16	23.7	0.04	0.33	394	56	0.11
5H-2, 20–22	36.7	0.02	0.24	394	46	0.06
6H-1, 81–82	45.4	0.02	0.19	378	40	0.11
6H-4, 21–22	48.4	0.02	0.31	400	47	0.05
6H-7, 118–120	52.0	0.02	0.38	397	63	0.05
7H-4, 23–24	57.8	0.00	0.01	608	8	0.00
8H-9, 37–38	70.4	0.02	0.36	411	59	0.05
10H-9, 87–88	89.1	0.01	0.19	386	33	0.04
11H-8, 94–95	96.7	0.00	0.17	397	27	0.01
12H-9, 20–21	107.7	0.01	0.24	397	40	0.03
14H-6, 128–129	123.9	0.01	0.27	396	50	0.05
16H-12, 25–26	144.1	0.01	0.30	410	51	0.05
18H-3, 11.5–12.5	156.4	0.00	0.16	400	31	0.00
19H-4, 26.5–27.5	162.7	0.00	0.15	398	29	0.00
21H-3, 20–21	176.8	0.00	0.12	405	24	0.00
22H-2, 35–36	179.3	0.01	0.15	397	37	0.07
24T-1, 36–37	191.0	0.00	0.07	421	15	0.00
25T-1, 66–69	200.8	0.01	0.22	411	41	0.04
27T-5, 24–25	223.7	0.00	0.03	417	9	0.00
28T-4, 26–27	232.9	0.00	0.10	413	20	0.00
29T-1, 68–69	238.8	0.00	0.21	426	48	0.02
29T-5, 43–44	243.3	0.01	0.16	431	31	0.03
31X-5, 14–15	261.0	0.00	0.18	412	33	0.00
34X-2, 19–20	287.3	0.00	0.23	424	41	0.01
36X-2, 63–64	305.6	0.04	0.31	425	51	0.12
36X-8, 52–53	311.3	0.00	0.20	426	44	0.00

HC = hydrocarbon, TOC = total organic carbon.